

Dissertation
submitted to the
Combined Faculties of the Natural Sciences and Mathematics
of the Ruperto-Carola University of Heidelberg, Germany
for the degree of
Doctor of Natural Sciences

Put forward by
Ruoyu Liu
born in: Nanjing, China
Oral examination: 10th June, 2015

Constraining sources of ultrahigh energy
cosmic rays and shear acceleration
mechanism of particles in relativistic jets

Referees: Prof. Dr. Matthias Bartelmann
Prof. Dr. Felix Aharonian

Zusammenfassung

Ultraenergetischer kosmischer Strahlung sind extrem energiereiche Teilchen von der Aussen Raum. Sie haben grosses Interesse von Wissenschaftlern für mehr als fünfzig Jahren geweckt. Jedoch aufgrund der seltenen Ereignissen und komplex in ihrer Ausbreitung auf die Erde, sie sind nach wie vor eines der grössten Rätsel in der modernen Hochenergie-Astrophysik. Diese Dissertation widmet, die Herkunft der ultrahochenergetischer kosmischer Strahlung aus studieren verschiedene Aspekte. Erstens, einen möglichen Zusammenhang diskutierten wir zwischen kurzem entdeckt Unter-PeV/PeV Neutrinos und ultrahochenergetischer kosmischer Strahlung. Wenn diese beiden Arten von Teilchen den gleichen Ursprung haben, kann die Beobachtung von Neutrinos liefern zusätzlichen und nicht-triviale Einschränkungen für die Quellen von Ultrahochenergetischer kosmischer Strahlung. Zweitens, unter Verwendung der Messung der chemischen Zusammensetzung und der Ankunft Richtungen von Ultraenergetischer kosmischer Strahlung gemeinsam finden wir eine robuste Obergrenze für Entfernungen Quellen von Ultrahochenergetischer kosmischer Strahlung oberhalb ~ 55 EeV sowie als untere Grenze für ihre Metallizitäten. Schliesslich untersuchen wir die Scherbeschleunigung Mechanismus in der relativistischen Jets, die eine effizientere Mechanismus beschleunigt wird menarbeit der höheren Energiepartikel. Wir berechnen die Beschleunigungseffizienz und zeitabhängige Partikelspektrum, aber auch in die Funktion von Synchrotronstrahlung suchen Strahlung beschleunigter Teilchen. Möglichkeit dieser Mechanismus der Beschleunigung ultrahochenergetischer kosmischer Strahlung in realistischer astrophysikalischen Umwelt auch diskutiert.

Abstract

Ultrahigh energy cosmic rays are extreme energetic particles from outer space. They have aroused great interest among scientists for more than fifty years. However, due to the rarity of the events and complexity of the process of their propagation to Earth, they are still one of the biggest puzzles in modern high energy astrophysics. This dissertation is dedicated to study the origin of ultrahigh energy cosmic rays from various aspects. Firstly, we discuss a possible link between recently discovered sub-PeV/PeV neutrinos and ultrahigh energy cosmic rays. If these two kinds of particles share the same origin, the observation of neutrinos may provide additional and non-trivial constraints on the sources of ultrahigh energy cosmic rays. Secondly, we jointly employ the chemical composition measurement and the arrival directions of ultrahigh energy cosmic rays, and find a robust upper limit for distances of sources of ultrahigh energy cosmic rays above ~ 55 EeV, as well as a lower limit for their metallicities. Finally, we study the shear acceleration mechanism in relativistic jets, which is a more efficient mechanism for the acceleration of higher energy particle. We compute the acceleration efficiency and the time-dependent particle energy spectrum, and explore the feature of synchrotron radiation of the accelerated particles. The possible realizations of this mechanism for acceleration of ultrahigh energy cosmic rays in different astrophysical environments is also discussed.

Contents

Contents	ii
List of Figures	iii
1 Introduction	1
1.1 Some Popular Particle Acceleration Mechanisms	2
1.2 Candidate Sources	12
1.3 Extensive Air Shower and Detection Technique	16
1.4 Recent Observations of Ultrahigh Energy Cosmic Rays	20
2 Possible Link Between PeV Neutrinos and UHECR	29
2.1 Detection of High-energy Neutrinos and Its Implications	29
2.2 Possible Common Sources for PeV Neutrinos and UHECRs	32
2.3 Neutrino Emission from Semi-relativistic Hypernova Remnants	40
2.4 Discussion	44
3 Constraints on the Sources of Ultra-high Energy Cosmic Rays Using Anisotropy vs Chemical Composition	49
3.1 A Joint Analysis on Anisotropy and Chemical Composition Measurement of UHECRs	49
3.2 Anisotropies at Constant Rigidity	51
3.3 Discussion	62
3.4 Conclusion	68
4 Particle Acceleration in Relativistic Turbulent Gradual-shear Jets	71
4.1 A Brief History of Study on Shear Acceleration	71
4.2 A Microscopic Analysis	73
4.3 Accelerated Particle Spectrum	82
4.4 Discussion	99
4.5 Conclusion	101
5 Summary, Discussion and Future Work	105

List of Figures

- 1.1 A Hillas diagram from Kotera & Olinto (2011). The blue (red) line shows conditions for confinement of protons (iron nuclei) with energy of $E_{\max} = 10^{20}$ eV. Various candidate sources with uncertainties in parameters are shown with colored region. 13
- 1.2 A schematic picture for the development of cascade. At each step roughly 1/3 of the energy is transferred from the hadronic cascade to the electromagnetic one. The figure is from Letessier-Selvon & Stanev (2011). 19
- 1.3 Energy spectrum of UHECRs measured by the PAO. The numbers give the number of events in each energy bin. The last three arrows represent upper limits at 84% C.L. This figure is taken from The Pierre Auger Collaboration (2013a) 22
- 1.4 The hybrid spectrum obtained by the TA (black circles). The spectrum measured by the surface array (purple squares) and the MD monocular spectrum (green squares) is shown for reference. The figure is taken from Telescope Array Collaboration 2014 23
- 1.5 Attenuation length of different species of cosmic rays when they propagate in the intergalactic space of the local universe. The figure is taken from Allard et al. 2006 24
- 1.6 Theoretical fit to the Auger's CR spectrum. A pure proton injection (red) and an iron nuclei injection (blue) are assumed respectively. This figure is taken from The Pierre Auger Collaboration (2013a) 25
- 1.7 Energy evolution of X_{\max} and $\text{RMS}\langle X_{\max} \rangle$ measured by the PAO, with comparison to air-shower simulations for proton and iron primaries in different hadronic models. The figure is taken from The Pierre Auger Collaboration (2013a). 26

- 1.8 Shower maximum measurements of the TA experiment with the comparison to different hadronic models. Data are the black points with error bars. The solid black line is a fit to the data. Colored lines are fits to Monte-Carlo. Blue is proton and red is iron. The green hashed box indicates the total systematic error on $\langle X_{\max} \rangle$. The figure is taken from Telescope Array Collaboration (2015) 27
- 1.9 An earlier report of arrival directions of highest energy cosmic rays by the PAO (The Pierre Auger Collaboration 2010a). There are 69 events in total with energy $E \geq 55$ EeV detected up to 31 December 2009. UHECR events are plotted as black dots in an Aitoff-Hammer projection of the sky in galactic coordinates. The solid line represents the field of view of the PAO for zenith angles smaller than 60° . Blue circles of radius 3.1° are centred at the positions of the 318 AGNs in the VCV catalog that lie within 75 Mpc and that are within the field of view of the Observatory. Darker blue indicates larger relative exposure. The exposure-weighted fraction of the sky covered by the blue circles is 21%. 28
- 1.10 99% *C.L.* upper limits on dipole (left panel) and quadrupole (right panel) amplitudes as a function of the energy. Theoretical anisotropy expectations from stationary galactic sources that distributed in the disk are also shown for comparison, in pure proton and iron nuclei composition cases respectively. The uncertainty of the amplitudes due to the stochastic nature of the turbulent component of the magnetic field are sampled from different simulation data sets and are shown by colored bands. The figure is taken from The Pierre Auger Collaboration (2013b) 28

- 2.1 The local proton energy production rate $\dot{W}_{p,0}$ versus f_π , the pion-production efficiency of escaping CRs that produce PeV neutrinos. The black solid line represents the relation between $\dot{W}_{p,0}$ and f_π required to reproduce the observed neutrino flux, with the gray band corresponding to its $1-\sigma$ confidence interval. The upper and lower dashed curves represent the local energy production rate $\dot{W}_{CR,0}$ of escaping CRs required to account for the observed UHECRs if the Galactic-extragalactic transition occurs at the second knee and at the ankle, respectively, for the case $\xi = 1$. The dotted curves are corresponding ones for the case $\xi = 0$. Here $\alpha = 10$ is assumed for the normalization factor of the proton spectrum (note $\alpha = \ln(E_{max}/E_{min})$ for $s_p = 2$). Larger/smaller values of alpha will shift all curves in the plot upwards/downwards by the same factor. See text for discussion on the regions corresponding to different potential UHECR source candidates. 35
- 2.2 Propagated spectrum of cosmic rays assuming a source composition equal to that of the stellar wind of Wolf-Rayet stars. The black solid line represents the all-particle flux, while other lines represent the contributions by different species as shown in the legend. The black squares are data measured by PAO (Pierre Auger Collaboration 2011). The figure is taken from Liu & Wang (2012) 37
- 2.3 Propagated spectrum of cosmic rays assuming a source composition equal to that of the hypernova ejecta in the model of SN 1998bw. The figure is taken from Liu & Wang (2012) 38

- 2.4 Panels (a)-(c) show the propagated cosmic-ray spectrum for the source composition equal to that of the hypernova ejecta, similar to Fig. 2.3, but with some modifications taken into account. In panel (a), the abundance of iron nuclei in the ejecta is increased by a factor of three. In panel (b), a hard initial spectrum with $p = 1.6$ is assumed. In panel (c), the local source number density is taken to be two times higher than the average within a distance of 30 Mpc. The dashed line in panel (c) represents the contribution by sources beyond 30 Mpc while the dash-dotted line represents the contribution by local sources within 30 Mpc. Panel (d) shows the propagated cosmic-ray spectrum for the source composition equal to that of stellar wind, but with the effects of a hard spectrum and a local overdensity being taken into account. The figure is taken from Liu & Wang (2012) 39
- 2.5 Spectra of ν_μ and gamma rays produced by SR-hypernova remnants in star-forming galaxies. Upper panel: the red dashed line and dash-dotted line represent the one-flavor neutrino flux from starburst galaxies and normal star-forming galaxies respectively, and the red solid line is their sum. Neutrino oscillations imply that $\nu_\mu : \nu_e : \nu_\tau = 1 : 1 : 1$ at the detector. The blue dashed and dotted lines represent the gamma ray fluxes from pion decay (accounting for intergalactic absorption) and the cascaded gamma ray flux, respectively, while the blue solid line is the sum of the two components. Data points are taken from (Abdo et al. 2010). The shaded rectangle shows the IceCube flux (IceCube Collaboration 2013b). Lower panel: same as the upper one but with $D_0 = 10^{27} \text{ cm}^2\text{s}^{-1}$ used for normal star-forming galaxies and $f_{SB} = 10\%$. See text for more discussion. 45
- 2.6 Diffusive neutrino flux from star-forming of different populations. The red, orange, green, blue lines show the flux contributed by starburst galaxies, normal spiral galaxies, SF-AGNs (SB) and SF-AGNs (spiral), respectively. And the black line represents the sum. The cyan line shows the associated produced diffuse gamma-ray flux. The figure is taken from Chang et al. (2014) 48
- 3.1 An example of propagated spectrum of UHECRs. The injection particles are oxygen nuclei which travel a distance of 50 Mpc. The initial spectrum is set to be a power-law spectrum with index of -2 and with an abrupt cutoff at 10^{21} eV. The figure is taken from Liu et al. (2012) 57

- 3.2 The phenomenological fit of nucleon loss rate for some species of cosmic rays. The blue lines are numerically calculated results while the green ones are plotted based on the analytical expressions (Eq. 3.18). 58
- 3.3 Ratio of anisotropy significance at low to high energies as a function of the distance to the sources responsible for the anisotropy. Solid lines represent the numerical results while dashed lines represent the analytical results; thick solid line: scenario (A), in which one sums up over fragments of similar rigidity, in interval $[E_1, E_2]$, with at most $Z/4$ photodisintegration interactions; thin solid lines: scenario (B), in which one sums up over all fragments with rigidities in excess of E_1/Z . The source is assumed to inject pure O, Si or Fe composition as indicated. 61
- 3.4 The minimum metal mass relative to hydrogen in the source, assuming pure O, Si or Fe compositions are injected. Thick solid lines and thin solid lines respectively represent results in scenario (A) and (B), which are the same as in Fig. 3.3. 62
- 4.1 A sketch of the geometry. The jet propagates along the z -axis with a velocity profile as a function of distance from the propagation axis. The angle between the z -axis and particle's velocity is θ while the angle between the x -axis and the projection of particle's velocity on the xy -plane is ϕ . 74
- 4.2 Average acceleration rate as a function of particle energy (Lorentz factor). The upper panel is for the case of a mildly-relativistic jet while the lower panel is for the case of an ultra-relativistic jet. 83
- 4.3 Average acceleration rate as a function of radius (vertical distance to the propagation axis). The upper panel is for the case of a mildly-relativistic jet while the lower panel is for the case of an ultra-relativistic jet. 84

- 4.4 $q = 1$ case. **Top panel:** timescales for different processes. The blue and green lines show the average shear acceleration timescale and stochastic timescale. The thick black line is the real acceleration timescale under these two acceleration mechanisms. The dashed line represents synchrotron cooling timescale while the dash-dotted line represents diffusive escape timescale; **Middle panel:** evolution of electron spectrum. Thin black lines are spectrum at certain time after the injection while the thick line shows the spectrum in steady state. The dashed line exhibits the analytical solution for steady state; **Bottom panel:** synchrotron radiation of electrons in steady state. Transverse radius of jet is $r_j = 10^{20}$ cm, while the size of shearing region is $\Delta L = 10^{19}$ cm. The background magnetic field is $B_0 = 3\mu\text{G}$. The energy density ratio between turbulent magnetic field and background magnetic field is $\xi = 0.1$. The number density of protons is 10^{-4}cm^{-3} which leads to an Alfvén speed of $\beta_A \simeq 0.007$. 87
- 4.5 The same as Fig. 4.4 but for $q = 5/3$ case. 88
- 4.6 The same as Fig. 4.4 but for $q = 2$ case. In this case, the mean scattering time is independent on particle energy. 89
- 4.7 Time-dependent evolution of electron spectrum without stochastic acceleration. All parameters are same the as in the Fig. 4.5. 91
- 4.8 The time-dependent evolution of electron spectrum without escape (but with stochastic acceleration). All parameters are same the as in the Fig. 4.5. 93
- 4.9 the same as Fig. 4.4 but for proton acceleration. 94
- 4.10 the same as Fig. 4.5 but for proton acceleration. 95
- 4.11 the same as Fig. 4.6 but for proton acceleration. 96
- 4.12 Time-depended evolution of electron spectrum, by using Monte-Carlo method, in an ultra-relativistic gradual-shear jet for $q = 1$, $q = 5/3$ and $q = 2$ cases respectively. Solid lines are the spectrum in different time while dash lines show the steady-state analytical solutions with neglecting the diffusion term in the Fokker-Planck equation. 98
- 4.13 Available jet parameter space for acceleration of 10^{18} eV (upper panel) and 10^{20} eV (lower panel) protons for $q = 5/3$ case. The hatched blue regions are for weakly-relativistic jets and the hatched yellow regions are for ultra-relativistic jets. Jet parameters are identical to those used in Section 4.3.1 and Section 4.3.2. 102

Introduction

Cosmic rays are energetic particles of extra-terrestrial origins. Most of the cosmic rays comprise protons and nuclei, with a smaller fraction of electrons (positrons), photons, neutrinos and mesons. To zero-order approximation, the spectrum of all particles of cosmic rays can be described by a power-law of index -2.7 , spanning over 11 decades from 1 GeV ($= 10^9 \text{ eV}$) to 10^{11} GeV . But if one looks closely into the spectrum, finer structures can be revealed. The two most distinct features are the "knee" around 3 PeV ($1 \text{ PeV} = 10^{15} \text{ eV}$) where the spectrum steepens and the power-law of index changes from -2.7 to -3.1 , and the "ankle" above a few EeV ($1 \text{ EeV} = 10^{18} \text{ eV}$) where the spectrum flattens to -2.7 again. A second knee where the spectrum softens further has been reported by some experiments around $0.4 - 0.8 \text{ EeV}$. Ultrahigh energy cosmic rays (UHECRs) usually refer to cosmic rays with energies above 1 EeV .

At the very end of the cosmic ray spectrum, the event of UHECRs is very rare. UHECRs with energies above 10^{20} eV are estimated to have a rate of only about 1 event per square kilometer per century per steradian. Due to the pioneering work of Linsley and collaborators, the first UHECR of energy 10^{20} eV was discovered in 1962 (Linsley 1963). The mystery of UHECRs can be basically summarized into three questions, which are also related to each other:

- What are they? i.e., the species/chemical composition of UHECRs
- Where are they from? i.e., the sources and their spatial distribution
- How can they achieve such high energies? i.e., the acceleration mechanisms of UHECRs

Besides, studying UHECRs is also of particular relevance to particle physics, because they serve as natural particle beams for exploring the behavior of particles

at extremely high energies, which significantly surpass the highest achievable energy in man-made laboratories (like LHC) nowadays, and may lead to important discoveries in particle physics. Among all these intriguing issues, perhaps the most attracting one to theoretical astrophysicists is the way of reaching extremely high energies. However, since the acceleration of these particles is very difficult, some particle physics processes were introduced to explain these particles' origin. The main alternative explanation, also known as the "top-down" model, was the decay of super-heavy particles X , which could be emitted by topological defects or preserved since the very early universe (e.g., Hill et al. 1987; Chung et al. 1999; Bhattacharjee 2000). However, recent observations of particle arrival directions (as we will introduce later) indicate that UHECRs seem to correlate with nearby large scale structure, while the top-down model predicted an isotropic distribution, strongly favoring their astrophysical origins. Thus, it brings peoples' attentions back to the acceleration mechanisms in astrophysical sources. On the other hand, because of the harsh condition for the astrophysical sources to acceleration particles to such high energies, there must not be many kinds of objects able to fulfill it. So if one can figure out the way of acceleration, it also helps in pinpointing the sources of these particles.

1.1 Some Popular Particle Acceleration Mechanisms

We will introduce some particle acceleration mechanisms in the following, with an emphasis on Fermi acceleration, as it is the most widely considered mechanisms, while inductor and magnetic reconnection will also be briefly mentioned.

1.1.1 Fermi Acceleration

The Fermi acceleration mechanism considers the scenario in which particles gain energy through elastic collision with moving scattering centers, and converts the macroscopic kinetic energy of the scattering centers to microscopic nonthermal energy of particles. In astrophysical environments, the scattering centers are found to be magnetohydrodynamic(MHD) waves such as Alfvén waves, which are due to oscillation of ions in response to a restoring force provided by tensions of magnetic field lines. The MHD waves are perturbations of background magnetic fields, varying with both time and space and hence exciting electric fields that can accelerate particles as they pass through or as particles pass through each other.

Wave-particle Interaction

Usually, one treats the scattering in the frame of waves, so that the electric field vanishes and the energies of particles are conserved before and after scattering. In the following derivation, we will follow the method in Kulsrud (2005). Consider that the length of a wave packet of Alfvén waves is L . Assume that the wave propagates along the z -axis and is polarized in x -axis. The perturbed magnetic field in the xy -plane can be given by

$$\delta B_{\perp} = \vec{e}_x \delta B \sin(kz - \omega t) \quad (1.1)$$

where δB , $k = 2\pi/\lambda$ and $\omega = kv_A$ are the amplitude, wavenumber and angular frequency of the wave respectively, with λ the wave length and v_A the Alfvén speed. Consider a proton with velocity v moving with a pitch angle θ . The particle's velocity in y -direction is

$$v_y = v \sin \theta \sin(\Omega t + \phi) \quad (1.2)$$

where $\Omega = eB_0/\gamma mc$ is the gyro-frequency of a charged particle with γ being the Lorentz factor of the particle and B_0 the strength of the background magnetic field which also lies along the z -axis. Here ϕ is the random phase between the particle and the wave. Then, we can write the Lorentz force along the z -axis as

$$\begin{aligned} F_z &= \frac{e}{c} (\vec{v} \times \vec{B})_z = \frac{e}{c} \delta B v \sin \theta \sin(kz_0 + kv_z t - \omega t) \sin(\Omega t + \phi) \\ &= \frac{1}{2} \frac{e}{c} v \sin \theta \delta B \{ \cos[(kv_z - \omega + \Omega)t + (kz_0 + \phi)] - \cos[(kv_z - \omega - \Omega)t + (kz_0 - \phi)] \} \end{aligned} \quad (1.3)$$

Here z_0 is the position of particle on the z -axis at $t = 0$. If $v_z > 0$, the first cosine term averages out after some time t due to its high frequency while the second term may not average out when

$$kv_z - \omega - \Omega \simeq 0 \quad (1.4)$$

. Since the Alfvén speed is usually much smaller than the particle velocity, the above equation can be approximated to $r_g \cos \theta \simeq \lambda/2\pi$, which implies that only resonant waves whose wavelength is comparable to particle's Larmor radius can efficiently interact with the particle. Indeed, if $\lambda \gg r_g$, the particle will tightly follow the field line and the pitch angle will go back to the original one after the particle passing through the wave packet. While in the case $\lambda \ll r_g$, the particle

can hardly be affected by the magnetic field perturbation. As the particle passes through the resonant wave, the change of particle's momentum in the z -direction reads

$$\begin{aligned}
\delta p_z &= \int_0^{t_0} dt F_z \\
&= \frac{1}{2} \frac{ev_\perp \delta B}{c} t_0 \cos(kz_0 - \phi) \\
&\simeq \frac{\pi ev_\perp \delta B}{c\Omega} \cos(kz_0 - \phi) \\
&= \pi p \sin\theta \left(\frac{\delta B}{B_0} \right) \cos(kz_0 - \phi)
\end{aligned} \tag{1.5}$$

where t_0 is the time it takes for the particle passes through the wave packet, and we assume that the length of the wave packet equal to the length of the wave, i.e., $L = \lambda$, again using the approximation that $t_0 = L/(v_z - v_A) \simeq L/v_z = 2\pi/kv_z$. On the other hand, since the energy of the particle is conserved in the wave frame, we have

$$\delta p_z = \delta(p \cos\theta) = -p \sin\theta \delta\theta = \pi p \sin\theta \frac{\delta B}{B_0} \cos(kz_0 - \phi) \tag{1.6}$$

and we arrive at

$$\delta\theta = -\pi \frac{\delta B}{B_0} \cos(kz_0 - \phi) \tag{1.7}$$

Although the particle's energy is conserved in the wave frame, as the pitch angle has changed after passing through the wave packet, its energy in the lab frame would also be changed.

During a time t , t/t_0 such interactions are expected to happen and hence give a diffusion rate as a function of pitch angle as

$$D_\theta \equiv \left\langle \frac{\Delta\theta^2}{2t} \right\rangle = \frac{\pi}{8} \Omega \left\langle \left(\frac{\delta B}{B} \right)^2 \right\rangle \tag{1.8}$$

Let us denote the ratio of the energy density of the turbulent magnetic field energy density to that of the background magnetic field by ξ and assume a power-law form of turbulent wave spectrum, say, $I(k) = I_0 k^{-q}$. Then we can get $I_0 = C\xi B^2 k_{\min}^{q-1}$ where C is a constant and k_{\min} is the smallest wavenumber of the turbulent wave which corresponds to the longest wavelength $\lambda_{\max} \simeq 1/k_{\min}$. Given $\delta B^2 \simeq \Delta k I(k) \simeq k I(k)$, we find

$$D_\theta = \xi c r_g^{q-2} \lambda_{\max}^{1-q} \tag{1.9}$$

Here we have dropped the constant which is not far from unity. The time required for particle isotropization, or for a large angle scattering to occur, τ , can then be

obtained by letting $D_\theta \sim 1$

$$\tau = \xi^{-1} \left(\frac{r_g}{c} \right) \left(\frac{r_g}{\lambda_{\max}} \right)^{1-q} \quad (1.10)$$

Here we use the relation that $r_g \simeq 1/k$. The mean free path of a particle is defined as

$$\Lambda \simeq v\tau \simeq \xi^{-1} r_g^{2-q} \lambda_{\max}^{q-1} \quad (1.11)$$

In the above derivation, we assumed that the length of the wave packet is equal to the wave length, i.e., $L = \lambda$. If the wave packet is n times the wavelength, the change in $\langle \Delta\theta^2 \rangle$ would be n^2 times larger. However, in that case, the time for the particle to pass through the wave packet is also n times larger and Δk is also n times smaller. Due to this effect, the diffusion coefficient is independent on n .

We hereby point out that interactions between waves and particles can also induce wave damping or wave growth. But here we will use a test-particle approximation and neglect the feedback from particles to waves.

Microscopic Analysis

Basically, there are three types of Fermi acceleration: 1st-order Fermi acceleration which is well known as the shock acceleration; 2nd-order Fermi acceleration, which is the original idea of Enrico Fermi and is also called stochastic acceleration; and shear acceleration, a less discussed mechanism in literatures which considers the acceleration of a particle when it travels inside a shearing flow. This scenario will be one of the focuses of this dissertation. Microscopic analysis is usually taken to understand the physics behind these processes. Let us consider a charged particle with Lorentz factor γ and velocity β (in units of the speed of light) colliding with a moving scattering center with Lorentz factor Γ_s and velocity β_s . Denote the angle between the velocity of the particle and that of the scattering center by θ . Then we can write the Lorentz factor of the particle in the frame of the scattering center as

$$\gamma' = \Gamma_s \gamma (1 - \beta \beta_s \cos \theta) \quad (1.12)$$

Here primed quantities represent the value measured in the frame of the scattering center. After scattering, the Lorentz factor of the particle in the wave frame remains the same, but the angle between the particle velocity and the scattering center velocity changes to θ'_1 in the wave frame. Therefore, the Lorentz factor of

the particle measured in the lab frame will be

$$\gamma_1 = \Gamma_s \gamma' (1 + \beta' \beta_s \cos \theta'_1) \quad (1.13)$$

Since the particle is usually ultra-relativistic, we take $\beta, \beta' \rightarrow 1$ and substitute the expression of γ' into that of γ_1 , and obtain

$$\gamma_1 = \Gamma_s^2 \gamma (1 - \beta_s \cos \theta) (1 + \beta_s \cos \theta') \quad (1.14)$$

Thus, the change in energy of the particle after leaving the scattering region is then

$$\Delta \gamma = \gamma \frac{\beta_s^2 - \beta_s \cos \theta + \beta_s \cos \theta' - \beta_s^2 \cos \theta \cos \theta'}{1 - \beta_s^2} \quad (1.15)$$

To calculate the average energy change in one scattering, we need to average over both the incidence and emergence angles of the particle. In both shock acceleration and shear acceleration, the MHD waves are essentially embedded in the background flow. If the change of the velocity of the background flow dominates, the background flow should be regarded as the scattering center instead of the MHD waves. This would also cause fundamentally different geometries among the three cases. Below, we look into all these three cases. For simplicity, we will restrict the consideration to the case of an isotropic particle flux and isotropic turbulence.

In shock acceleration, the "scattering center" should be regarded as the whole downstream region, because the MHD waves are essentially embedded in the background flow. So the incidence angle distribution is

$$\frac{dn}{d\cos\theta} = -2\cos\theta, \quad -1 < \cos\theta < 0 \quad (1.16)$$

Energies of particles viewed in the upstream region will increase once they are isotropized in the downstream region. But these particles need to return to the upstream region again for continuous acceleration. By passing through the shock from the downstream region to the upstream region, a similar distribution of the emergence angle is caused

$$\frac{dn}{d\cos\theta'_1} = 2\cos\theta', \quad 0 < \cos\theta'_1 < 1 \quad (1.17)$$

The average energy change can be given by

$$\begin{aligned}
\langle \Delta\gamma \rangle &= \int \int \Delta\gamma(\theta, \theta') \frac{dn}{d\cos\theta} \frac{dn}{d\cos\theta'} d\cos\theta d\cos\theta' \\
&= -\frac{\gamma}{4} \int \int \frac{\beta_s^2 - \beta_s \cos\theta + \beta_s \cos\theta' - \beta_s^2 \cos\theta \cos\theta'}{1 - \beta_s^2} \cos\theta \cos\theta' d\cos\theta d\cos\theta' \\
&= \left(\frac{4}{3} \Gamma_s^2 \beta_s + \frac{13}{9} \Gamma_s^2 \beta_s^2 \right) \gamma
\end{aligned} \tag{1.18}$$

For a non-relativistic shock, $\beta_s \ll 1$, so we have $\langle \frac{\Delta\gamma}{\gamma} \rangle \simeq \frac{4}{3} \beta_s$. The energy gain per cycle is proportional to the speed of the shock. That is the reason why shock acceleration is also called 1st-order Fermi acceleration. The acceleration efficiency not only depends on the energy gain per cycle, but also on the time it takes to complete one cycle. Particles may undergo several scatterings with MHD waves before they cross the shock, so the time should be longer than the mean scattering time obtained in Eq. 1.10. On the other hand, the scatterings confine particles around the shock and enables multiple crossing. One can find more details in (Bell 1978a; Bell 1978b) Let us first consider the upstream region. The distribution of particles' number density n satisfies the equation

$$\frac{\partial n}{\partial t} = \nabla \cdot (\kappa_u \nabla n) - \nabla \cdot (\vec{V}_u n) \tag{1.19}$$

$\kappa_u = \lambda c/3$ is the spatial diffusion coefficient in the upstream region assuming an isotropic diffusion and V_u is the fluid velocity of the upstream region (viewed from the frame of the shock). So the first term of the right-hand side represents the diffusion due to scattering off MHD waves while the second term for the convection with the background flow. Assuming that a plane shock propagates toward the x -axis and considering a steady state distribution, we see that

$$\kappa_u \frac{dn}{dx} = -V_u n \tag{1.20}$$

and this provides a particle distribution in the upstream region

$$n = n_0 \exp(-xV_u/\kappa_u) \tag{1.21}$$

with n_0 being the number of density of particles at the shock. Integrating the distribution from 0 to ∞ yields the column density of particles in the upstream region $n_0 \kappa_u / V_u$. On the other hand, the rate of particles encountering the shock is given by the projection of an isotropic particle flux onto the planar shock front,

say, $n_0c/4$. This gives an average residence time of a particle in the upstream region

$$t_u = (n_0\kappa_u/V_u)/(n_0c/4) = 4\kappa_u/V_uc \quad (1.22)$$

In the downstream region, we can not use the same method because a fraction of particles will be advected with the background flow farther and farther away from the shock front, making the mean residence time to infinity. What we are interested in is the mean residence time of particles that will return back to upstream. Consider a convection–diffusion equation with a source located at $x_0 (< 0, \text{in the downstream})$ and with an absorbing boundary at the shock front ($n(0) = 0$)

$$\frac{\partial n}{\partial t} = \nabla \cdot (\kappa_d \nabla n) - \nabla \cdot (\vec{V}_d n) + Q\delta(x - x_0) \quad (1.23)$$

where V_d is the fluid velocity in the downstream region and Q is the total amount of injected particles at x_0 . The steady state solution reads

$$n(x) = \begin{cases} \frac{Q}{V_d} [\exp(-V_dx/\kappa_d) - 1] \exp(V_dx_0/\kappa_d), & 0 \leq x \leq x_0 \\ \frac{Q}{V_d} [1 - \exp(V_dx_0/\kappa_d)], & x_0 < x \end{cases} \quad (1.24)$$

and the flux towards the shock front is

$$\kappa_d \frac{\partial n}{\partial x} = Q \exp(V_dx_0/\kappa_d) \quad (1.25)$$

The above equation indicates that a fraction $\exp(V_dx_0/\kappa_d)$ of the injected particles at x_0 will go back to the shock front, and gives the total column density of particles that will return downstream by

$$\int_{-\infty}^0 \exp(V_dx_0/\kappa_d) n dx_0 = \kappa_d n_0 / V_d \quad (1.26)$$

Thus the average residence time of a particle in the downstream region is

$$t_d = (n_0\kappa_d/V_d)/(n_0c/4) = 4\kappa_d/V_dc \quad (1.27)$$

which is identical to that in the upstream region. So the total average time for one cycle is $\Delta t = t_u + t_d = \frac{4}{c} \left(\frac{\kappa_u}{V_u} + \frac{\kappa_d}{V_d} \right)$ and hence the acceleration time is

$$t_{\text{acc,shock}} = \frac{\Delta t}{\Delta\gamma/\gamma} = \frac{3}{v_s} \left(\frac{\kappa_u}{V_u} + \frac{\kappa_d}{V_d} \right). \quad (1.28)$$

The acceleration efficiency is highly dependent on the shock velocity v_s . However, note that this does not make a relativistic shock with $v_s \simeq c$ a powerful particle

accelerator. The reason is that, as first realized by Gallant & Achterberg (1999; and also see, e.g., Derishev et al. 2003), the shock is so fast that it will catch up with the particle that returns to the upstream region when the particle just deflects a small angle of $\sim 1/\Gamma_s$, relative to the shock normal, while maintaining a Γ_s^2 energy gain would require isotropization of particles in the upstream region. Therefore, a mildly-relativistic shock may optimize the acceleration efficiency. Otherwise some extra mechanism, such as the converter acceleration mechanism (Derishev et al. 2003), or generation of strong micro-scale turbulences near the shock front (e.g., Lemoine et al. 2006) are needed for an efficient acceleration.

In the case of stochastic acceleration, the scattering centers are just MHD waves. Assuming that these turbulence waves are also isotropic, there will be a preference for "head-on" collisions (i.e., $\cos\theta < 0$) because scattering centers that move roughly in the direction of the particles will have a smaller collision rate. The collision probability is proportional to $(1 - \beta\cos\theta)$, and so we get the distribution of incidence angles

$$\frac{dn}{d\cos\theta} = \frac{1 - \beta_s\cos\theta}{2} \quad -1 \leq \cos\theta \leq 1 \quad (1.29)$$

while the distribution of emergence angles is still isotropic,

$$\frac{dn}{d\cos\theta'} = \frac{1}{2} \quad -1 \leq \cos\theta' \leq 1 \quad (1.30)$$

Repeating the same steps for the case of shock acceleration case, we have

$$\langle\Delta\gamma\rangle = \frac{4}{3}\Gamma_s^2\beta_s^2\gamma \simeq \frac{4}{3}\beta_A^2\gamma \quad (1.31)$$

This mechanism is known as 2nd-order Fermi acceleration because the average energy gain per scattering is proportional to the square of the velocity of the scattering center. The acceleration time is then

$$t_{\text{sto.}} = \frac{9\kappa}{4\beta_A^2 c^2} \quad (1.32)$$

Comparing this to the acceleration time of shock acceleration, we can see that the acceleration efficiency in these two mechanisms basically have the same dependence on the velocities of scattering centers as well as on quantities concerning turbulence. But if we look into the energy change in each individual scattering, we find that energies of particles always increase in shock acceleration as each scattering¹ is head-on, while particles undergoing stochastic acceleration can

¹for shock acceleration, a scattering should be regarded as one downstream-upstream cycle

either gain or lose energy in each scattering, although a net gain will occur after many scatterings. This implies that particles diffuse in the momentum space and the diffusion coefficient can be found as follows

$$D_p = \left\langle \frac{\Delta p^2}{\Delta t} \right\rangle = \frac{2\beta_A^2 p^2}{3\tau} \quad (1.33)$$

or

$$D_\gamma = \frac{2\beta_A^2 \gamma^2}{3\tau} \quad (1.34)$$

in terms of the Lorentz factor. Stochastic acceleration could be very efficient for relativistic Alfvén waves. But it is not clear whether relativistic Alfvén waves do exist in the astrophysical objects that satisfy the Hillas criterion.

Shear acceleration is more complicated, as the velocity of scattering centers depend on the incident particle's velocity and the given shear profile of the outflow. This mechanism is firstly proposed by Berezhko and his collaborators (Berezhko 1981; Berezhko & Krymskii 1981), and is gradually developed by other scientists such as Webb (1985), Earl et al (1988), Jokipii (1990), Ostrowski (1998), Rieger & Duffy (2004) and etc. But comparing with shock and stochastic acceleration, this mechanism is much less discussed in literatures. We will show later this mechanism is a very powerful mechanism of acceleration high energy particles. Here we introduce the basic idea of this mechanism, following the treatment of Jokipii (1990) for a non-relativistic longitudinal shearing flow. Consider a flow moving along the z -axis with velocity $u = u(x)\vec{e}_z$ of a shear in the x -axis. A particle with momentum p moving along a certain direction with a pitch angle θ , and ϕ is the angle between x -axis and the projection of the velocity of the particle in the xy -plane, i.e., $\tan\phi = v_y/v_x$. A particle moves a distance in x -axis between two scatterings. The velocity difference between the initial background flow and the new background flow is

$$\delta\vec{u} \equiv \vec{u}' - \vec{u} = \delta u \vec{e}_x = \frac{\partial u(x)}{\partial x} \delta x \vec{e}_x = \frac{\partial u}{\partial x} \frac{p}{m} \sin\theta \cos\phi \tau \vec{e}_x \quad (1.35)$$

where $m = \gamma m_0$ is the relativistic mass of the particle with γ being the particle's Lorentz factor and m_0 the rest mass. So p/m is the particle's velocity, and denoted by v . In the rest frame of the flow where the particle is isotropized, its momentum is given by

$$\vec{p}' = \vec{p} - m\delta\vec{u}, \quad (1.36)$$

so

$$p' = p \left[1 + \frac{\delta u^2}{v^2} - \frac{2\delta u}{v} \cos\theta \right]^{1/2} \quad (1.37)$$

Expanding the equation to the second order of u/v , we have

$$p' = p\left(1 + \frac{1}{2} \frac{\delta u^2}{v^2} \sin^2 \theta - \frac{\delta u}{v} \cos \theta\right) \quad (1.38)$$

and substituting the expression of δu into the above equation will give

$$\Delta p \equiv p' - p = \frac{1}{2} \left(\frac{\partial u}{\partial x}\right)^2 \tau^2 \sin^4 \theta \cos^2 \phi - \frac{\partial u}{\partial x} \tau \sin \theta \cos \theta \cos \phi \quad (1.39)$$

Assuming that the distribution of $\cos \theta$ and ϕ is isotropic, say

$$\frac{dn}{d\cos\theta d\phi} = \frac{1}{4\pi}, \quad -1 < \cos\theta < 1 \text{ \& } 0 < \phi < 2\pi, \quad (1.40)$$

we can get the average energy change in one scattering to be

$$\langle \Delta p \rangle = \int_0^{2\pi} \int_0^\pi \frac{dn}{d\cos\theta d\phi} \Delta p \sin\theta d\theta d\phi = \frac{2}{15} \left[\frac{\partial u(x)}{\partial x} \right]^2 p \tau^2 \quad (1.41)$$

Similar to the stochastic acceleration, the mean scattering time is τ , and the average acceleration rate and momentum diffusion coefficient are

$$\left\langle \frac{\Delta p}{\Delta t} \right\rangle = \frac{\int_0^{2\pi} \int_0^\pi \Delta p \sin\theta d\theta d\phi}{\tau \int_0^{2\pi} \int_0^\pi \sin\theta d\theta d\phi} = \frac{2}{15} \left[\frac{\partial u(x)}{\partial x} \right]^2 p \tau \quad (1.42)$$

and

$$D_p = \left\langle \frac{\Delta p^2}{\Delta t} \right\rangle = \frac{\int_0^{2\pi} \int_0^\pi \Delta p^2 \sin\theta d\theta d\phi}{\tau \int_0^{2\pi} \int_0^\pi \sin\theta d\theta d\phi} = \frac{1}{15} \left[\frac{\partial u(x)}{\partial x} \right]^2 p^2 \tau \quad (1.43)$$

Interestingly, in contrast to shock acceleration and stochastic acceleration, the average acceleration rate in shear acceleration increases with the particle's energy, implying that the higher the energy of the particle, the easier it gains energy. This is because higher energy particles can travel a longer distance before being isotropized, while a longer distance results in a larger velocity difference in background flow, in other words, a higher scattering center speed and hence leads to a larger energy increase. This would make shear acceleration a promising mechanism for accelerating high energy particles. Besides, for particles traveling among different regions of a flow with a relativistic velocity difference, the isotropization problem is not as pronounced as in the shock acceleration case. For example, given a longitudinal shearing flow, particles enter a new inertial frame from the sides.

1.1.2 Other Acceleration Mechanism

Unipolar Inductor

A unipolar inductor is generated by rotating magnetic fields, such as those in pulsars and rotating black holes. The combination of strong magnetic fields and rotational energy establishes a strong electric field by $\vec{E} = -\vec{v} \times \vec{B}/c$ between the root of magnetic field lines and infinity. In the relativistic wind of a fast-rotating magnetar, the maximum energy of a charged particle can reach (Arons 2003; Kotera & Olinto 2011)

$$E \sim 10^{21} \text{eV} Z \frac{\eta}{0.1} \frac{B}{10^{15} \text{G}} \left(\frac{R}{10 \text{km}} \right)^3 \left(\frac{\Omega}{10^4 \text{s}^{-1}} \right)^2 \quad (1.44)$$

where η is the fraction of the voltage drop experienced by a particle with charge number Z and R is the radius of the magnetar.

Magnetic Reconnection

A magnetic reconnection event is the topological reconfiguration of a magnetic field structure. Highly conducting plasma inflows with oppositely orientated magnetic fields encounter each other and form a current sheet. Dissipation occurs along the current sheet and makes field lines reconnect. Magnetic tension along the direction of the reconnected magnetic field lines then drive plasma outflows. This process gives rise to a net local electric field $E \sim LB$ where L is the size of the reconnection region which can accelerate charged particles. In addition, particles can also gain energy by traveling back and forth several times across the two converging plasma inflows, similar to shock acceleration. This phenomenon commonly occurs in the sun and solar winds, and has also been suggested to occur in the magnetosphere of pulsars (de Gouveia Dal Pino & Lazarian 2000), pulsar winds (Coroniti 1990; Lyubarsky & Kirk 2001, Lyubarsky 2003), and in GRB outflows (Thompson 2006), and to be responsible for the acceleration of UHECRs.

1.2 Candidate Sources

One basic requirement for UHECRs sources is that the size R of the source should be larger than the Larmor radius or the gyroradius, r_g , of the particles, otherwise the particles will efficiently escape the source before it acquires the energy. So

theoretically, the maximum particle energy in the source is given by $E_{\max} < ZeBR$ where B is the magnetic field in the source and e the electron charge. This is also termed "Hillas criterion" or "Hillas condition" as it was first suggested by Hillas (1984). As shown in Fig. 1.1, different astrophysical objects are placed in a $R - B$ plane and there are not many that can satisfy the criterion, even assuming UHECRs are iron nuclei. We note that the Hillas criterion is only a necessary but insufficient condition for acceleration. More accurate maximum achievable energy depends on the detailed acceleration mechanism, which is required to overcome the cooling and escape process of particles which can stop the acceleration.

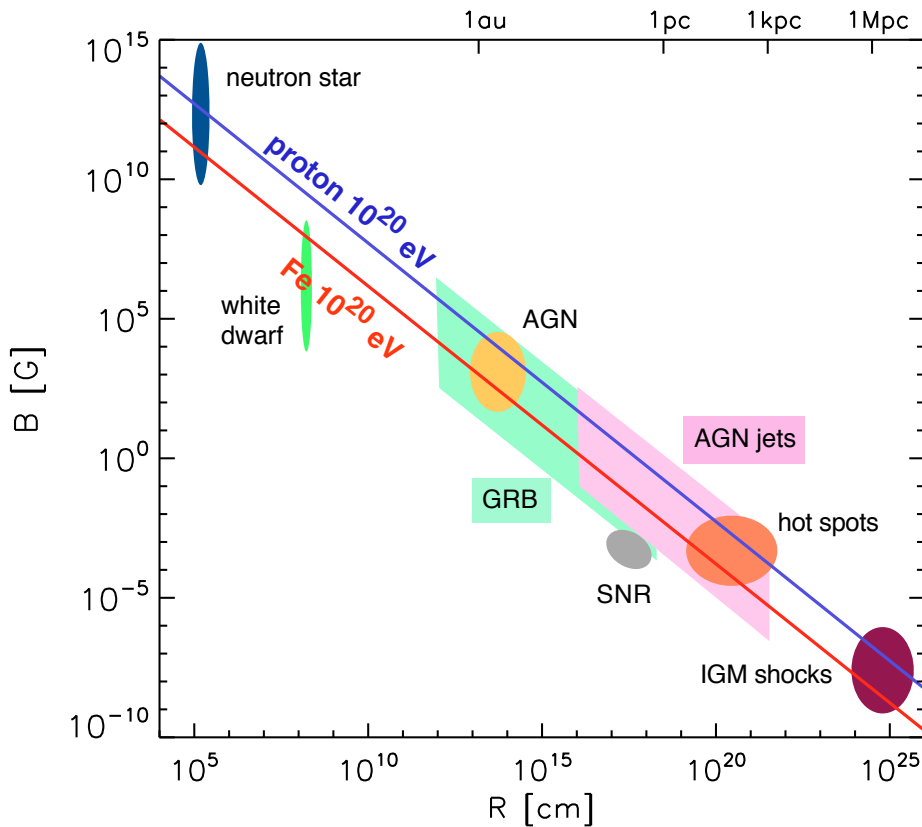


Figure 1.1: A Hillas diagram from Kotera & Olinto (2011). The blue (red) line shows conditions for confinement of protons (iron nuclei) with energy of $E_{\max} = 10^{20}$ eV. Various candidate sources with uncertainties in parameters are shown with colored region.

The most frequently discussed sources are radio-loud Active Galactic Nuclei

(AGN) and gamma-ray bursts (GRB). Both objects are believed to consist of a black hole accretion disk launching a high speed outflow or jet, but at different sizes and timescales. An AGN is a compact region located at the center of a galaxy, observable in various bands. It is persistently powered by accretion of gas onto massive black holes of 10^6 – 10^{10} times solar mass for a few million years or even longer. Dipolar jets are launched from the accretion disk and can extend to a distance of kpc–Mpc from the central black hole. Some powerful AGNs with kinetic jet power even beyond 10^{46} erg/s, e.g., Farnoff-Riley II galaxies, show hot spots at the far end of their jets which result from the interaction between jets and the intergalactic medium, and are expected to generate strong shocks and may accelerate particles to ultrahigh energies (e.g., Rachen & Biermann 1993; Berezhko 2008). Stochastic acceleration mechanisms and shear acceleration mechanisms may also work to accelerate UHECRs inside the jets. A detailed discussion on particle acceleration will be presented later.

In contrast to AGNs, which are the most powerful persistent sources in the Universe, GRBs are the most powerful transient sources and the most intense explosions since the big bang. They can release 10^{51} – 10^{54} erg of energies from the X-ray to gamma-ray bands within only a few seconds. These "monsters" are thought to originate from the deaths of massive stars or mergers of neutron star–neutron star binaries or neutron star–black hole binaries. A stellar-mass level black hole is formed inside the debris and engulfs the rest of the gas at an enormous rate of $1 - 10 M_{\odot}/s$ and gives rise to an ultra-relativistic jet of Lorentz factor ~ 100 – 1000 . In the popular "internal shock" model (Rees & Mészáros 1994), collisions among different parts of the jet which have different bulk velocities will form mildly-relativistic shocks at a distance of 10^{13} – 10^{15} cm from the explosion center and produce the observed GRB. After this phase, all the ejecta will combine into one when it encounters the ambient interstellar medium, an ultra-relativistic shock consequently forms and produces the afterglow. Protons and nuclei in principle could be accelerated to ultrahigh energies in both the internal shock and the external shock (e.g., Vietri 1995; Waxman 1995).

As shown in Fig. 1.1, some other sources also meet the Hillas criterion and have been suggested to be UHECR sources. Intergalactic shocks are usually considered as a potential source. They are generated when clusters of galaxies collide, or when accretion gas supersonically falls toward the center of clusters of galaxies and encounters the content therein. The typical size of an intergalactic shock is $1 - 10$ Mpc and the magnetic field downstream may be amplified to

$1\ \mu\text{G}$ (van Weeren et al. 2010). Although there is no problem in confinement of UHECRs for an intergalactic shock, a detailed calculation (Vannoni et al. 2009) showed that given a realistic shock speed of a few thousand km/s and a magnetic field of $1\ \mu\text{G}$, the maximum proton energy is not able to exceed a few times 10^{19}eV due to pion-production loss on CMB.

Semi-relativistic hypernovae are a peculiar type of supernovae which are brighter and have higher explosion energies than typical ones. Several events have been observed in the nearby universe to date, usually associated with low-luminosity GRBs. SN 1998bw, associated with GRB 980425, is the first peculiar supernova found at a distance of 38 Mpc, with an isotropic-equivalent total kinetic energy of $\sim 5 \times 10^{52}\text{erg}$ (Galama et al. 1998; Kulkarni et al. 1998; Iwamoto et al. 1998). The radio afterglow of this event showed that more than 10^{50}erg of kinetic energy was released in the form of a mildly relativistic ejecta. Similar to supernova remnants, when the ejecta of hypernovae encounter the interstellar medium, mildly-relativistic shocks are formed and accelerate particles. Although hypernova remnants may not be able to accelerate protons above a few times 10^{18}eV (Wang et al. 2007), intermediate-mass nuclei such as carbon, nitrogen and oxygen nuclei and heavy nuclei such as iron nuclei can be accelerated beyond 10^{20}eV given that the maximum energy in the shock acceleration is proportional to charge number of particle. The progenitors of hypernovae are believed to be Wolf-Rayet stars which have been stripped of their original H-rich and sometimes even He-rich envelopes. Their circum-stellar winds are therefore rich in intermediate-mass elements. Moreover, the hypernova ejecta contain heavy elements that are produced by nuclear fusion in the core as well as elements heavier than Fe that are synthesized during the explosions. Note that a nuclei-dominated composition of UHECRs at highest energies is consistent with the measurement of the PAO.

Fast-rotating magnetars are another possible sources for UHECRs. Their birth accompany massive core-collapse supernovae. In combination with fast rotation and a strong magnetic field, a huge electric potential difference can be induced between the surface of the magnetar and infinity. Charged particles that undergo a fraction of the potential drop can be accelerated to ultrahigh energies. However, the acceleration in the magnetosphere of a neutron star will be severely limited by energy loss of curvature radiation radiation (Aharonian et al. 2002; Arons 2003). An alternative of feasible acceleration zone is the relativistic winds outside the light cylinder. A comparable voltage drop can be produced there

(Blasi et al. 2000; Arons 2003) and given the larger radius of curvature of magnetic field lines there, the curvature radiation loss is not important (Arons 2003). Due to its iron-rich surface, a magnetar is able to inject large amount of heavy nuclei into the acceleration region. It is found that to account for the measured UHECR flux, about 5% of the extragalactic magnetar population have to be fast-rotators (Fang et al. 2012). Since the maximum particle acceleration energy depends on the rotation speed, ultrahigh energies can only be achieved at an early phase for the rotation energy will convert into kinetic energy of launched relativistic winds soon. Thus, similar to GRBs, magnetars are transient UHECR sources.

Despite that theorists can create many plausible models for the origin of UHECRs, only observations can give decisive conclusion. Although current measurements are far from clear, thanks to multi-annual operations of the Pierre Auger Observatory (PAO) and Telescope Array experiment (TA), great progress has been made in the measurement of UHECRs. In the following part, we will briefly overview the detection technique and the latest results of these two experiments.

1.3 Extensive Air Shower and Detection Technique

UHECRs are detected via the extensive air showers (EAS) generated when they arrive at the Earth and interact with molecules in the atmosphere. More specifically, one primary UHECR particle, usually a proton or a nucleus, hits the air molecules and produces lots of secondary particles most of which are pions. About 2/3 of the generated pions are charged ones. They can decay into muons, electron/positron pairs and neutrinos, but due to their relatively long lifetimes, they may interact with other air molecules before decaying. These subsequent interactions basically create the same products, albeit less energetic, as the previous one and cascade the energy of the primary cosmic ray particle to more and more secondary particles until they are not energetic enough to produce new particles, a process which is also called a "hadronic shower". The remaining 1/3 of the pi-mesons (pions) are neutral pions which have much shorter lifetimes compared to the charged ones. Almost all of them will decay into gamma rays before the next collision, initiating an "electromagnetic shower". The generated gamma rays will interact with nuclei or electrons in air molecules and produce electron/positron pairs, which will in turn produce gamma rays via the Bremsstrahlung process. The cascading process will continue until the photon

energies fall below the pair production threshold. Note that a hadronic shower will keep producing neutral pions and hence also leads to secondary electromagnetic showers as it proceeds. A schematic figure of shower development is shown in Fig. 1.2.

Heitler (Heitler 1954) developed a toy model for electromagnetic showers before the shower maximum. In this model, the cross sections of collisions are assumed to be independent of particle energy. Energy is also conserved in the collision. Another assumption is that both photons and electrons/positrons will split into two particles of equal energy through pair production or Bremsstrahlung after a fixed distance d , which is given by $d = \lambda_r \ln 2$ with $\lambda_r = 37 \text{ g cm}^{-2}$ being the radiation length in air. The total number of secondary particles is increasing as the extensive air shower (EAS) is developing until the average energy of the secondary particles is insufficient to produce more particles. Usually, the atmospheric depth that the shower penetrates after the primary UHECR particle has entered the atmosphere is denoted by X and its maximum by X_{max} . Given the density of the atmosphere, this depth is usually expressed in units of g/cm^2 . Thus, after N steps, the shower crosses a distance of $X = nd$ and the total number of particles in the shower is 2^n . Denoting the critical energy of particles at the shower maximum by E_c^{em} , which is related to the absorbing medium and is about 85 MeV in the atmosphere, and the energy of the primary particle by E_0 , the total number of particles at shower maximum can be written as E_0/E_c^{em} . The penetration depth of the primary particle at the shower maximum is then

$$X_{\text{max}}^{\text{em}} = \lambda_r \ln \frac{E_0}{E_c^{\text{em}}} \quad (1.45)$$

Another important quantity is the change of X_{max} per decade in energy, i.e., $D_{10} \equiv dX_{\text{max}}/d \lg E_0$, which is also known as the elongation rate. If the incidence particle is a photon,

$$D_{10}^{\gamma} = \lambda_r \ln 10 = 85 \text{ g cm}^{-2} \quad (1.46)$$

Hadronic showers are more complicated, but Heitler's model can still be applied with some modifications (Matthew 2005). An incident proton with energy E_0 and its secondary particles are assumed to interact with air molecules by propagating a distance of $d = \lambda_l \ln 2$ to produce $2N_{\pi}$ charged pions and N_{π} neutral pions with equal energy. Neutral pions will induce an electromagnetic shower and hence we do not need to consider its further products. After n steps, the total energy remaining in the hadronic shower is $(2/3)^n E_0$ while the total number of particles is $(2N_{\pi})^n$ so the energy of each pion is $E_0/(3N_{\pi})^n$. Supposing

that the cascade ceases when the energy of produced pions drops to E_c^π , and only considering the first hadronic interaction and the subsequent electromagnetic showers, the shower maximum is given by (Matthew 2005)

$$X_{\max} = \lambda_l \ln 2 + \lambda_r \ln \left(\frac{E_0}{6N_\pi E_c^\gamma} \right) \quad (1.47)$$

Energy dependence is usually presented in the form of λ_l as

$$\lambda_l = 90 - 9 \lg \left(\frac{E_0}{\text{EeV}} \right) \text{g cm}^{-2} \quad (1.48)$$

where a proton air cross section of 550 mb at 1 EeV and an increase rate about 50,mb per decade of energy is assumed in the above equation (Ulrich et al. 2009). Thus, the elongation rate for a proton-initiated hadronic shower is $D_{10}^p \simeq 62 \text{g cm}^{-2}$.

If the incidence particle is a nucleus with atomic mass A , it is usually treated as the superposition of the A protons with individual energy E_0/A . At the same energy, heavier particles will develop showers faster and hence have smaller penetration depths at shower maximum, which can be approximated with a good accuracy as an offset with respect to proton showers

$$X_{\max}^A(E_0) = X_{\max}^p(E_0/A) = X_{\max}^p - \lambda_r \ln A \quad (1.49)$$

After the shower has reached its maximum, the secondary particles are gradually absorbed. To give a direct impression of the EAS (Letessier-Selvon & Stanev 2011), one 10 EeV proton will penetrate a depth of $\sim 1033 \text{g/cm}^2$ from the top of the atmosphere to sea level if it enters the atmosphere vertically. It will produce about 3×10^{10} particles at sea level, 99% of which will be photons, and 85% of the total energy will be contained in electrons/positrons of energy 1-10 MeV. A small fraction of secondary particles consists of muons with an average energy of about 1 GeV which collectively carry about 10% of the total energy, a few GeV pions which account for about 4% of the total energy, and neutrinos and baryons which are responsible for the remainder. The shower covers a few km^2 on the ground. Since the shower maximum X_{\max} varies with the species and energies of primary particles, it is a crucial parameter to distinguish the chemical composition of UHECRs.

Generally, there are three types of detectors that are used to observe UHECRs: a ground array that observes the Cherenkov radiation of the fast-moving secondary particles, a ground array of scintillation detectors that can generate photo

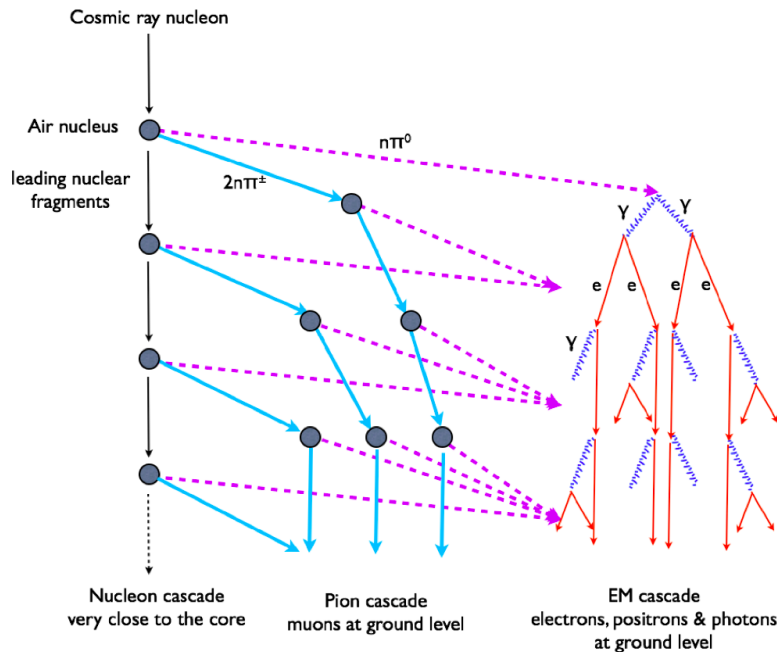


Figure 1.2: A schematic picture for the development of cascade. At each step roughly $1/3$ of the energy is transferred from the hadronic cascade to the electromagnetic one. The figure is from Letessier-Selvon & Stanev (2011).

electrons when ionizing secondary particles pass through them, and fluorescence detectors which measure the fluorescent light isotropically emitted from the Nitrogen nuclei in the air that are excited when the shower passes. The Pierre Auger Observatory (PAO) and the Telescope Array (TA) are two currently operating hybrid detectors which use two independent methods to detect UHECRs. PAO combines four fluorescence detector (FD) buildings, each of which employs 6 fluorescence telescopes along with a ground array of 1600 water tank surface detectors (SD), that observe Cherenkov radiation from secondary particles when they interact with the water. TA combines three FD stations, each of which contains 12-14 fluorescence telescopes, and 507 scintillation SDs. As hybrid detectors, the PAO and TA experiments are able to select events that trigger FD and SD simultaneously. With this technique, they can combine SD and FD data to make a better event reconstruction. As the front of an EAS that was induced by a UHECR particle reaches the SD array, the secondary particles will trigger different SDs at different time. Then according to the difference in arrival time and the geometry of the SD array, the incidence direction of the UHECR particle

can be obtained. Another important quantity is the lateral distribution function of the shower, which measures the intensity of certain secondary particles as a function of the transverse distance to the air-shower core (or the propagation axis of the incidence UHECR particle). This function is related to the energy of the incident particle (e.g. Hillas et al. 1971). After obtaining the incidence direction, the function can also be calculated according to the signal recorded in each of the SDs and their geometry, and hence the energy of the UHECR particles can be reconstructed. An SD array can not measure the shower maximum X_{\max} directly, which limits its ability to recognize the particle species.

Since the fluorescence light is emitted isotropically, FDs can detect the radiation regardless of the shower direction. Also considering that fluorescent photons come directly from their sources where the air shower passes through, one can see that FDs are good at tracing the development of the shower. The incidence direction can be reconstructed given the recorded data of a few FDs at different positions. Due to the same reason, FD can directly measure the shower maximum X_{\max} , which can be utilized to study the species or mass of the incident particle. Besides, the energy of the incident UHECR particle can be deduced from the total number of fluorescent photons which is proportional to the shower energy or the initial energy of incident particle, which is a cross check of the energy reconstruction based on the SD data.

1.4 Recent Observations of Ultrahigh Energy Cosmic Rays

Fig. 1.3 and Fig. 1.4 show the energy spectrum measured by PAO and TA, respectively. The two measured spectra are consistent with each other when considering the uncertainty in energy calibration. The both experiments exhibit an ankle around 4 EeV and a suppression of flux beyond 40-50 EeV. The spectrum data of the PAO experiment is able to be fitted by a broken power law with a smooth suppression as (The Pierre Auger Collaboration 2013a)

$$\frac{dN}{dE} \propto \begin{cases} E^{-\gamma_1}, & E < E_a \\ E^{-\gamma_2} \left[1 + \exp\left(\frac{\lg E - \lg E_{1/2}}{\lg W_c}\right) \right]^{-1}, & E \geq E_a \end{cases} \quad (1.50)$$

with $E_{1/2}$ the energy at which the energy flux drops to half of its peak value and W_c a parameter related to the steepness after the suppression. Detailed parameters are shown in Table.1.1. The TA collaboration fitted their data by

Table 1.1: The best-fit parameters for the UHECR spectrum measured by the PAO (Pierre Auger Collaboration 2013a).

Parameter	Results
$\lg(E_a/\text{eV})$	$18.72 \pm 0.01 \pm 0.02$
γ_1	$3.23 \pm 0.01 \pm 0.07$
γ_2	$2.63 \pm 0.02 \pm 0.04$
$\lg E_{1/2}/\text{eV}$	$19.63 \pm 0.01 \pm 0.01$
$\lg W_c$	$0.15 \pm 0.01 \pm 0.02$

Table 1.2: The best-fit parameters for the UHECR spectrum measured by the TA (Telescope Array Collaboration 2014)

Parameter	Results
$\lg(E_a/\text{eV})$	18.65
$\lg(E_b/\text{eV})$	19.75
γ_1	3.25
γ_2	2.81
γ_3	5.1

broken power-law (Telescope Array Collaboration 2013a)

$$\frac{dN}{dE} \propto \begin{cases} E^{\gamma_1}, & E < E_a \\ E^{\gamma_2}, & E_a < E < E_b \\ E^{\gamma_3}, & E_b < E \end{cases} \quad (1.51)$$

and the parameters are shown in Table. 1.2.

There is a consensus that UHECRs above the ankle arise from extragalactic sources, although any specific source is far from being determined, because our Galaxy can not contain such high energy particles given its size and magnetic field strengths. However, whether UHECRs below the ankle are Galactic or extragalactic is still under debate, and this leads to different explanations of the ankle-like feature. The ankle can be explained as a transition from one component of cosmic rays to another, as the feature can be naturally produced when one component drops and a new component rises to take over. Under this interpretation, it is usually regarded as a transition from Galactic to extragalactic cosmic rays, but might also be explained with a transition between two extragalactic components. On the other hand, if UHECRs are composed of only one extragalactic proton component, the ankle-like feature can be a robust result of pair production of UHECRs of energies $\sim 1 - 10 \text{ EeV}$ interacting with cosmic

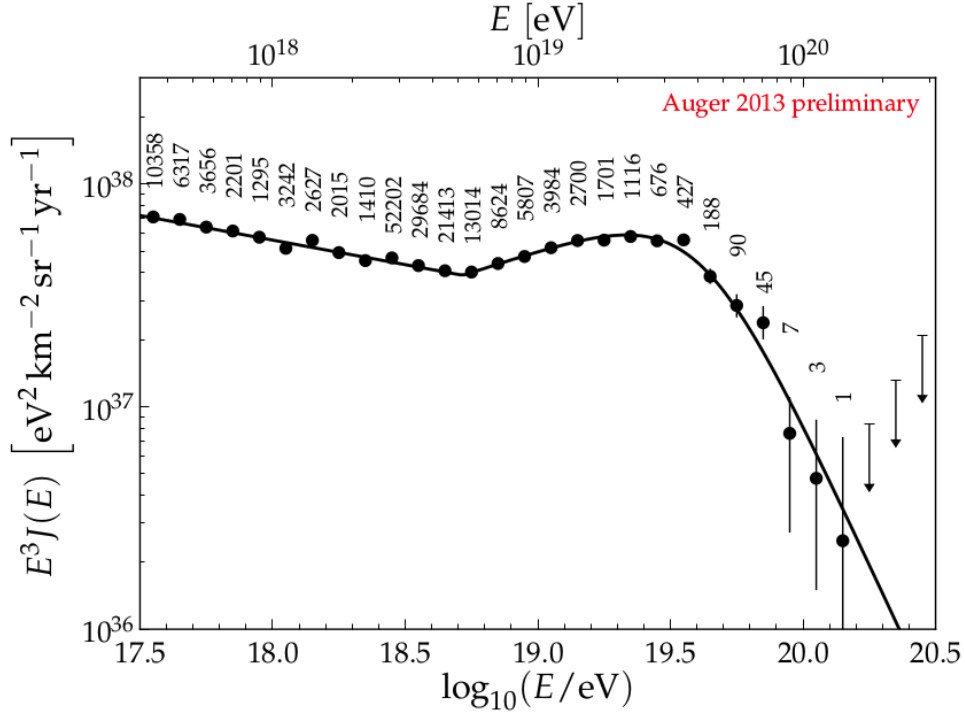


Figure 1.3: Energy spectrum of UHECRs measured by the PAO. The numbers give the number of events in each energy bin. The last three arrows represent upper limits at 84% C.L. This figure is taken from The Pierre Auger Collaboration (2013a)

microwave background (CMB) photons during their propagation because CMB photons are always there, unless the injection spectrum is softer than $\sim E^{-2.7}$. The suppression above 40 EeV is widely believed to have been caused by the attenuation of UHECRs by the background photon field during their propagation from sources to the Earth. If UHECRs are mainly made up of protons, the attenuation is due to photonpion production ($p + \gamma_{\text{CMB}} \rightarrow p/n + \pi^0/\pi^+$) on the CMB (Greisen 1966; Zatsepin & Kuz'min 1966), while if UHECRs are nuclei, the attenuation is then mainly due to photodisintegration, again by the CMB (Puget et al. 1976). Fig. 1.5 shows the attenuation length of different species of particles. This explanation also implies that the observed events with energies above the suppression should come from nearby sources given that the mean free paths of the attenuation processes for UHECRs above ~ 50 EeV is less than ~ 100 Mpc. An alternative explanation of the suppression is the limited acceleration that UHECR sources are capable of supplying. The spectrum shapes in the

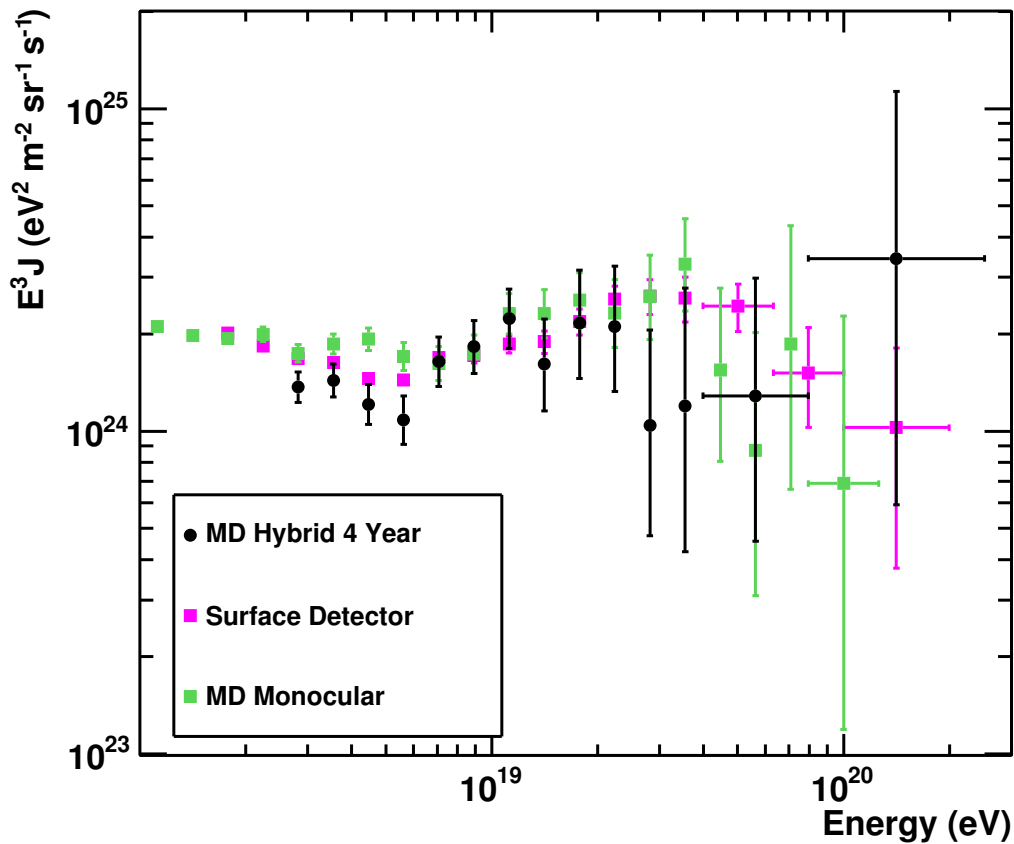


Figure 1.4: The hybrid spectrum obtained by the TA (black circles). The spectrum measured by the surface array (purple squares) and the MD monocular spectrum (green squares) is shown for reference. The figure is taken from Telescope Array Collaboration 2014

suppression region are different between these two cases. Also, the shapes of a proton-dominated spectrum and a nuclei-dominated spectrum are different. Unfortunately, the current data are not sufficient to distinguish between them. Fig. 1.6 shows the fitting to Auger data with different models.

The shower maximum X_{\max} is another crucial parameter to understand UHECRs, for it can reveal their chemical composition. X_{\max} is a function of the particle energy and particle mass (or species), as particle with more energy and less mass can penetrate deeper into the atmosphere. Once the energy of an event is reconstructed, one can determine its species from the measured shower maximum. As we mentioned above, the elongation rate (i.e. $dX_{\max}/d\lg E$) approximately only depends on the mass of the particle. So if the chemical composition of UHECRs

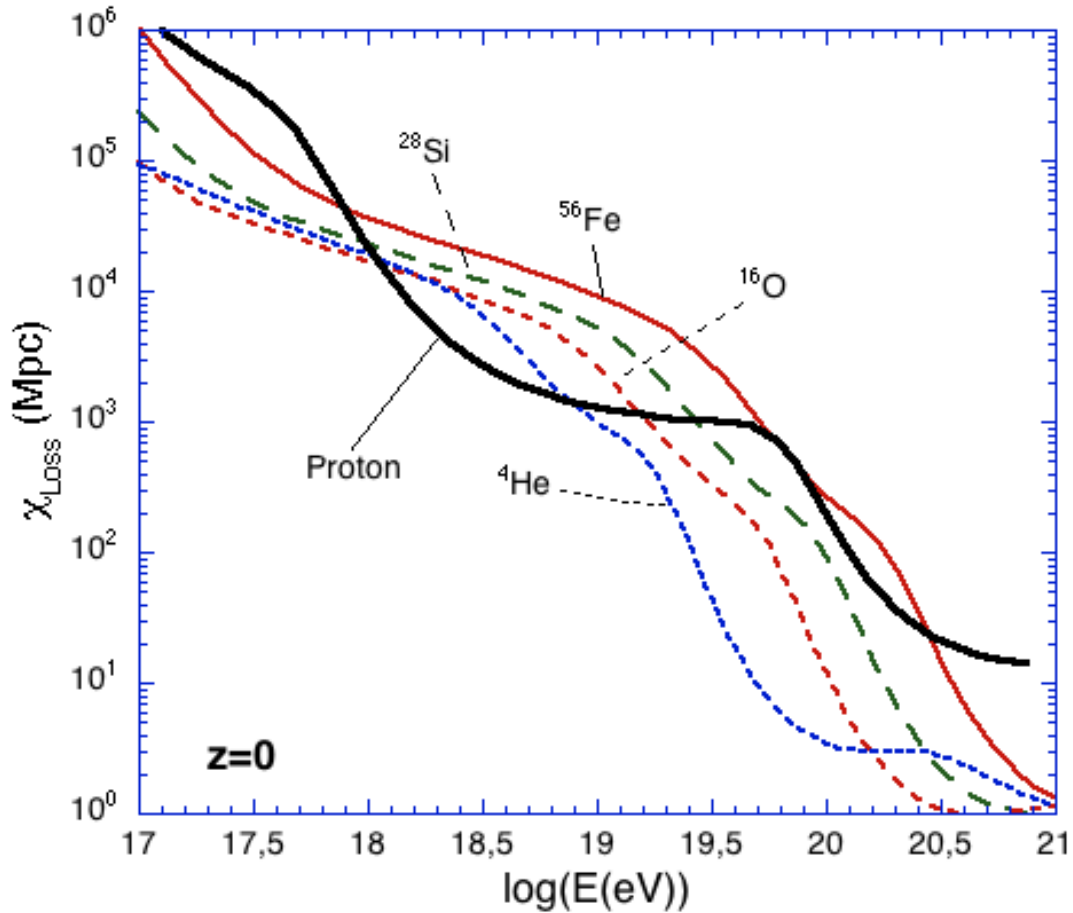


Figure 1.5: Attenuation length of different species of cosmic rays when they propagate in the intergalactic space of the local universe. The figure is taken from Allard et al. 2006

are constant, data in the $X_{\max} - \lg E$ plane should distribute along a straight line and vice versa (see. Eq. 1.51). From the left panel of Fig. 1.7, we can see that the X_{\max} measurement of the PAO suggests that the chemical composition of UHECRs gradually changes from protons to heavier nuclei beyond the ankle. A complementary and independent method to study the chemical composition is to measure the shower-to-shower fluctuations of X_{\max} , i.e. $\text{RMS}\langle X_{\max} \rangle$, which is expected to decrease with the mass of UHECR particles. As shown in the right panel of Fig. 1.7, the value of $\text{RMS}\langle X_{\max} \rangle$ implies an increasing mass above the ankle, consistent with the X_{\max} measurement. However, the measurements of TA yielded an incompatible result (Telescope Array Collaboration 2015). As shown in Fig. 1.8, both X_{\max} and $\text{RMS}\langle X_{\max} \rangle$ imply a light component of UHECR at all energies above 1 EeV. This inconsistency may be caused by different event

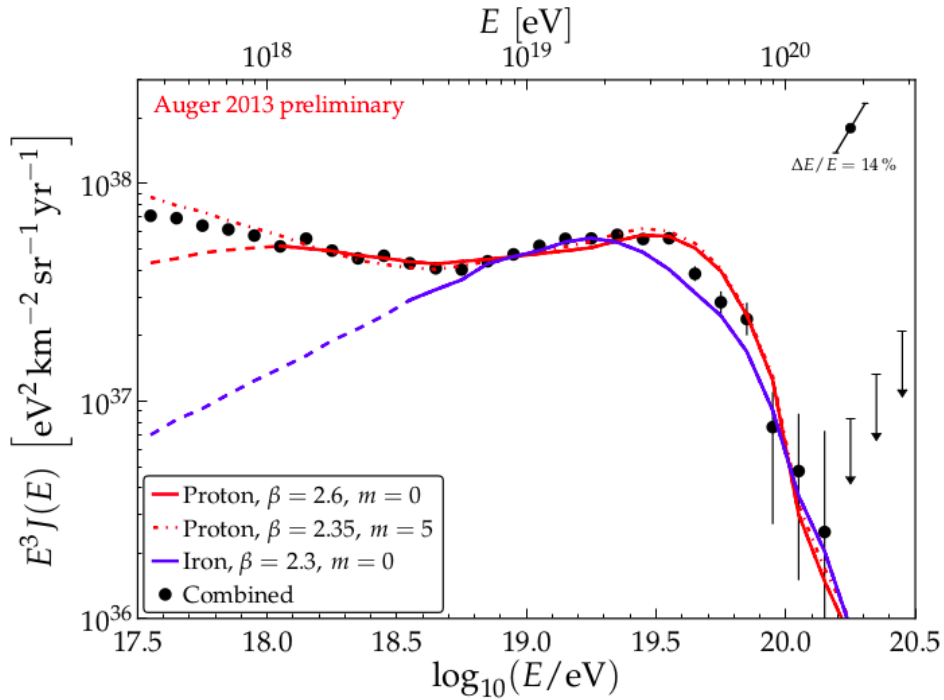


Figure 1.6: Theoretical fit to the Auger's CR spectrum. A pure proton injection (red) and an iron nuclei injection (blue) are assumed respectively. This figure is taken from The Pierre Auger Collaboration (2013a)

reconstruction and analysis techniques. Statistics may be another reason since UHECR events are very rare, especially for the TA experiment due to its smaller collection area (by about a factor of 4) and shorter operation time (by about 4 years) than the Auger experiment. On the other hand, both experiments suffer from uncertainties in their hadronic interaction model. The highest center-of-mass energy currently achieved in laboratory is 10^{17} eV, so one has to extrapolate the model for low-energy interactions up to above 10^{18} eV, while differences among different models are considerable.

Since UHECR events with energies above the flux suppression are expected to come from the nearby universe, the arrival directions of these events may include important hint regarding UHECR sources. PAO reported that (Kampert 2012) a total of 28 out of 84 UHECR events above 55 EeV were found to have been distributed within 3.1° of AGNs from the VCV catalog within 75 Mpc (see Fig. 1.9 for an sky distribution of highest energy cosmic rays in an earlier dataset).

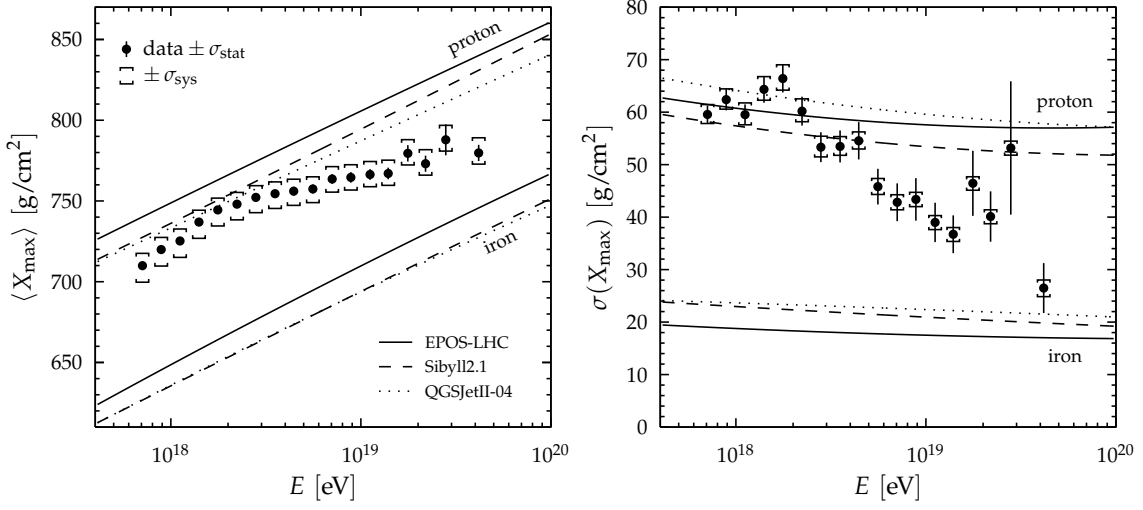


Figure 1.7: Energy evolution of X_{\max} and $\text{RMS}\langle X_{\max} \rangle$ measured by the PAO, with comparison to air-shower simulations for proton and iron primaries in different hadronic models. The figure is taken from The Pierre Auger Collaboration (2013a).

The probability of observing such a correlation from an isotropic distribution is below 1%. Most notably, there are 19 events distributed within 24° of the direction of the center of Cen A while 7.6 are expected from isotropic arrival direction, corresponding to a chance probability of about 4%. TA also reported 11 out of 25 events above 57 EeV correlating with nearby AGNs, while 5.9 are expected from random coincidence, corresponding to a probability of $\sim 2\%$. The combined PAO and TA probability of observing such a correlation is $\sim 0.1\%$. However, we should keep in mind that as UHECRs are most likely charged particles, and be careful when trying to find their sources by looking back to their arrival directions because they may be deflected significantly by magnetic field during propagation. Given the Larmor radius of a particle with energy E and charge number Z $r_g \simeq 1 \text{ kpc}(E/\text{EeV})(B/\mu\text{G})^{-1}Z^{-1}$, protons will be more or less still in their original directions, but nuclei will probably lose the information concerning their arrival directions and birth places after passing through intergalactic and Galactic magnetic fields. At lower energies, PAO found no significant deviation from isotropic distribution and reported the upper limits on dipole and quadrupole amplitudes as shown in Fig. 1.10. This challenges the model of stationary galactic sources that are distributed in the disk because they are expected to cause a stronger dipole and quadrupole component.

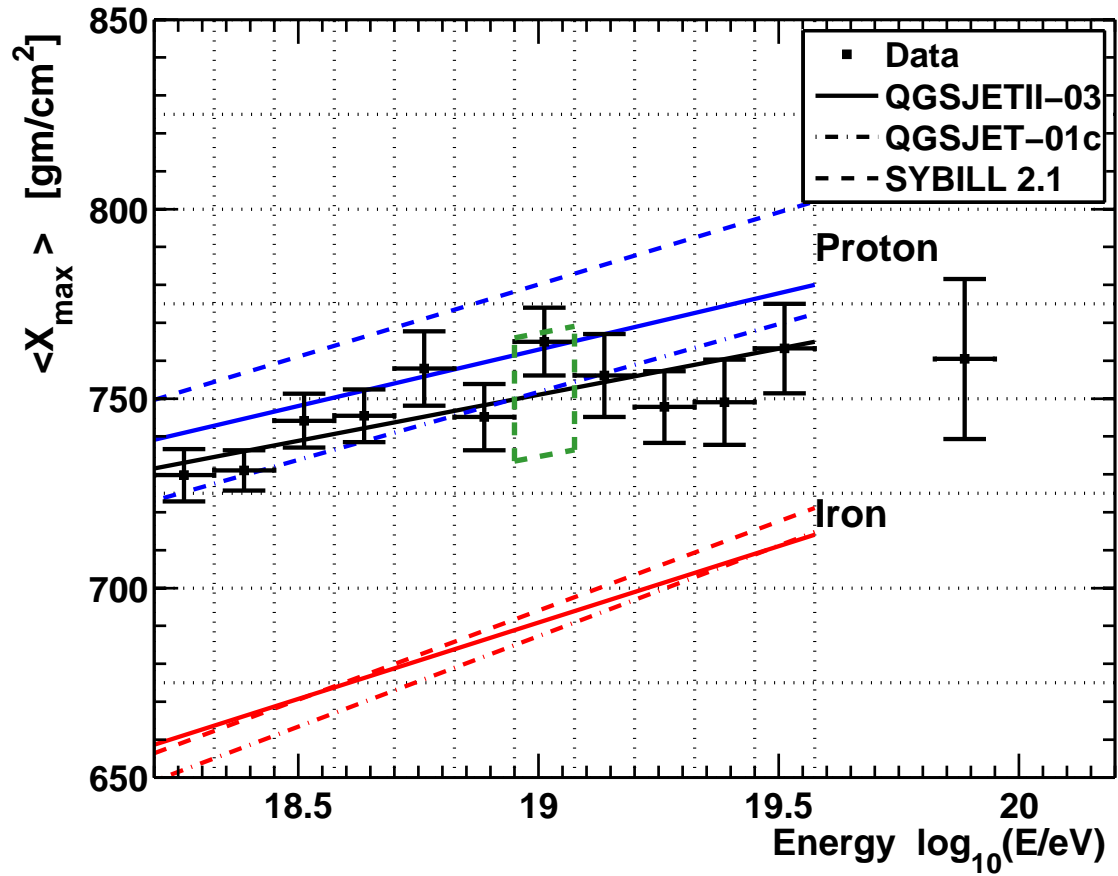


Figure 1.8: Shower maximum measurements of the TA experiment with the comparison to different hadronic models. Data are the black points with error bars. The solid black line is a fit to the data. Colored lines are fits to Monte-Carlo. Blue is proton and red is iron. The green hashed box indicates the total systematic error on $\langle X_{\max} \rangle$. The figure is taken from Telescope Array Collaboration (2015)

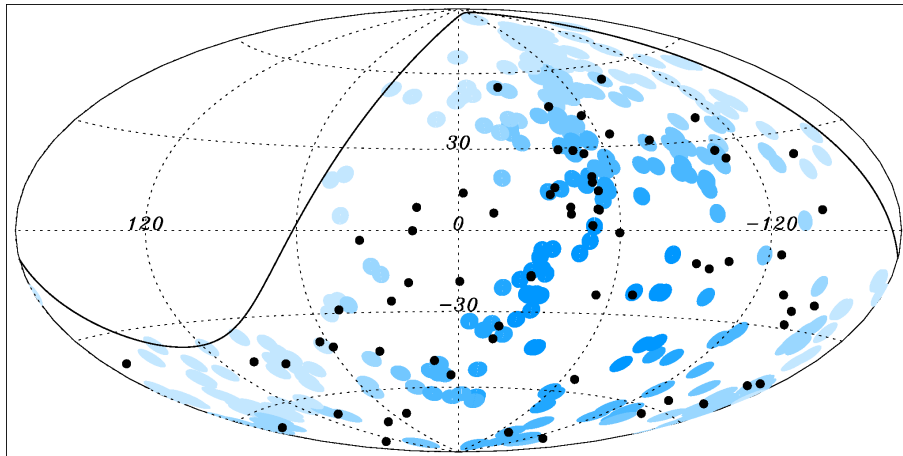


Figure 1.9: An earlier report of arrival directions of highest energy cosmic rays by the PAO (The Pierre Auger Collaboration 2010a). There are 69 events in total with energy $E \geq 55$ EeV detected up to 31 December 2009. UHECR events are plotted as black dots in an Aitoff-Hammer projection of the sky in galactic coordinates. The solid line represents the field of view of the PAO for zenith angles smaller than 60° . Blue circles of radius 3.1° are centred at the positions of the 318 AGNs in the VCV catalog that lie within 75 Mpc and that are within the field of view of the Observatory. Darker blue indicates larger relative exposure. The exposure-weighted fraction of the sky covered by the blue circles is 21%.

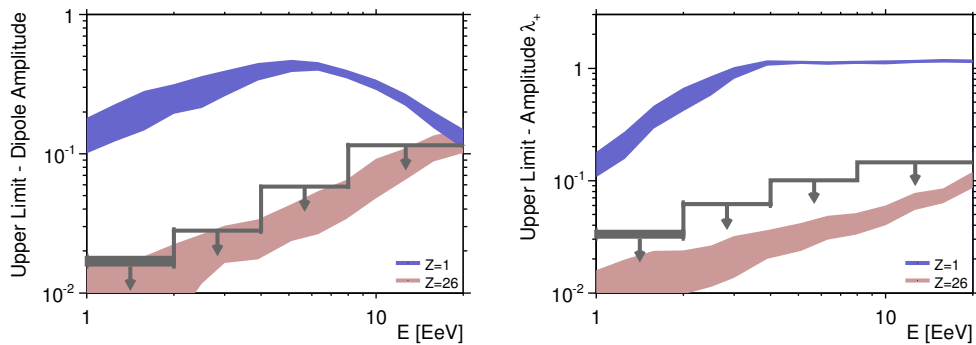


Figure 1.10: 99% *C.L.* upper limits on dipole (left panel) and quadrupole (right panel) amplitudes as a function of the energy. Theoretical anisotropy expectations from stationary galactic sources that distributed in the disk are also shown for comparison, in pure proton and iron nuclei composition cases respectively. The uncertainty of the amplitudes due to the stochastic nature of the turbulent component of the magnetic field are sampled from different simulation data sets and are shown by colored bands. The figure is taken from The Pierre Auger Collaboration (2013b)

Possible Link Between PeV Neutrinos and UHECR

As we mentioned in previous chapter, one difficulty in finding sources of UHECRs is that the arrival directions of UHECR events typically deviate strongly from their sources due to deflection in magnetic field during propagation. However, UHECRs could interact with photon fields or matter inside their sources and produce both neutral mesons and charged mesons whose decay products include photons and neutrinos: ($\pi^0 \rightarrow \gamma + \gamma$, $\pi^+ \rightarrow e^+ \nu_\mu \bar{\nu}_\mu \nu_e$, $\pi^- \rightarrow e^- \nu_\mu \bar{\nu}_\mu \bar{\nu}_e$). These neutral particles will travel to Earth straightly and if we can discover them precisely, it is then possible to pinpoint UHECRs source by looking back to arrival directions of these secondary particles. However, UHECR sources are most likely extragalactic, so due to large propagation distance, the generated secondary photons will be absorbed by CMB or EBL that permeated throughout the universe and hence can not reach us. Fortunately, secondary neutrinos may reach us without interaction thanks to their very small cross sections. Thus observations of high-energy neutrinos (> 100 TeV) have important implications for understanding the origin of PeV-EeV cosmic rays (CRs). This chapter is based on the work of Liu et al. (2014)

2.1 Detection of High-energy Neutrinos and Its Implications

IceCube is a neutrino telescope located at the south pole, with thousands of sensors distributed over a cubic kilometer of volume inside the Antarctic ice. Two PeV neutrinos were detected during the combined IC-79/IC-86 data period (IceCube Collaboration 2013a). Later, a follow-up analysis by the IceCube Collaboration (IceCube Collaboration 2013b) discovered 26 additional sub-PeV neutrinos, corresponding to a 4.3 σ excess over reasonable expectations for the

atmospheric neutrino background of $10.6_{-3.9}^{+4.5}$. This results in a single-flavor neutrino flux of $(1.2 \pm 0.4) \times 10^{-8} \text{ GeV cm}^{-2} \text{ s}^{-1} \text{ sr}^{-1}$ at PeV. More recently, 9 more events are discovered (IceCube Collaboration 2014), including a PeV neutrino, which do not make inconsistency with the previous 28 events in terms of statistics. Non-detection of higher energy events implies a cutoff or a break above 3 PeV for a hard spectrum with power-law index of $s_\nu = 2$. Alternatively, it is also compatible with a slightly softer but unbroken power-law spectrum with index $s_\nu \simeq 2.2 - 2.3$ (IceCube Collaboration 2014; Anchordoqui et al. 2013; Winter 2013).

The sky distribution of the 37 events is consistent with isotropy (IceCube Collaboration 2014), implying an extragalactic origin, although a fraction of them could come from Galactic sources (Fox et al. 2013; Neronov et al. 2013; Ahlers & Murase 2013) or Galactic halo (Taylor et al. 2014). Several possible scenarios for the extragalactic origin of these neutrinos have been discussed, including that they are ‘cosmogenic’, arising in $p\gamma$ -collisions between CRs and cosmic background photons, or that they are generated within CR sources, either in $p\gamma$ - or pp -collisions between CRs and ambient radiation fields or gas respectively (Liu & Wang 2013; Murase & Ioka 2013; Kalashev et al. 2013; Cholis & Hooper 2013; He et al. 2013; Roulet et al. 2013, Winter 2013). A cosmogenic origin for the IceCube events is excluded because the predicted PeV flux is well below the observed one (IceCube Collaboration 2013c; Roulet et al. 2013). $p\gamma$ - or pp -collisions inside sources are more promising for generating sufficient flux. Each daughter neutrino typically takes 3 and 5 percent of the parent proton’s energy in these two processes respectively (Kelner et al. 2006). Thus, to produce a 1 PeV neutrino, we require a source located at redshift z to accelerate protons to $\gtrsim (40 - 60)^{\frac{1+z}{2}}$ PeV. This is only an order of magnitude lower than the energy of the “second knee” ($4\text{-}8 \times 10^{17}$ eV), where the CRs spectral index steepens from -3.1 to -3.3. About one to two orders of magnitude higher, the spectral index flattens from -3.3 to -2.7 at the “ankle” ($\lesssim 10^{19}$ eV). Either of these two spectral features may correspond to the transition energy above which extragalactic CRs dominate over Galactic CRs (Berezinsky 2006; Katz et al. 2009). This motivates us to discuss a possible link between sources of these neutrinos and the sources of CRs with energies above the second knee, hereafter simply ultrahigh energy CRs (UHECRs) in this chapter. Note that certain kinds of extragalactic accelerators of protons up to ~ 100 PeV may be sufficient to explain the current observations. However, our interest here is whether a link could exist between the newly-detected neutrinos and UHECRs, since then these neutrinos could shed some light on the still mysterious sources

of UHECRs. We note that the reported flux is quite close to the so-called Waxman-Bahcall bound (Waxman & Bahcall 1998), a benchmark value for the extragalactic neutrino flux based on the UHECR flux, subject to some assumptions (Rachen et al. 2000). Alternative constraints on the extragalactic neutrino flux comes from observations of the isotropic background of multi-GeV gamma-rays, which is at the level of $10^{-7} \text{ GeV cm}^{-2} \text{ s}^{-1} \text{ sr}^{-1}$. It provides a robust upper limit since the gamma-rays that are unavoidably co-produced must not overwhelm this flux. If the PeV neutrinos and UHECRs indeed originate from the same sources, the neutrino spectrum should extend to $\gtrsim 10 \text{ PeV}$ without any abrupt cutoff. This would not be inconsistent with the current IceCube observations as long as the neutrino spectrum is softer than $E^{-2.2}$. Note that the source proton spectrum may not necessarily be soft as the neutrino spectrum, since in some specific scenarios, higher energy protons can have lower production efficiencies of secondary pions, and for $p\gamma$ processes, the neutrino spectrum also depends on the ambient photon spectrum. Given the likely pion-production origin of the reported neutrinos, an approximate value for the required flux of parent protons Φ_p that escape the source can be given by $\varepsilon_\nu^2 \Phi_\nu = \frac{1}{6} f_\pi (\varepsilon_p^2 \Phi_p)^1$ (Waxman & Bahcall 1998; Murase et al. 2013), where ε_ν and ε_p are the energies of the neutrino and proton respectively, and f_π is the pion-production efficiency via pp - or $p\gamma$ -collisions of the escaping CRs. Thus, sources of UHECRs that also account for the sub-PeV/PeV neutrinos need to provide a proton flux of $\varepsilon_p^2 \Phi_p = 6(\varepsilon_\nu^2 \Phi_\nu) f_\pi^{-1} \simeq 7 \times 10^{-8} f_\pi^{-1} \text{ GeV cm}^{-2} \text{ s}^{-1} \text{ sr}^{-1}$ in the 10–100 PeV energy range. This flux corresponds to a local proton energy production rate of

$$\dot{W}_{p,0} \simeq \left(\frac{c \xi_z}{4\pi H_0} \right)^{-1} \alpha (\varepsilon_p^2 \Phi_p) \simeq 10^{44.5} f_\pi^{-1} \text{ erg Mpc}^{-3} \text{ yr}^{-1} \quad (2.1)$$

where c is the speed of light, H_0 is the Hubble constant, $\xi_z \simeq 3$ is a factor that accounts for the contribution from high-redshift sources (Waxman & Bahcall 1998), and $\alpha \sim 10 - 100$ is a factor coming from normalization of the proton spectrum (e.g., for power-law index of $s_p = 2$, $\alpha = \ln(\varepsilon_{p,\text{max}}/\varepsilon_{p,\text{min}})$). Note that accelerated protons contribute to the observed CRs only if they can escape from the sources, while pion-production process at the source would remove energy from accelerated protons. Thus the energy production rate of the CRs

¹ The factor 1/8 or 1/6 relates to the pion multiplicity in interaction. For $p\gamma$ process at Δ resonance charged to neutral pion ratio is about 1:1, corresponding to the factor 1/8. While for $p\gamma$ process at higher energy and for pp process, the charged to neutral pion ratio is about 2:1, corresponding to the factor 1/6. Since these two factor are close, we use 1/6 in the following calculation for simplicity.

that escape the source can be given by $\dot{W}_{\text{CR},0} = \dot{W}_{p,0}(1 - \xi f_{\pi}^{\text{PeV}})$ with $\xi = f_{\pi}^{\text{UHE}}/f_{\pi}^{\text{PeV}}$, where f_{π}^{UHE} is the pion production efficiency of the escaping UHECRs. For comparison, the required local CR energy production rate is $\sim 10^{45.5} \text{ erg Mpc}^{-3} \text{ yr}^{-1}$ if the transition from Galactic to extragalactic CRs occurs at the second knee, and $\sim 10^{44.5} \text{ erg Mpc}^{-3} \text{ yr}^{-1}$ if the transition occurs at the ankle for $s_p = 2$ (Katz & Waxman 2009). Given the proton energy production rate for a certain class of source, the pion production efficiency needs to be in a certain range in order to simultaneously account for the observed neutrino flux, which in turn can constrain the potential sources.

The rest of this chapter is outlined as follows. First we provide a brief overview of various candidate sources of UHECRs and discuss their potential as PeV neutrino sources in Section II. Then we focus on semi-relativistic hypernovae in star-forming galaxies as a possible source class that can simultaneously account for the newly discovered sub-PeV/PeV neutrinos and UHECRs in Section III. In Section IV, we conclude with a discussion of further aspects concerning the proposed scenario.

2.2 Possible Common Sources for PeV Neutrinos and UHECRs

Considering some usually discussed types of sources that are known to satisfy the Hillas criterion (Hillas 1984) for acceleration of UHECRs, we present in Fig. 2.1 the typical regions that they may occupy on the plane of $\dot{W}_{p,0}$, the local proton energy production rate, versus f_{π} , the pion-production efficiency of CRs that produce PeV neutrinos. The black solid line represents the relation between $\dot{W}_{p,0}$ and f_{π} required to reproduce the observed neutrino flux, with the gray band corresponding to its 1- σ confidence interval. The upper and lower dashed curves represent the local energy production rate $\dot{W}_{\text{CR},0}$ of escaping CRs required to account for the observed UHECRs if the Galactic-extragalactic transition occurs at the second knee and at the ankle, respectively, for the case $\xi = 1$. The dotted curves are corresponding ones for the case $\xi = 0$. Different values of ξ will result in different sets of the two curves. Valid sources of UHECRs are expected to be located above the lower curves. If, in addition, the efficiency of escape of accelerated CRs from the source is high, they should lie below the upper curves. Note that $\alpha = 10$ has been adopted here. A larger α will shift all the curves upward by the same factor.

If the observed sub-PeV/PeV neutrinos originate from the sources of UHECRs, the relevant region in the figure should overlap with the gray band. This implies that for Galactic-extragalactic transition at the second knee, the pion production efficiency for escaping CRs must be ~ 0.1 , whereas if the transition is at the ankle, the efficiency must be even higher, i.e., $\gtrsim 0.5$.

In plotting the various regions in Fig. 2.1, we have assumed only representative values for each type of source, without indicating the entire parameter space covered by that source class. For all sources, we take a common range of values $\eta_p = 0.01 - 1$ for the fraction of available energy that is channeled into escaping CR protons.

Jets of active galactic nuclei (AGN) have long been considered one of the most promising candidates for the sources of UHECRs as well as neutrinos (Biermann & Strittmatter 1987; Mannheim & Biermann 1992; Mannheim 1993; Rachen & Biermann 1993). Here we consider only powerful objects with kinetic power $\sim 10^{45} \text{erg s}^{-1}$ and source density $\sim 10^{-5} \text{Mpc}^{-3}$ (Berezinsky et al. 2006; Ghisellini et al. 2010), which gives $\dot{W}_{0, \text{AGN}} \sim \eta_p 10^{47.5} \text{erg Mpc}^{-3} \text{yr}^{-1}$. The pion production efficiency depends on the location of CR acceleration and neutrino production. In the inner jet regions corresponding to the typical emission zones in blazars within $\sim 10 - 100$ Schwarzschild radii of the central black hole, the large photon density implies a high value, $0.1 \lesssim f_\pi \leq 1$ (Mannheim & Biermann 1992; Mannheim 1993; Mannheim et al. 2001) (note also Stecker et al. 1991). In the outer jet regions such as the hot spots or radio lobes at kpc-Mpc scales with much less ambient radiation, accordingly lower values are expected, $f_\pi \sim 10^{-3} - 10^{-2}$ (Biermann & Strittmatter 1987; Anchordoqui et al. 2008). These sites are respectively denoted “AGN inner jets/cores” and “AGN outer jets” in Fig. 2.1.

Gamma-ray bursts (GRBs) have also been widely discussed as favorable sources of UHECRs (Milgrom & Usov 1995; Vietri 1995; Waxman 1995). Adopting an isotropic-equivalent kinetic energy per GRB of 10^{54}erg and a local GRB rate $\sim 1 \text{Gpc}^{-3} \text{yr}^{-1}$ (Wanderman & Piran 2010), we have $\dot{W}_{0, \text{GRB}} \sim \eta_p 10^{45} \text{erg Mpc}^{-3} \text{yr}^{-1}$. If CR acceleration occurs in the innermost regions of internal shocks with high photon density, the pion production efficiency could be as high as $0.1 \lesssim f_\pi \leq 1$ (Waxman & Bahcall 1997), as indicated in Fig. 2.1 as “GRB internal shocks”. Note, however, that the location of internal shocks can span a large range of radii depending on the behavior of the central engine, and if it occurs in the outermost regions closer to the external shock, much smaller values of f_π are also possible.

Clusters of galaxies, in particular the accretion shocks surrounding them,

have also been proposed as possible UHECR sources (Norman et al. 1995; Kang et al. 1996; Kang et al. 1997). Although it may be challenging to achieve maximum energies of $\sim 10^{20}$ eV, acceleration up to \gtrsim EeV may be quite feasible (Inoue et al. 2005; Vannoni et al. 2011). Furthermore, radio galaxies, i.e. AGN with jets, are sometimes found in the central regions of clusters, which can also provide UHECRs inside clusters. Such UHECRs can produce high-energy neutrinos via pp collisions with the gas constituting the intracluster medium (ICM) (Murase et al. 2008). If we consider massive clusters with $M \sim 10^{15} M_{\odot}$, their space density is $\sim 10^{-6} \text{ Mpc}^{-3}$ and their expected accretion luminosity is $\sim 10^{46} \text{ erg s}^{-1}$, so we arrive at $\dot{W}_{0,\text{IGS}} \sim \eta_p 10^{47.5} \text{ erg Mpc}^{-3} \text{ yr}^{-1}$, comparable to that of AGN. Assuming an average density of 10^{-4} cm^{-3} for the ICM gas and a residence time 1-10 Gyr of high-energy protons inside the cluster, we estimate a pion-production efficiency of $\sim 0.01 - 0.1$, outlined in Fig. 2.1 as “Clusters of galaxies”.

Supernova remnants (SNRs) have been widely discussed as promising accelerators of CR protons (see Hillas 2005 for a review and references therein). However, standard treatments of shock acceleration in SNRs with ejecta velocities $< 10^9 \text{ cm s}^{-1}$ reveal that it is difficult to reach maximum energy $\gtrsim 40 \left(\frac{1+z}{2}\right)$ PeV, not to mention UHE protons with energy \geq EeV (Lagage & Cesarsky 1983 Schure & Bell 2013) (but see Ptuskin et al. 2010 for discussions on acceleration during the very early stage of SNRs, and Biermann & Strittmatter 1988 on SNRs expanding into their progenitor winds). However, a subset of very energetic supernovae called semi-relativistic hypernova (SR-hypernova), has ejecta with much faster velocities, $\gtrsim 0.1c$, expanding into their progenitors’ stellar winds (Kulkarni et al. 1998). Assuming a CR-amplified magnetic field with a strength close to equipartition, SR-hypernovae satisfy the Hillas condition (Hillas 1984) for acceleration of $\gtrsim 10^{18}$ eV protons and have thus been proposed as sources of UHECRs above the second knee (Wang et al. 2007), or even up to the highest CR energies when considering the fastest part of the ejecta and heavy nuclei acceleration (Liu & Wang 2012). SR-hypernovae are usually found associated with low-luminosity GRBs. Although their event rate of $\sim 500 \text{ Gpc}^{-3} \text{ yr}^{-1}$ is lower than ordinary supernovae, the total kinetic energies released per event is larger, $\sim (3 - 5) \times 10^{52} \text{ erg}$ (Kulkarni et al. 1998), providing a proton production rate $\dot{W}_{0,\text{HN}} \sim \eta_p 10^{46} \text{ erg Mpc}^{-3} \text{ yr}^{-1}$.

Fig. 2.2 and Fig. 2.3 show the propagated spectrum of UHECRs from SR-hypernova throughout the whole universe, with two different possible chemical compositions of injected particles. Fig. 2.2 considers the chemical composition of UHECRs at the source equal to that of the Wolf-Rayet stellar wind, where

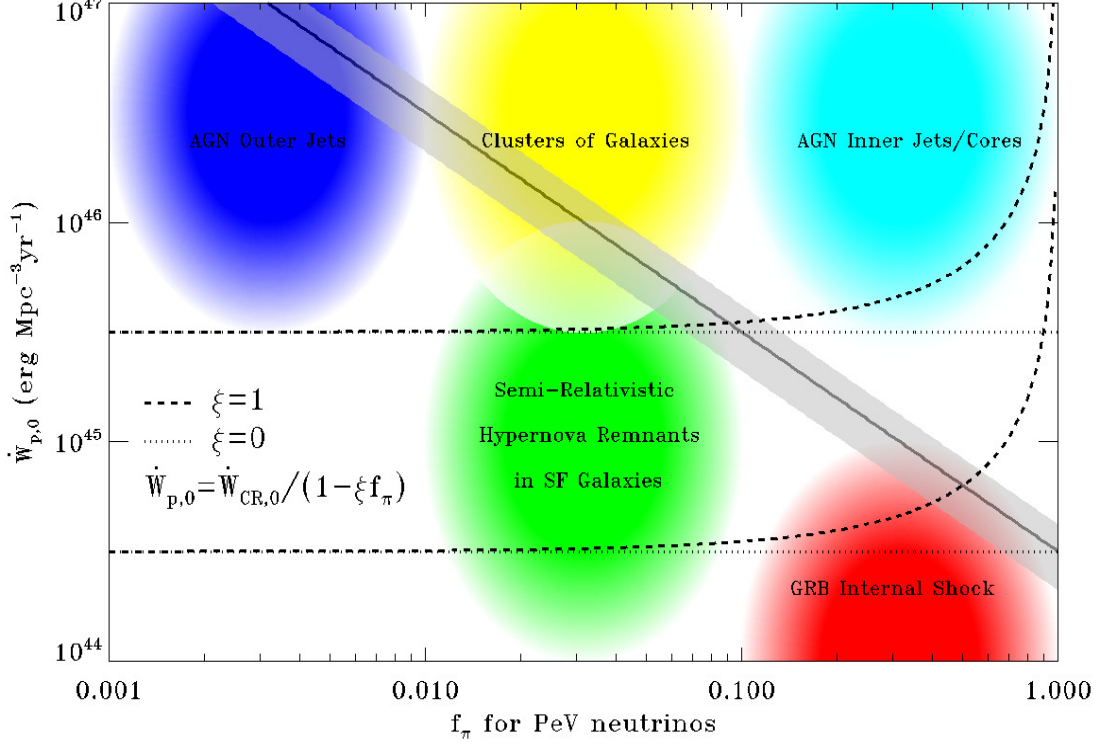


Figure 2.1: The local proton energy production rate $\dot{W}_{p,0}$ versus f_π , the pion-production efficiency of escaping CRs that produce PeV neutrinos. The black solid line represents the relation between $\dot{W}_{p,0}$ and f_π required to reproduce the observed neutrino flux, with the gray band corresponding to its 1- σ confidence interval. The upper and lower dashed curves represent the local energy production rate $\dot{W}_{CR,0}$ of escaping CRs required to account for the observed UHECRs if the Galactic-extragalactic transition occurs at the second knee and at the ankle, respectively, for the case $\xi = 1$. The dotted curves are corresponding ones for the case $\xi = 0$. Here $\alpha = 10$ is assumed for the normalization factor of the proton spectrum (note $\alpha = \ln(E_{max}/E_{min})$ for $s_p = 2$). Larger/smaller values of alpha will shift all curves in the plot upwards/downwards by the same factor. See text for discussion on the regions corresponding to different potential UHECR source candidates.

matters are dominated by helium, carbon and oxygen elements, with mass ratio $M_{\text{He}} : M_{\text{C}} : M_{\text{O}} = 0.32 : 0.39 : 0.25$ (Bieging 1990). Fig. 2.3 presents the similar result but with a chemical composition of UHECRs at sources based on the best fit for the early spectra and light curve of SN 1998bw (Nakamura et al. 2001), which yields a mass ratio for different elements in the hypernova ejecta as $M_{\text{C}} : M_{\text{O}} : M_{\text{Ne}} : M_{\text{Mg}} : M_{\text{Si}} : M_{\text{S}} : M_{\text{Ca}} : M_{\text{Fe}} = 0.006 : 0.71 : 0.037 : 0.034 : 0.083 : 0.041 : 0.007 : 0.09$. In both figures, the spectrum of injection cosmic rays are assumed to be a power law with index -2 and the maximum energy of certain species is $E_{\text{max}} = 10^{20.5}(Z/26)\text{eV}$. We can see the fit is not good in the wind-element composition case. The reason is because the maximum energies of intermediate-mass nuclei such as C and O are below 10^{20}eV given the assumption of E_{max} shown above. It results in an exponentially cutoff in the spectrum before 10^{20}eV . The fitting (including the fitting in the ejecta-element composition case) can be improved if considering some modifications, as shown in Fig. 2.4. We present these figures just to show SR-hypernovae are potential candidates of UHECRs, especially when considering the measurement of chemical composition from the PAO. More discussions on this model can be found in Liu & Wang (2012).

Below we estimate that the pion production efficiency for PeV neutrinos due to pp -collisions between CRs escaping from SR-hypernova remnants and the ambient interstellar medium (ISM) of their host galaxies is ~ 0.1 , although this is subject to uncertainties concerning the magnetic field and density of the host ISM. Thus, SR-hypernova remnants could be good candidates for the sources of the neutrinos detected by IceCube, as marked in Fig. 2.1. Since Fig. 2.1 only describes a necessary condition for the link between IceCube neutrinos and UHECRs, in the following sections we investigate in more detail whether a self-consistent model can be constructed that ascribe the newly discovered sub-PeV/PeV neutrinos to SR-hypernovae remnants, provided that they are also responsible for UHECRs above the second knee. Since both Auger and HiRes indicate a rather light composition of UHECRs around the second knee (Pierre Auger Collaboration 2010b; Abbasi et al. 2005), we assume that the source composition of CRs below $\sim 1\text{EeV}$ is predominantly protons and do not consider the effect of heavier nuclei in this work.

We point out that the marked regions in Fig. 2.1 for each source contain large uncertainties. More precise values of $\dot{W}_{0,\text{CR}}$ and f_{π} depend on the details of the models. Nonetheless, we can arrive at a general conclusion about the plausibility of candidate sources. As shown, if a certain type of source can only account

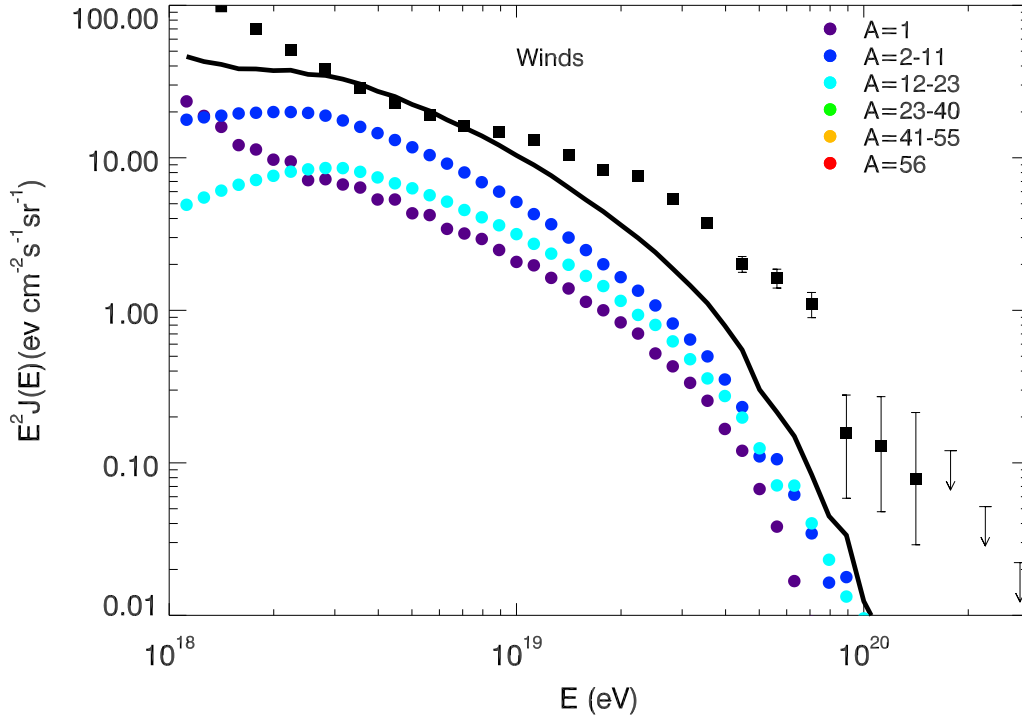


Figure 2.2: Propagated spectrum of cosmic rays assuming a source composition equal to that of the stellar wind of Wolf-Rayet stars. The black solid line represents the all-particle flux, while other lines represent the contributions by different species as shown in the legend. The black squares are data measured by PAO (Pierre Auger Collaboration 2011). The figure is taken from Liu & Wang (2012)

for UHECRs above the ankle, an extremely high pion-production efficiency (i.e. $f_\pi \approx 1$) is needed to achieve sufficient PeV neutrino flux. On the other hand, if the pion-production efficiency is too low (e.g., $\lesssim 0.01$), reproducing the observed neutrino flux requires a high proton production rate, which in turn implies a low efficiency of CR escape from the sources to be consistent with the observed UHECR flux. We also note that Fig. 2.1 only gives constraints on some candidates from the viewpoint of the energy budget. These sources do not necessarily represent the common origins of these neutrinos and UHECRs even if they satisfy these energetics constraints. Note also that some of these sources may already be constrained by other means. For instance, as indicated in (Liu & Wang 2013), if the GRB internal shock model is responsible for the PeV neutrinos, IceCube should probably have already discovered a neutrino-GRB

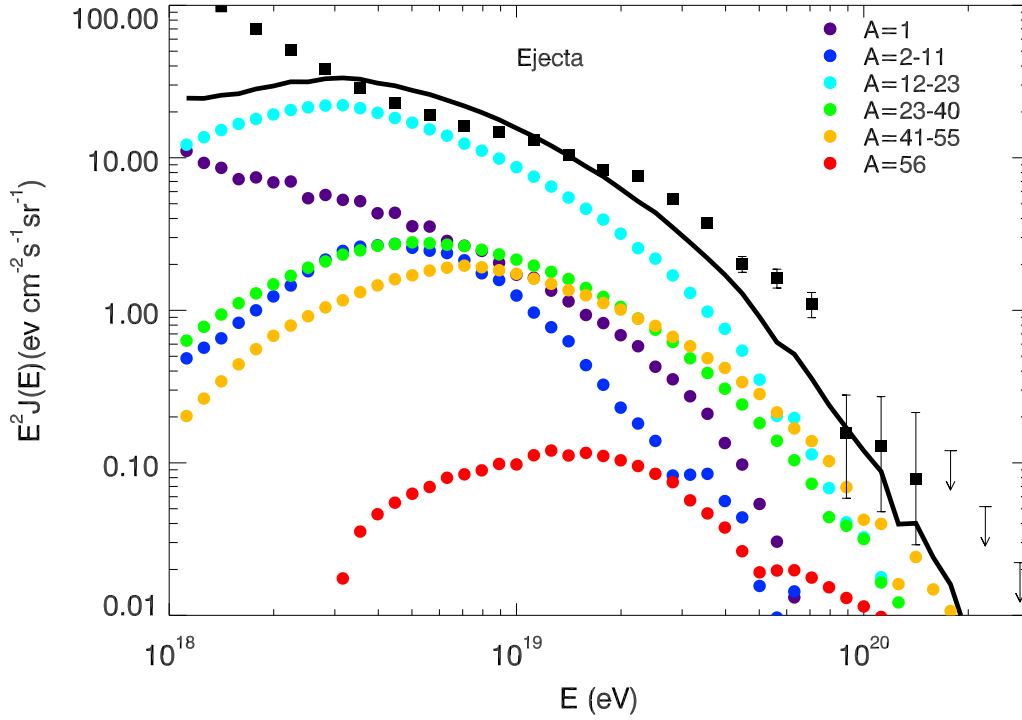


Figure 2.3: Propagated spectrum of cosmic rays assuming a source composition equal to that of the hypernova ejecta in the model of SN 1998bw. The figure is taken from Liu & Wang (2012)

association both in time and space during its previous 40- and 59-string search (IceCube Collaboration 2012). Gamma-ray upper limits for some nearby, massive galaxy clusters imply a low energy density of CRs at GeV-TeV energies in their ICM (Zandanel & Ando 2013; Fermi-LAT Collaboration et al. 2010b; Prokhorov & Churazov 2013), which constrain their contributions to the diffuse neutrino background at energies somewhat lower than those of the IceCube neutrinos. In simplest AGN models, $p\gamma$ collisions would lead to too many events at \gtrsim PeV energies, which is not favored by the current observation, unless extremely high magnetic field exists in the interaction region (Winter 2013).

In the SR-hypernova remnant model, the concomitantly produced isotropic gamma-ray flux may pose a potential problem. Generally speaking, if the diffuse neutrino flux is produced at the level of 10^{-8} $\text{GeVcm}^{-2}\text{s}^{-1}\text{sr}^{-1}$ via pp -collisions, the accompanying gamma-rays may overwhelm the 0.1-100 GeV diffuse isotropic gamma-ray background observed by Fermi/LAT (Fermi-LAT Collaboration 2010a)

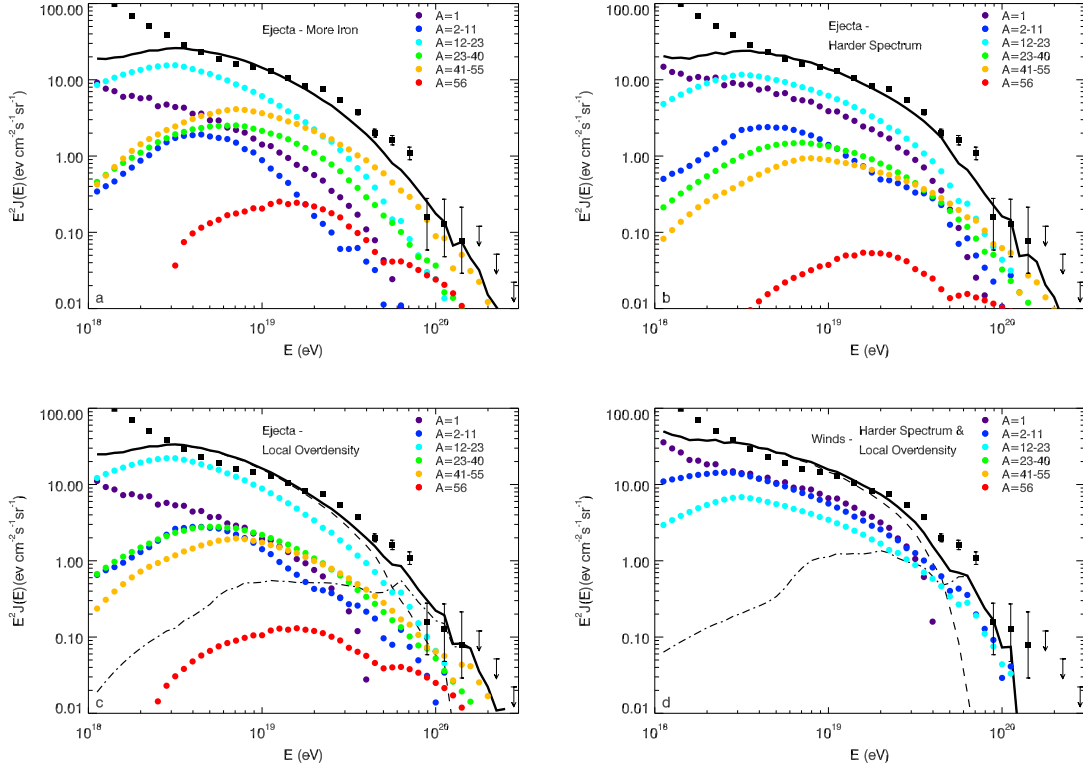


Figure 2.4: Panels (a)-(c) show the propagated cosmic-ray spectrum for the source composition equal to that of the hypernova ejecta, similar to Fig. 2.3, but with some modifications taken into account. In panel (a), the abundance of iron nuclei in the ejecta is increased by a factor of three. In panel (b), a hard initial spectrum with $p = 1.6$ is assumed. In panel (c), the local source number density is taken to be two times higher than the average within a distance of 30 Mpc. The dashed line in panel (c) represents the contribution by sources beyond 30 Mpc while the dash-dotted line represents the contribution by local sources within 30 Mpc. Panel (d) shows the propagated cosmic-ray spectrum for the source composition equal to that of stellar wind, but with the effects of a hard spectrum and a local overdensity being taken into account. The figure is taken from Liu & Wang (2012)

unless the source proton spectrum is sufficiently hard. As indicated in Murase et al. (2013), $s_p \gtrsim 2.2$ may already be in conflict with the gamma-ray background at low energies. Although a hard spectrum of $s_p = 2$ is employed in our calculation, we note that besides the proposed SR-hypernovae remnants, ordinary SNRs are expected to provide additional low-energy gamma-ray flux without contributing to sub-PeV/PeV neutrinos. Thus we must beware that the total diffuse gamma-ray flux generated by SR-hypernova remnants and SNRs do not exceed the observed value.

2.3 Neutrino Emission from Semi-relativistic Hypernova Remnants

Accelerated protons from SR-hypernova remnants will interact with the ISM before escaping from their host galaxies and produce neutrinos, gamma rays and electrons/positrons. The energy loss time of CR protons in the ISM via pp -collisions is

$$\begin{aligned} \tau_{pp}(\varepsilon_p) &= [\kappa \sigma_{pp}(\varepsilon_p) n c]^{-1} \\ &= 6 \times 10^7 \text{ yr} \left[\frac{\sigma_{pp}(\varepsilon_p = 60 \text{ PeV})}{100 \text{ mb}} \right]^{-1} \left(\frac{n}{1 \text{ cm}^{-3}} \right)^{-1} \end{aligned} \quad (2.2)$$

where $\kappa = 0.17$ is the inelasticity, σ_{pp} is the cross section, and n is the number density of ISM protons. The pp -collision efficiency can be estimated by $f_\pi = \min(1, t_{\text{esc}}/\tau_{pp})$ with t_{esc} as the escape timescale. Generally, there are two ways for CRs to escape from a galaxy. The first one, the diffusive escape, is energy-dependent and the other, and the second one, the advective escape via a galactic wind, is energy-independent. The associated escape timescales can be estimated by $t_{\text{diff}} = h^2/4D$ and $t_{\text{adv}} = h/V_w$ respectively. Here $D = D_0(E/E_0)^\delta$ is the diffusion coefficient where D_0 and E_0 are normalization factors, and δ may vary between 0 and 1 depending on the spectrum of interstellar magnetic turbulence. h is usually taken as the scale height of the galaxy's gaseous disk and V_w is the velocity of the galactic wind in which the CRs are advected. The diffuse gamma-ray emission from the Galactic plane implies $f_\pi \sim 1\%$ for TeV protons (Strong et al. 2010), so we may expect that f_π for 10PeV protons is $\ll 1\%$ in our Galaxy. However, since the SR-hypernova rate should generally trace the cosmic star formation rate (SFR), which is known to increase dramatically with z from $z = 0$ up to at least $z \sim 1-2$ (Hopkins & Beacom 2006), the properties of galaxies at $z \sim 1-2$ (hereafter

‘high-redshift’ galaxies) are likely to be more important for determining the total diffuse neutrino flux. As our template systems, we consider high-redshift galaxies of two types, normal star-forming galaxies (NSG) and starburst galaxies (SBG).

High-redshift galaxies display different properties from nearby ones. High-redshift NSGs generally do not reveal well-developed disk structure and show more extended morphologies with typical scale height $h \sim 1$ kpc for massive systems (Daddi et al. 2010, Law et al. 2012). They also have much higher mass fractions of molecular gas (Daddi et al. 2010) with typical column density $\Sigma \sim 0.1 \text{ g cm}^{-2}$, implying volumetric average ISM densities of $n \sim \Sigma/2h \sim 10 \text{ cm}^{-3}$. High-redshift SBGs typically have scale height $h \sim 500$ pc and average gas density $n \sim 250 \text{ cm}^{-3}$ (Tacconi et al. 2006). As for diffusion coefficients, recent studies on CR propagation and anisotropy in our Galaxy suggest $D_0 \sim 10^{28} \text{ cm}^2 \text{ s}^{-1}$ at 3 GeV and $\delta \simeq 0.3$ (Trotta et al. 2011). Since little is known about the diffusion coefficient in high- z galaxies, we adopt the same values of D_0 and δ as inferred in our Galaxy for high-redshift NSGs. We assume a lower diffusion coefficient $D_0 \sim 10^{27} \text{ cm}^2 \text{ s}^{-1}$ for high-redshift SBGs, because the magnetic fields in nearby SBGs such as M82 and NGC253 are observed to be ~ 100 times stronger than in our Galaxy and the diffusion coefficient is expected to scale with the CR’s Larmor radius ($\propto \varepsilon_p/B$) (Loeb & Waxman 2006). Regarding advective escape, the velocity of the Galactic nuclear wind is $\sim 300 \text{ km s}^{-1}$ (Keeney et al. 2006; Crocker 2012), while optical and X-ray observations show observations imply an outflow in M82 with velocity $\sim 500 - 600 \text{ km s}^{-1}$ (McKeith et al. 1995) and $1400 - 2200 \text{ km s}^{-1}$ (Strickland et al. 2009) respectively. Since galactic winds are probably driven by supernova explosions (Chevalier & Clegg 1985; Breitschwerdt et al. 1993; Ptuskin et al. 1997) whose rate is higher in high-redshift galaxies, we may expect their winds to be faster and take $V_w = 500 \text{ km s}^{-1}$ and 1500 km s^{-1} as the reference values for NSGs and SBGs respectively. Then we obtain

$$t_{\text{diff}}^{\text{N}} = 5 \times 10^4 \text{ yr} \left(\frac{h}{1 \text{ kpc}} \right)^2 \left(\frac{D_0}{10^{28} \text{ cm}^2 \text{ s}^{-1}} \right)^{-1} \left(\frac{\varepsilon_p}{60 \text{ PeV}} \right)^{-0.3} \quad (2.3)$$

$$t_{\text{adv}}^{\text{N}} = 2 \times 10^6 \text{ yr} \left(\frac{h}{1 \text{ kpc}} \right) \left(\frac{V_w}{500 \text{ km s}^{-1}} \right)^{-1} \quad (2.4)$$

for NSGs, and

$$t_{\text{diff}}^{\text{B}} = 10^5 \text{ yr} \left(\frac{h}{0.5 \text{ kpc}} \right)^2 \left(\frac{D_0}{10^{27} \text{ cm}^2 \text{ s}^{-1}} \right)^{-1} \left(\frac{\varepsilon_p}{60 \text{ PeV}} \right)^{-0.3} \quad (2.5)$$

$$t_{\text{adv}}^{\text{B}} = 3 \times 10^5 \text{ yr} \left(\frac{h}{0.5 \text{ kpc}} \right) \left(\frac{V_w}{1500 \text{ km s}^{-1}} \right)^{-1} \quad (2.6)$$

for SBGs. The escape timescale can be approximated by $t_{\text{esc}} = \min(t_{\text{adv}}, t_{\text{diff}})$, and we may expect a break occurring in t_{esc} when $t_{\text{adv}} = t_{\text{diff}}$, i.e.,

$$\varepsilon_{p,b}^{\text{N}} = 300 \text{ GeV} \left(\frac{h}{1 \text{ kpc}}\right)^{3.3} \left(\frac{V_w}{500 \text{ km s}^{-1}}\right)^{3.3} \left(\frac{D_0}{10^{28} \text{ cm}^2 \text{ s}^{-1}}\right)^{-3.3} \quad (2.7)$$

and

$$\varepsilon_{p,b}^{\text{B}} = 1.6 \text{ PeV} \left(\frac{h}{1 \text{ kpc}}\right)^{3.3} \left(\frac{V_w}{1500 \text{ km s}^{-1}}\right)^{3.3} \left(\frac{D_0}{10^{27} \text{ cm}^2 \text{ s}^{-1}}\right)^{-3.3} \quad (2.8)$$

for NSGs and SBGs respectively. We then find that the pp -collision efficiencies for production of 1 PeV neutrinos in NSGs and SBGs are respectively

$$f_{\pi}^{\text{N}} = t_{\text{diff}}^{\text{N}}/\tau_{pp}^{\text{N}} \simeq 0.01 \text{ and } f_{\pi}^{\text{B}} = t_{\text{diff}}^{\text{B}}/\tau_{pp}^{\text{B}} \simeq 0.4 \quad (2.9)$$

The single-flavor neutrino flux at 1 PeV is then $\varepsilon_{\nu}^2 \Phi_{\nu} = \frac{1}{6} [f_{\text{SB}} f_{\pi}^{\text{B}} + (1 - f_{\text{SB}}) f_{\pi}^{\text{N}}] \varepsilon_p^2 \Phi_{\text{CR}} \sim 10^{-8} \text{ GeV cm}^{-2} \text{ s}^{-1} \text{ sr}^{-1}$, which is comparable to the observed neutrino flux. Here $f_{\text{SB}} \sim 10\% - 20\%$ (Rodighiero et al. 2011; Lamastra et al. 2013) is the fraction of the SFR contributed by SBGs. If we assume that SR-hypernovae account for CRs above $\sim 5 \times 10^{17} \text{ eV}$, they should provide a CR flux of $\varepsilon_p^2 \Phi_{\text{CR}} \simeq 7 \times 10^{-7} \text{ GeV cm}^{-2} \text{ s}^{-1} \text{ sr}^{-1}$ at this energy (Abbasi et al. 2004) and the required local CR energy production rate \dot{W}_0 is then $\sim 10^{45.5} \text{ erg Mpc}^{-3} \text{ yr}^{-1}$. Assuming that each SR-hypernova releases $E_{k,\text{HN}} = 5 \times 10^{52} \text{ erg}$ of kinetic energy (Kulkarni et al. 1998), a fraction $\eta_p = 10\%$ of which goes into CRs, we find the required local event rate is about $600 \text{ Gpc}^{-3} \text{ yr}^{-1}$, consistent with the observed value (Guetta & Della Valle 2007).

The fluxes of secondary neutrinos and gamma rays produced by one SR-hypernova ϕ_{ν} and ϕ_{γ} (in unit of eV^{-1}) are calculated with the following analytical approximation (Kelner et al. 2006),

$$\phi_i(\varepsilon_i) \equiv \frac{dN_i}{d\varepsilon_i} \simeq \int_{\varepsilon_i}^{\infty} \frac{f_{\pi}}{\kappa} J_p(\varepsilon_p) F_i\left(\frac{\varepsilon_i}{\varepsilon_p}, \varepsilon_p\right) \frac{d\varepsilon_p}{\varepsilon_p} \quad (2.10)$$

where i could be γ or ν . In the above equation, F_i is the spectrum of the secondary γ or ν in a single collision. We assume that the accelerated proton spectrum is $J_p = C_p \varepsilon_p^{-2} \exp(-\varepsilon_p/\varepsilon_{p,\text{max}})$ where C_p is a normalization coefficient fixed by $\int \varepsilon_p J_p d\varepsilon_p = \eta_p E_{k,\text{HN}}$. Here we neglect the contribution of secondary electrons/positrons and primary electrons via inverse Compton scattering and Bremsstrahlung radiation, because these are only important at $\lesssim 100 \text{ MeV}$ (Lacki et al. 2012). To calculate the diffuse flux of neutrinos and gamma rays, we need to integrate the contribution from galaxies throughout the whole universe, i.e.

$$\Phi_i(\varepsilon_i^{\text{ob}}) \equiv \frac{dN_i^{\text{ob}}}{d\varepsilon_i^{\text{ob}}} = \frac{1}{4\pi} \int_0^{z_{\text{max}}} \rho(z) \Gamma_{\text{HN}}^{\text{SFR}} \phi_i[(1+z)\varepsilon_i^{\text{ob}}] \frac{cdz}{H(z)} \quad (2.11)$$

where $\rho(z) = \rho_0 S(z)$ represents the star-formation history with ρ_0 being the local SFR and $S(z)$ describing its evolution with redshift. The total SFR in the local universe is found to be $\rho_0 \sim 0.01 M_\odot \text{ yr}^{-1} \text{ Mpc}^{-3}$ and assumed to evolve as (Hopkins & Beacom 2006) $S(z) \propto (1+z)^{3.4}$ for $z < 1$, $(1+z)^0$ for $1 \leq z \leq 4$ and $(1+z)^{-7}$ for $z > 4$. Here we assume the fraction of SFR from SBGs is $f_{SB} = 20\%$ at any cosmic epoch. The factor $\Gamma_{\text{HN}}^{\text{SFR}}$ represents the ratio between the SR-hypernova rate and SFR (in units of M_\odot^{-1}). Its value is normalized by requiring the local CR energy production rate of SR-hypernovae to match the observed CR flux above the second knee. $H(z) = H_0 \sqrt{\Omega_M(1+z)^3 + \Omega_\Lambda}$ is the Hubble parameter and we adopt $H_0 = 71 \text{ kms}^{-1} \text{ Mpc}^{-1}$, $\Omega_M = 0.27$ and $\Omega_\Lambda = 0.73$. While neutrinos can reach the Earth without interaction, very high energy (VHE, $\gtrsim 100 \text{ GeV}$) gamma rays can be absorbed by e^\pm pair production on the intergalactic radiation field, initiating cascade processes and depositing energy into $< 100 \text{ GeV}$ photons. As long as the cascade is well developed, the VHE gamma rays injected at an epoch of redshift z will form a nearly universal spectrum which only depends on the total energy injected and the injection redshift z (Coppi & Aharonian 1997; Berezhinsky et al. 2011; Murase et al. 2012) We integrate over redshift to sum up the contributions of cascades initiated at different z .

Panel (a) of Fig. 2.5 presents our calculated diffuse neutrino and gamma-ray fluxes. The red dashed and dash-dotted lines represent the neutrino flux from NSGs and SBGs respectively. At low energies, energy-independent advective escape dominates over energy-dependent diffusive escape, so the spectrum of neutrinos roughly follows the $s = -2$ accelerated proton spectrum. As the energy increases, the neutrino spectrum breaks because diffusive escape becomes faster than advective escape. Because $t_{\text{diff}} \propto \varepsilon^{-0.3}$, the spectral index above the break increases by about 0.3. But the increase of the pp cross section at higher energies (Kelner et al. 2006) compensates this slightly, making the final spectral slope close to -2.2. Note that in this case the UHECRs are mostly produced by SR-hypernovae in NSGs while the PeV neutrinos mainly arise from SR-hypernovae in SBGs. This is because most SR-hypernovae occur in NSGs while the pp -collision efficiency is much higher in SBGs.

Given the uncertainties in D at high redshift, we also consider an alternative case in which D_0 in high-redshift NSGs is 10 times smaller than in our Galaxy. There is observational evidence for stronger magnetic fields in such galaxies (Bernet et al. 2013), so a smaller diffusion coefficient is plausible. With $D_0 = 10^{27} \text{ cm}^2 \text{ s}^{-1}$ and assuming $f_{SB} = 10\%$, we find that $f_\pi^N \simeq 0.1$ for production of

PeV neutrinos, in which case both PeV neutrinos and UHECRs are produced predominantly by hypernovae in NSGs, as shown in panel (b) of Fig. 2.5.

If the observed sub-PeV/PeV neutrinos originate from the sources of UHECRs, their spectrum should extend to $\gtrsim 10$ PeV without an abrupt cutoff. In our model, the spectrum becomes softer at $\lesssim 10$ PeV, since the energy of the corresponding parent proton is $\lesssim 0.6(\frac{1+z}{2})$ EeV, approaching our assumed maximum energy of 1 EeV. This softening would not occur if $E_{p,\max}$ can be higher. Unless the propagation mode of CRs changes from diffusive to rectilinear above \sim EeV and leads to a lower pion-production efficiency, our model predicts a flux of a few times 10^{-9} GeV cm $^{-2}$ s $^{-1}$ sr $^{-1}$ around 10 PeV, as long as we assume the observed neutrinos and CRs above the second knee share a common origin. This flux is consistent with the present non-detection of neutrinos above several PeV, but is likely to be detectable in the future. Given that the all-flavor exposure of IceCube is $\sim 10^{15}$ cm 2 sr s at 10 PeV (Anchordoqui et al. 2013) for 662 days, we may expect that such a flux of $\gtrsim 10$ PeV neutrinos would be detected in $\lesssim 5 - 10$ yrs operation.

2.4 Discussion

Together with the cascade component, the total diffuse gamma ray flux at < 100 GeV is $\sim (7 - 8) \times 10^{-8}$ GeV cm $^{-2}$ s $^{-1}$ sr $^{-1}$ in both cases, as shown with the solid blue lines in Fig. 2. Note that putative additional losses due to absorption of VHE photons by the radiation fields inside their host galaxies (Inoue 2011) and by synchrotron losses of the e^\pm pairs in the host galaxy magnetic fields would lower the predicted cascade flux. A detailed study shows (Chang & Wang 2014) that about associating gamma-ray flux contribute about 20% of the observed flux at 100 GeV. The resulting flux is $\lesssim 50\%$ of the flux observed by LAT. Also note that although normal SNRs should not contribute to the $\gtrsim 100$ TeV neutrino flux, they can accelerate protons to PeV and produce < 100 TeV gamma rays, contributing to the diffuse gamma-ray background. Compared to normal supernovae, the local event rate of SR-hypernovae is $\sim 1\%$ while their explosion energy is dozens of times larger, so the integral energy production rate of supernovae may be a few times larger than that of SR-hypernovae. But the rate of SR-hypernovae relative to supernovae might be higher at high redshifts, as SR-hypernovae may be engine-driven like long GRBs (Paczynski 1998), which seem to occur preferentially in low-metallicity galaxies (Stanek et al. 2006). This would suggest a relatively smaller contribution of normal SNRs at higher z . Nevertheless, as a rough estimate, we

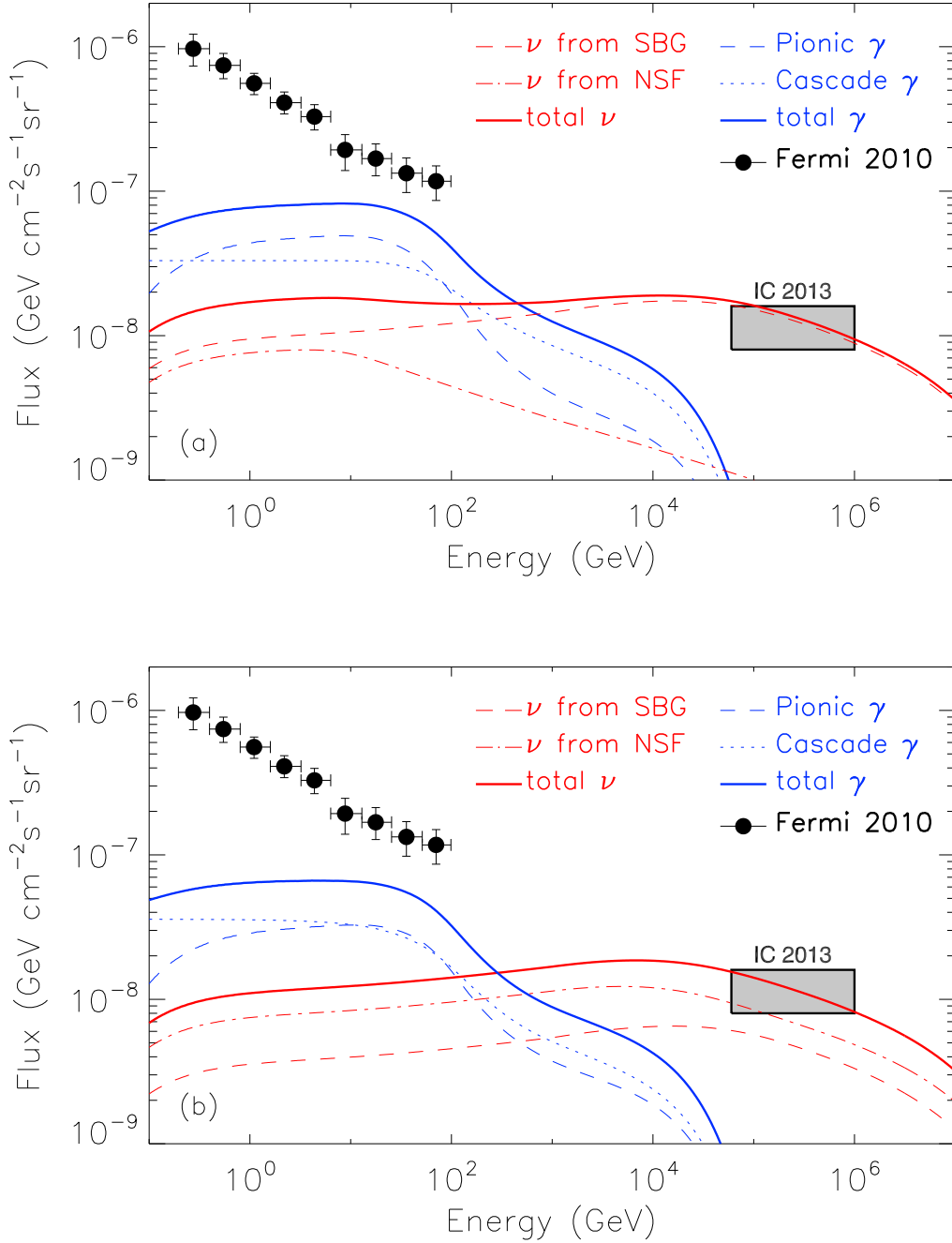


Figure 2.5: Spectra of ν_μ and gamma rays produced by SR-hypernova remnants in star-forming galaxies. Upper panel: the red dashed line and dash-dotted line represent the one-flavor neutrino flux from starburst galaxies and normal star-forming galaxies respectively, and the red solid line is their sum. Neutrino oscillations imply that $\nu_\mu : \nu_e : \nu_\tau = 1 : 1 : 1$ at the detector. The blue dashed and dotted lines represent the gamma ray fluxes from pion decay (accounting for intergalactic absorption) and the cascaded gamma ray flux, respectively, while the blue solid line is the sum of the two components. Data points are taken from (Abdo et al. 2010). The shaded rectangle shows the IceCube flux (IceCube Collaboration 2013b). Lower panel: same as the upper one but with $D_0 = 10^{27} \text{ cm}^2 \text{ s}^{-1}$ used for normal star-forming galaxies and $f_{SB} = 10\%$. See text for more discussion.

may expect that normal SNRs could produce a gamma-ray flux comparable to (or even less than) that of SR-hypernova remnants, and in the former case the total gamma-ray flux at 10 – 100 GeV could reach the level of the observed one, providing a possible explanation for the apparent hardening in the spectrum of the diffusive isotropic gamma-ray background at > 10 GeV. On the other hand, we should also bear in mind that if the normal SNRs' energy budget turns out to be higher than that of SR-hypernovae even at high redshifts, the total generated diffusive gamma-ray flux would be a serious problem for this model.

As mentioned above, the spectral index of the high energy neutrino flux depends on the spectral indices of the injected protons and that of interstellar magnetic turbulence, i.e., $s_\nu \simeq s_p + \delta - 0.1$ where the correction -0.1 results from the increase of the pp cross section at high energy. Since the current measurement of the neutrino spectrum is rather approximate and contains significant uncertainties, if further observations would show a different spectral shape, the values of s_p or δ must be adjusted correspondingly. The most restrictive constraint on these two parameters comes from the concomitantly produced < 100 GeV gamma-ray flux in the pion-production process: this should not exceed the isotropic gamma-ray background observed by Fermi/LAT. Adopting either a larger s_p or a larger δ would lead to a higher low-energy gamma-ray flux (see the Appendix for a detailed calculation). If future observations reveal a much softer neutrino spectrum, our model faces difficulties without invoking some untypical parameters or further refinements, e.g., introducing a break in the source spectrum.

If SR-hypernovae are responsible not only for CRs above the second knee but also for those at the highest energies, one may ask whether any of the neutrino events that have already been observed by IceCube can be associated with individual sources within the GZK horizon of 100 Mpc (Greisen 1966; Zatsepin & Kuz'min 1966; Taylor et al. 2011). According to our adopted evolution function $S(z)$ and assuming an isotropic sky distribution for such sources, only about 0.4 out of the total of 37 events can be expected to come from within 100 Mpc. In case such nearby sources happened to coincide with the direction of maximum effective area for IceCube, then they may be responsible for about one of the 37 events.

The local SFR density is estimated to be $\sim 0.01 M_\odot \text{Mpc}^{-3} \text{yr}^{-1}$, and thus employing the relation between SFR and infrared luminosity of a galaxy $\text{SFR} [M_\odot \text{yr}^{-1}] = 1.7 \times 10^{-10} L_{\text{IR}} [L_\odot]$ (Magnelli et al. 2011), we find that a galaxy's CR luminosity, ac-

commodated by hypernovae, is $L_{\text{CR}} \sim 10^{40} \text{ erg s}^{-1} (\dot{W}_0/10^{45.5} \text{ erg Mpc}^{-3} \text{ yr}^{-1})(L_{\text{IR}}/10^{10} L_{\odot})$. Given the infrared luminosity of our Galaxy is $\sim 10^{10} L_{\odot}$ and assuming a pp -collision efficiency of 10^{-3} , we estimate the total Galactic neutrino luminosity at 100 TeV–1 PeV is $\lesssim 10^{36} \text{ erg s}^{-1}$. Note that our Galaxy might be too metal rich to host semi-relativistic hypernovae (or long GRBs) for the last several billion years (Stanek et al. 2006), so the real value could be smaller. Even if all these neutrinos are produced in the Galactic center and radiate isotropically, it would result in $\lesssim 1$ event detection during 662 days operation within a 8° circular region around the Galactic Center (Razzaque 2013) and would not cause a strong anisotropy that violates the observations (IceCube Collaboration 2013).

In this work, we assume all the starburst galaxies, as well as normal star-forming galaxies, have the same set of properties like magnetic field, gas density and etc, which are set to typical values of starburst galaxies and normal star-forming galaxies respectively. This lead to the same emissivity of neutrinos among all starburst galaxies or star-forming galaxies. However, these parameters should be different in different galaxies. For example, a galaxy with higher infrared luminosity should have larger SFR, and given the Kennicutt-Schmidt law (Kennicutt 1998) we can expect a denser gas in the galaxy. On the other hand, the number of galaxies of different luminosities also follow certain distribution, which is known as the luminosity function. Usually, there are less galaxies with higher luminosities. Recently, we consider a scenario with more realistic galaxy properties and luminosity function of starburst/star-forming galaxies, and got a similar conclusion (Chang et al. 2014, see Fig. 2.6), supporting the results obtained here.

To summarize, we studied whether the newly-detected sub-PeV/PeV neutrinos can originate from the same sources as those responsible for CRs with energies above the second knee. We discussed the conditions necessary for such a link between the observed PeV neutrinos and EeV CRs, and took SR-hypernova remnants in star-forming galaxies as an example of a self-consistent model that can provide the neutrino-UHECR link. Comparing the predictions of different models, the generated neutrino spectrum may vary somewhat from model to model, and even within the same model depending on the uncertain parameters. Thus, based on the spectral information alone, SR-hypernova remnants can be neither confirmed nor refuted as the true sources of the observed neutrinos. However, as long as the link between the observed neutrinos and EeV CRs exists, we may generally expect detection of $\gtrsim 10$ PeV neutrinos in the near future. If

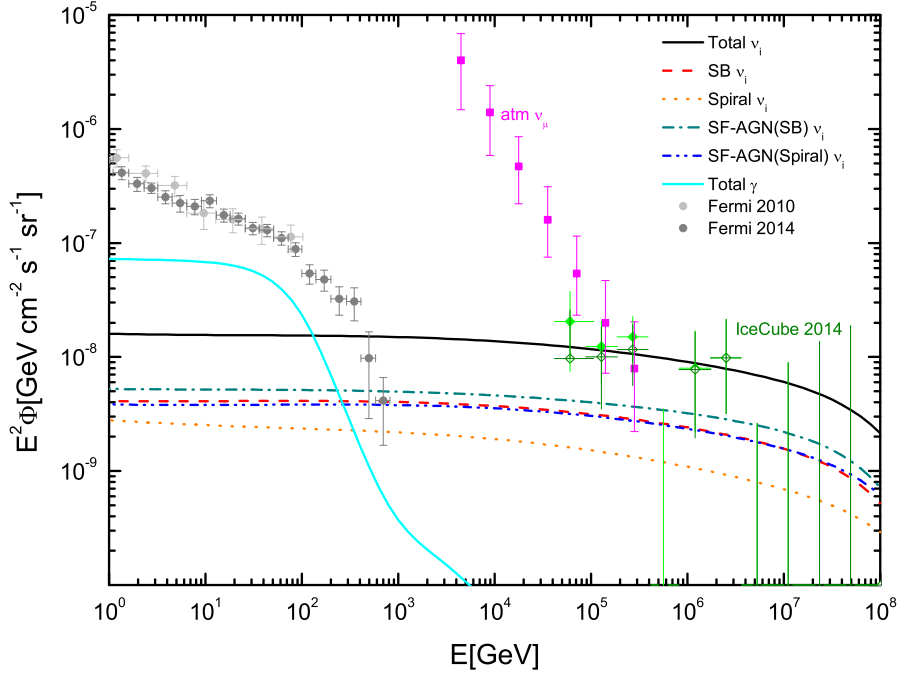


Figure 2.6: Diffusive neutrino flux from star-forming of different populations. The red, orange, green, blue lines show the flux contributed by starburst galaxies, normal spiral galaxies, SF-AGNs (SB) and SF-AGNs (spiral), respectively. And the black line represents the sum. The cyan line shows the associated produced diffuse gamma-ray flux. The figure is taken from Chang et al. (2014)

such a link could be recognized, the detected neutrino flux and spectral shape should proffer information on the pion-production process at the sources. We shall then know that the real sources, whatever their identity, have a similar pion-production efficiency as that claimed for SR-hypernova remnants here, given that they also explain the UHECRs above the second knee. This provides us a chance to study the environment of the sources. Future observations with greater statistics over the current neutrino energy range or detection at higher energies can give further constraints and help to uncover the true identity of the currently mysterious sources of EeV CRs.

Constraints on the Sources of Ultra-high Energy Cosmic Rays Using Anisotropy vs Chemical Composition

As we mentioned in the first chapter, despite of the long-lasting debate on transition of cosmic rays from Galactic to extragalactic origin, it is commonly believed that the sources of the highest energy cosmic rays (with energy above several tens of EeV) are from powerful extragalactic astrophysical objects. Due to the GZK effect (Greisen 1966; Zatsepin & Kuz'min 1966) and as well as the photodisintegration if UHECRs are nuclei (Puget et al. 1976), the sources of these cosmic rays should be in nearby universe within ~ 100 Mpc, where, however, there are still lots of candidates. In this chapter, we will show an additional constraint on UHECR sources by jointly using the anisotropy and chemical composition measurement of the PAO. This constraint is quite rigorous and leaves only a limited number of possible sources. This chapter is based on the work of (Liu et al. 2013).

3.1 A Joint Analysis on Anisotropy and Chemical Composition Measurement of UHECRs

On their way to Earth, UHECRs suffer inevitable interactions with the CMB and EBL that permeate extragalactic space, in particular Bethe–Heitler pair production, photo-pion production and photodisintegration. Photo-hadronic interactions inevitably introduce a high energy cut-off in the UHECR spectrum beyond $\sim 5 \times 10^{19}$ eV, due to the rapid decrease of the attenuation length of UHECRs with increasing energy. Above these GZK energies, the typical horizon to which

sources can be detected shrinks to values of the order of $\sim 100 - 200$ Mpc. This cut-off/suppression feature has now been observed by different experiments at a statistically significant level (Abbasi et al. 2008; The Pierre Auger Collaboration 2008; The Pierre Auger Collaboration 2010b), implying notably that the sources of the highest energy cosmic rays must be nearby luminous objects (Waxman 1995; Waxman 2005; Farrar & Piran 2009, Piran 2010, Taylor et al. 2011).

The Pierre Auger Observatory (PAO), presently the largest UHECR observatory, has reported the detection 69 events within the energy range 55–142 EeV between January 2004 and December 2009 (The Pierre Auger Collaboration 2010c). A detailed analysis has shown that the fraction of these events correlating with nearby AGN (< 75 Mpc) in the Véron-Cetty and Véron (VCV) catalog is $(38_{-6}^{+7})\%$, above the isotropic expectation of 21%. Most of this excess is found around the direction of Centaurus A (Cen A) within a surrounding 18° window, in which 13 events in the energy range 55–84 EeV are observed while only 3.2 are expected (The Pierre Auger Collaboration 2010a). Although the significances are lowered down with a larger data set as reported later, these anisotropy signals are still far from trivial. However, both the intergalactic and the Galactic magnetic field deflect the trajectories of cosmic rays, resulting in apparent correlations with objects which are not necessarily their true birth places. Furthermore, measurements on the maximum air shower elongations $\langle X_{\max} \rangle$ and their rms ($\sigma_{X_{\max}}$) by the PAO suggest that the chemical composition of UHECRs are progressively dominated by heavier nuclei at energies above 4 EeV (The Pierre Auger Collaboration 2010b). If the cosmic rays are indeed intermediate-mass or heavy nuclei, the deviation of their arrival directions due to propagation in the intervening magnetic fields must be significant, hence the observation of anisotropies appears slightly surprising. From a theoretical point of view, it may appear more favorable to accelerate heavy nuclei, as their higher charge, comparatively to protons, reduce the energetic constraints placed on the source candidates, e.g. Lemoine & Waxman (2009). However, it also requires the acceleration site to be abundant in intermediate-mass or heavy elements, well beyond a typical galactic composition (The Pierre Auger Collaboration 2011; Liu et al. 2012). Finally, other experiments, such as HiRes or the Telescope Array, find that the composition at $\gtrsim 10^{19}$ eV remains dominated by light nuclei (Abbasi et al. 2010, Tsunesada 2011).

One way to make progress is to use the pattern of anisotropies as a function of energy. This idea was first proposed in Lemoine & Waxman (2009): if a source produces an anisotropy signal at energy E with cosmic ray nuclei of charge Z , it

should also produce a similar anisotropy pattern at energies E/Z via the proton component that is emitted along with the nuclei, given that the trajectory of cosmic rays within a magnetic field is only rigidity-dependent. It is easy to show that the low energy anisotropy should appear stronger, possibly much stronger than the high energy anisotropy (assuming a chemical composition similar to that inferred at the source of Galactic cosmic rays), offering means to constrain the chemical composition of the source. This test has been applied on the Pierre Auger Observatory dataset and no significant anisotropy has been found at energies E/Z , with $E = 55$ EeV and $Z = 6, 14, 26$ (The Pierre Auger Collaboration 2011).

In this chapter, we push further and generalize this idea by considering the amount of secondary protons produced through photodisintegration interactions of the primary nuclei. We provide detailed analytical and numerical estimates of the ratio of significance of the anisotropy at E/Z vs E , and derive the maximal distance to the source D_{\max} in order to avoid the formation of a stronger anisotropy pattern produced by the secondary protons at energy E/Z . This bound does not depend on the amount of protons produced by the source. We also discuss how the comparison of the anisotropy ratio constrains the metal abundance in the source, independently of the injection spectral index, and emphasize how large this metal abundance must be, if the anisotropies persist at high energies, but not at low energies. Finally, we briefly discuss the prospects for the detection of anisotropies at higher energies than E , with next generation experiments, based on current reports of anisotropies at E .

The layout of this chapter is arranged as follows. In § 3.2, we discuss how the absence of a low-energy anisotropy signal could constrain the source distance and its metal abundance. In §3.3, we discuss the low energy proton fraction and the possible anisotropy signal at higher energies, as well as their implication for the source. We draw some conclusions in §3.4.

3.2 Anisotropies at Constant Rigidity

3.2.1 Low Energy Anisotropy Signal

We assume that some anisotropy is detected within a solid angle $\Delta\Omega$ in the energy range from E_1 to E_2 . Following up on Lemoine & Waxman (2009), we quantify the significance of the anisotropy through its signal-to-noise ratio. Before doing so,

we define the injected spectrum of an element with nuclear charge number Z as

$$q_{Z,\text{inj}} = k_Z E^{-s}, \quad (3.1)$$

with s the power law index and k_Z the relative abundance of this element at a given energy. Provided that the maximum energy $E_{Z,\text{max}}$ and the minimum energy $E_{Z,\text{min}}$ of the accelerated spectrum are proportional to Z , i.e. scale with rigidity, the total mass of the element of charge Z and mass A_Z scales as

$$M_Z \propto A_Z \int q_{Z,\text{inj}} dE \propto k_Z A_Z Z^{1-s}. \quad (3.2)$$

Note that the above result does not depend on the magnitude of s , and the missing prefactor does not depend on Z . This implies in particular that the ratio of the relative abundance of a species at a given energy to that of hydrogen takes the form

$$\frac{k_Z}{k_p} = Z^{s-1} A_Z^{-1} \frac{M_Z}{M_H}. \quad (3.3)$$

We then denote respectively the number of injected and propagated primary cosmic rays with nuclear charge Z in the energy range $[E_1, E_2]$ by $N_{Z,\text{inj}}(E_1; E_2)$ and $N_{Z,\text{prop}}(E_1; E_2)$. These two quantities are related through

$$N_{Z,\text{prop}}(E_1; E_2) = f_{Z,\text{surv}}(E_1; E_2) N_{Z,\text{inj}}(E_1; E_2), \quad (3.4)$$

where

$$f_{Z,\text{surv}}(E_1; E_2) \equiv \frac{\int_{E_1}^{E_2} q_{Z,\text{prop}}(E) dE}{\int_{E_1}^{E_2} q_{Z,\text{inj}}(E) dE} \quad (3.5)$$

is the surviving fraction of primaries after propagation.

As we do not know the precise composition of cosmic ray events constituting the anisotropy signal, in a first scenario (A) we regard the fragments with less than $Z/4$ lost nucleons as primaries (i.e., $q_{Z,\text{prop}} = \sum_{i=3/4Z}^Z q_{i,\text{prop}}$). This ad-hoc choice guarantees that all arriving nuclei in the energy range $[E_1, E_2]$ which have suffered at most $Z/4$ photodisintegration interactions retain a similar rigidity, and thus follow a similar path in the intervening magnetic fields. Lighter nuclei, i.e. those that have suffered more than $Z/4$ interactions and arrive in $[E_1, E_2]$ carry higher rigidity. Depending on the intervening magnetic fields, such cosmic rays may or may not contribute to the anisotropies, since the magnetic fields may form a blurred image centered on the source (with higher rigidity cosmic rays clustering closer to the source direction), or impart a systematic shift in the

arrival directions, in which case the higher rigidity particles might lie outside $\Delta\Omega$, e.g. Waxman & Miralda-Escudé (1996); Kotera & Lemoine(2008). To account for this uncertainty, we will consider in the following an alternative scenario (B), in which $E_2 \rightarrow +\infty$ and as many photodisintegration interactions are allowed (i.e., $q_{Z,\text{prop}} = \sum_{i=2}^Z q_{i,\text{prop}}$), provided the nucleus arrives with energy $> E_1$. In this scenario (B), we thus sum up over all rigidities in excess of E_1/Z .

We adopt the premise that anisotropy in the arrival distribution of UHECR nuclei has been detected at high energies between E_1 and E_2 , ie. at energies of the order of the GZK energy. Since protons with the same rigidity have energies between E_1/Z to E_2/Z , one may safely neglect their subsequent energy losses given that their loss lengths at these energies are of the order of ~ 1 Gpc, considerably larger than the source distance considered here ($\lesssim 100$ Mpc). Photodisintegration interactions of nuclei with energy in the range $(A_Z/Z)[E_1, E_2] \approx [2E_1, 2E_2]$ produce secondary protons with energy in the range $[E_1/Z, E_2/Z]$, with number

$$N_{p,\text{dis}}(E_1/Z; E_2/Z) = A_Z f_{Z,\text{loss}}(2E_1; 2E_2) N_{Z,\text{inj}}(2E_1; 2E_2) = 2^{1-s} A_Z f_{Z,\text{loss}}(2E_1; 2E_2) N_{Z,\text{inj}}(E_1; E_2), \quad (3.6)$$

where

$$f_{Z,\text{loss}}(2E_1; 2E_2) \equiv \frac{\int_{E_1/Z}^{E_2/Z} q_{p,\text{dis}} dE}{A_Z \int_{2E_1}^{2E_2} q_{Z,\text{inj}} dE}. \quad (3.7)$$

In this expression, $q_{p,\text{dis}}$ represents the spectrum of secondary protons produced during propagation.

At low energies, the primary protons also contribute to the anisotropy, with

$$N_{p,\text{prop}}(E_1/Z; E_2/Z) \simeq N_{p,\text{inj}}(E_1/Z; E_2/Z) = \frac{M_H}{M_Z} A_Z N_{Z,\text{inj}}(E_1; E_2). \quad (3.8)$$

Note that the last equality is of particular interest. It shows that

$$N_{p,\text{prop}}(E_1/Z; E_2/Z)/N_{Z,\text{inj}}(E_1; E_2) = (M_H/M_Z) A_Z \quad (3.9)$$

controls the scaling of the signal-to-noise ratio of the low energy to high energy anisotropy signals. This scaling factor does not depend on the injection spectrum index, but does depend on the metal abundance at the source. It remains valid for general injection spectra, provided this spectrum is shaped by rigidity, i.e. $q_{Z,\text{inj}}(E) \propto \phi(E/Z)$, with ϕ an arbitrary function.

The noise is given by the square root of number of events expected from the averaged all-sky spectrum of UHECRs in the same solid angle $\Delta\Omega$. The observed

spectrum of the isotropic background can be approximately described by a broken power law beyond $\sim 10^{18}$ eV (The Pierre Auger Collaboration 2010c), i.e.,

$$\left. \frac{dN_{\text{iso}}}{dE} \right|_{\text{iso}} = N_0 \times \begin{cases} (E/E_b)^{-p_1} & E < E_b, \\ (E/E_b)^{-p_2} & E \geq E_b \end{cases} \quad (3.10)$$

where $p_1 = 2.6$, $p_2 = 4.3$ and $E_b = 10^{19.46}$ eV. N_0 represents the overall amplitude, which cancels out in the following calculation. The noise counts in the energy range $[E_1, E_2]$ then reads

$$N_{\text{iso}}(E_1; E_2) = \Delta\Omega \int_{E_1}^{E_2} \frac{dN_{\text{iso}}}{dE} dE \quad (3.11)$$

and for the low energy noise we have

$$N_{\text{iso}}(E_1/Z; E_2/Z) = \Delta\Omega \int_{E_1/Z}^{E_2/Z} \frac{dN_{\text{iso}}}{dE} dE = \eta Z^{p_1-1} N_{\text{iso}}(E_1; E_2), \quad (3.12)$$

with $\eta \equiv (1 - p_2)(1 - p_1)^{-1} (E_2^{1-p_1} - E_1^{1-p_1}) (E_2^{1-p_2} - E_1^{1-p_2})^{-1} E_b^{p_1-p_2}$. The above equation is valid for $E_1 > E_b$ and $E_2/Z < E_b$, which is the case of the "Cen A excess". If $E_2 < E_b$ or $E_1/Z > E_b$, Eq. (11) will read $Z^{p_1-1} N_{\text{iso}}(E_1; E_2)$ or $Z^{p_2-1} N_{\text{iso}}(E_1; E_2)$ respectively.

Assuming the anisotropy is mainly caused by cosmic ray nuclei with charge Z , the signal-to-noise ratio in the energy range $[E_1, E_2]$ can then be expressed as

$$\Sigma_Z(E_1; E_2) = \frac{N_{Z,\text{prop}}(E_1; E_2)}{\sqrt{N_{\text{iso}}(E_1; E_2)}} = \frac{f_{Z,\text{surv}}(E_1; E_2) N_{Z,\text{inj}}(E_1; E_2)}{\sqrt{N_{\text{iso}}(E_1; E_2)}}, \quad (3.13)$$

while the S/N of the low energy anisotropy produced by protons with the same rigidity is

$$\begin{aligned} \Sigma_p(E_1/Z; E_2/Z) &= \frac{N_{p,\text{prop}}(E_1/Z; E_2/Z) + N_{p,\text{dis}}(E_1/Z; E_2/Z)}{\sqrt{N_{\text{iso}}(E_1/Z; E_2/Z)}} \\ &= \frac{A_Z \left[M_H/M_Z + 2^{1-s} f_{Z,\text{loss}}(2E_1; 2E_2) \right] N_{Z,\text{inj}}(E_1; E_2)}{\sqrt{\eta Z^{p_1-1} N_{\text{iso}}(E_1; E_2)}}. \end{aligned} \quad (3.14)$$

Consequently, the ratio of the signal-to-noise ratios at low to high energy reads

$$\frac{\Sigma_p}{\Sigma_Z} = \frac{2M_H/M_Z + 2^{2-s} f_{Z,\text{loss}}(2E_1; 2E_2)}{f_{Z,\text{surv}}(E_1; E_2) \sqrt{\eta Z^{p_1-3}}}, \quad (3.15)$$

and if no anisotropy is recorded at low energies, one requires $\Sigma_p/\Sigma_Z < 1$. For reference, the Pierre Auger Observatory data indicate that, for the Cen A excess,

$\Sigma_p/\Sigma_Z \lesssim (2., 1.8, 0.8)$ at the 95% c.l., for $Z = 6, 14, 26$ corresponding to carbon, silicon and iron (The Pierre Auger Collaboration 2011). The exact number depends on the statistics (which of course have increased since this analysis was carried out), and on the elements adopted in the analysis. In the following, we use the constraint $\Sigma_p/\Sigma_Z < 1$ to impose a limit on the maximum source distance.

In terms of the (inverse) metal abundance, this constraint can be rewritten

$$\frac{M_H}{M_Z} < \frac{1}{2} \left[\sqrt{\eta Z^{p_1-3}} f_{Z,\text{surv}}(E_1; E_2) - 2^{2-s} f_{Z,\text{loss}}(2E_1; 2E_2) \right]. \quad (3.16)$$

Again, if secondary protons are ignored, meaning $f_{Z,\text{loss}}(2E_1; 2E_2) \rightarrow 0$ in the above, then the non-detection of anisotropy at low energies imposes a lower limit of M_Z/M_H which does not depend on the spectral index. Note that this statement is not in contradiction with the statement in the (The Pierre Auger Collaboration 2011), that the limit on the quantity f_p/f_Z used in that paper depends on the spectral index. This is due to the fact that f_p/f_Z , which is defined at a given energy, is not the "proton to heavy fraction in the source" or the "relative proton abundance", as it is misleadingly referred to in the Auger paper (in the notation of that paper, the relative proton abundance is k_p/k_Z , which is equivalent to our M_p/M_Z).

The minimum required metallicity of the element responsible for the observed anisotropy thus depends on the value of $f_{Z,\text{surv}}$ and $f_{Z,\text{loss}}$, which are directly determined by the source distance. A larger source distance will result in a smaller $f_{Z,\text{surv}}$ and a larger $f_{Z,\text{loss}}$ as more nuclei are photodisintegrated. There exists therefore a critical distance, beyond which the abundance of hydrogen in the source relative to metals becomes negative. This happens when $f_{Z,\text{loss}}(2E_1; 2E_2)/f_{Z,\text{surv}}(E_1; E_2) \geq 2^{s-2} \sqrt{\eta Z^{p_1-3}}$, meaning that even if the source injects no primary protons, secondary protons produced during propagation cause a stronger anisotropy at low energies. Therefore, the critical distance, which we denote by D_{max} hereafter, is the upper limit of the distance of the source responsible for the anisotropy signal in $[E_1, E_2]$. The value of D_{max} is also related to the primary cosmic ray species adopted and the injection spectrum used. Once these parameters are given, we can uniquely determine D_{max} by finding the distance for which $\Sigma_p(E_1/Z; E_2/Z)/\Sigma_Z(E_1; E_2) = 1$ using the method outlined above.

3.2.2 Photodisintegration of Nuclei

Ultra-high energy cosmic rays interact with the CMB and EBL photons while they propagate through extragalactic space. For nuclei, energy losses due to the photodisintegration process and the Bethe–Heitler process (pair production) by CMB photons are comparable around 55 EeV. As energy increases, the photodisintegration process plays a more and more dominant role in the energy loss process. Photodisintegration does not change the Lorentz factor of the cosmic ray nucleus, but does lead to the nucleus losing one or several nucleons as well as α particles through the giant dipole resonance (GDR) or quasi–deuteron (QD) process. These secondary nuclei can be further disintegrated to protons. On average, the mass number of a nucleus evolves as (Stecker 1969)

$$-\frac{dA}{dx} = \frac{1}{2\gamma_A^2} \sum_i \Delta A_i \int_{\epsilon_{\text{th},i}}^{\infty} d\epsilon \sigma_{\text{dis},i}^A(\epsilon) \epsilon \int_{\epsilon/2\gamma_A}^{2\gamma_A\epsilon} d\epsilon_\gamma \frac{n_\gamma(\epsilon_\gamma, z)}{\epsilon_\gamma^2} \quad (3.17)$$

with $\sigma_{\text{dis},i}^A$ the cross-section for photodisintegration through the i th channel (e.g., single–nucleon emission, deuterium emission, α particle emission and so on), and $\epsilon_{\text{th},i}$ the threshold energy of the i th channel, which is $\sim 10 - 20$ MeV for all species of nuclei for the GDR process and ~ 30 MeV for the QD process. ΔA_i is the number of nucleon lost through the i th channel (e.g., $\Delta A = 1, 2, 4$ for single nucleon emission, deuteron and α particle emission and so on). ϵ_γ and $n_\gamma(\epsilon_\gamma, z)$ are respectively the photon energy and the number density of the target photon field in the lab frame at redshift z while ϵ is the photon energy in the rest frame of the nucleus. The physics of UHE nuclei transport through the radiation backgrounds has been discussed by a number of authors, e.g. (Puget et al. 1976; Bertone et al. 2002; Khan et al. 2005; Hooper et al. 2008; Aloisio et al. 2012). In this work, we adopted the tabulated cross-section data generated by the code TALYS and implemented them into the Monte–Carlo framework along with other energy loss processes, as described in Hooper et al. (2007), to obtain the propagated spectra.

As Monte Carlo simulations of nuclei propagation remain somewhat costly in computing, it is useful to have a simple analytical estimate of the photodisintegration process. Detailed treatments are discussed in (Hooper et al. 2008; Aloisio et al. 2013; Aloisio et al. 2013b). Here, we adopt an even simpler approximation, which provides a sufficiently reliable approximation for the integrations that follow. In this analytical treatment, only the photodisintegration process is taken into account, with all other energy loss processes being neglected. A

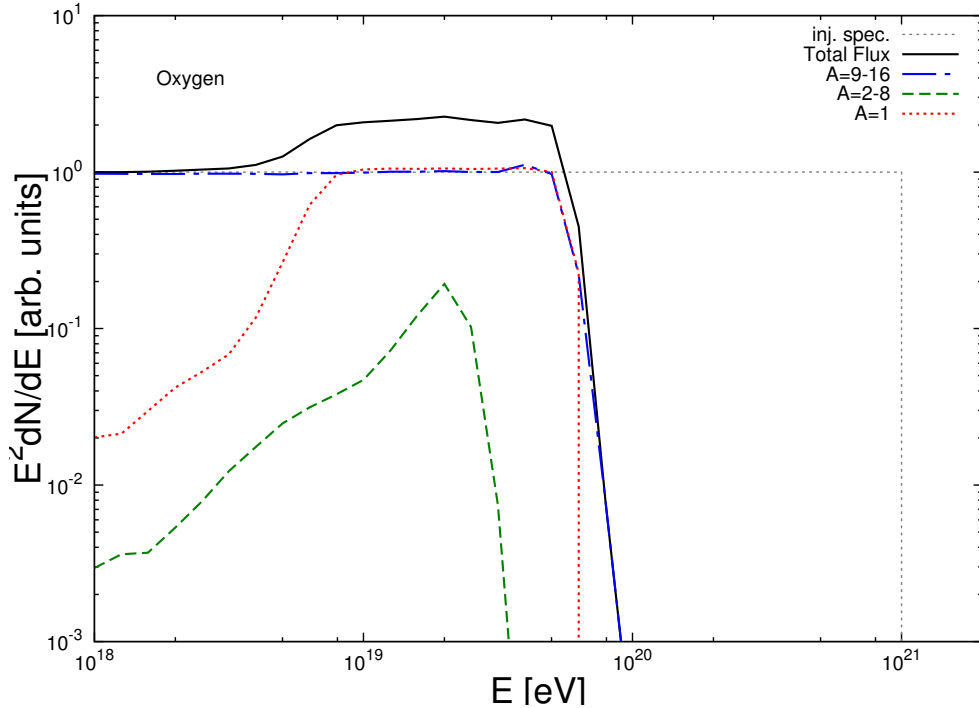


Figure 3.1: An example of propagated spectrum of UHECRs. The injection particles are oxygen nuclei which travel a distance of 50 Mpc. The initial spectrum is set to be a power-law spectrum with index of -2 and with an abrupt cutoff at 10^{21} eV. The figure is taken from Liu et al. (2012)

Table 3.1: The best-fit parameters for nucleon loss rate through a MCMC method.

	c_1	c_2
a_1	9.99×10^{-5}	2.11×10^{-3}
a_2	7.43×10^{-3}	0.31
a_3	0.69	1.15
a_4	1.79	2.80

phenomenological fit of the nucleon loss rate dA/dx for a nucleus with initial mass number A_0 and Lorentz factor γ :

$$-\frac{dA}{dx} = c_1(\gamma_{10})A^2 + c_2(\gamma_{10})A \text{ Mpc}^{-1} \quad (3.18)$$

where $c_1(\gamma_{10})$ and $c_2(\gamma_{10})$ are functions of the Lorentz factor of cosmic ray nuclei in unit of 10^{10} , which can be written in the form of $a_1\gamma_{10} + a_2\exp(-a_3/\gamma_{10}^{a_4})$.

Table 1 presents the results from a Markov Chain Monte Carlo exploration of the parameter space and Fig. 3.2 shows the phenomenologically fit and numeri-

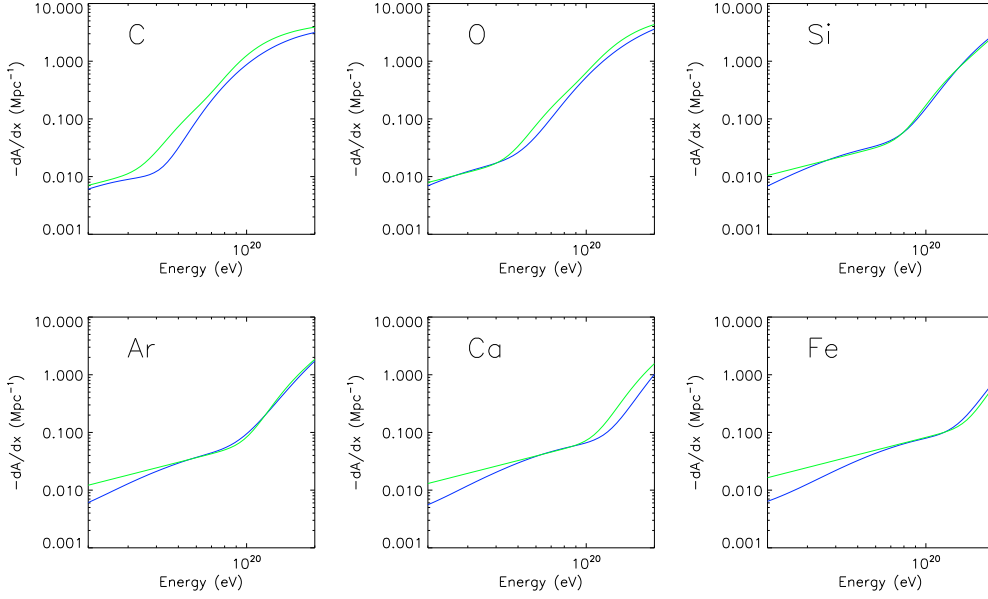


Figure 3.2: The phenomenological fit of nucleon loss rate for some species of cosmic rays. The blue lines are numerically calculated results while the green ones are plotted based on the analytical expressions (Eq. 3.18).

cal nucleon loss rate respectively for several cosmic ray species. From Eq. (3.18) we can derive the average mass number of a nucleus of initial mass number A_0 and Lorentz factor γ_{10} after propagation over a distance x :

$$A(x, \gamma_{10}) = \frac{A_0 c_2 e^{-c_2 x}}{A_0 c_1 (1 - e^{-c_2 x}) + c_2}. \quad (3.19)$$

For Poisson statistics with mean rate dA/dx , the probability that a nucleus undergoes at most N interactions reads

$$P_N(A_Z, x, E) \equiv \frac{\Gamma [N + 1, x |dA/dx|]}{\Gamma [N + 1]}. \quad (3.20)$$

Strictly speaking, Eq. (3.18) leads to modified Poisson statistics, because the rate dA/dx depends on A , which evolves as photodisintegration interactions occur. It is possible to derive the generalized probability law for P_N , at the expense of tedious calculation; however, as we demonstrate in the following, the above form for P_N provides a sufficient approximation for our case of interest.

One may then derive the propagated spectra, surviving fractions and secondary proton spectra used in the previous subsection, as follows. Consider first the simpler scenario (B) in which one sums up over all fragments with rigidities

in excess of E_1/Z . Writing $Q_{Z,\text{prop}}(E) = E q_{Z,\text{prop}}(E)$ the number of particles per log interval, and neglecting losses other than photodisintegration, one finds

$$Q_{Z,\text{prop}}(E) = \sum_{i=0}^{A_Z-1} p_i \left(A_Z, x, \frac{E}{1-i/A_Z} \right) Q_{Z,\text{inj}} \left(\frac{E}{1-i/A_Z} \right), \quad (3.21)$$

with $p_i(A_Z, x, E) \equiv (x |dA/dx|)^i \exp(-x |dA/dx|) / i!$ the probability to undergo i photodisintegration interactions over a distance x , thereby decreasing the injection energy from $E/(1-i/A_Z)$ down to E .

Then, the fraction of surviving fragments with rigidity $> E_1/Z$ can be obtained as

$$\begin{aligned} f_{Z,\text{surv}}(> E_1) &= \frac{1}{\int_{E_1}^{+\infty} q_{Z,\text{inj}}(E) dE} \int_{\ln E_1}^{+\infty} d \ln E Q_{Z,\text{prop}}(E) \\ &= \frac{1}{\int_{E_1}^{+\infty} q_{Z,\text{inj}}(E) dE} \int_{E_1}^{+\infty} dE q_{Z,\text{inj}}(E) P_j(A_Z, x, E), \end{aligned} \quad (3.22)$$

with $j \equiv \min \{A_Z - 1, \text{Int}[A_Z (1 - E_1/E)]\}$ and that $P_j(A_Z, x, E) = \sum_{i=0}^j p_i(A_Z, x, E)$. To go from the first to the second equality in the above equation, first explicit the discrete sum as in Eq. 3.21, take the sum out of the integral, and then change variables in the integration from $E \rightarrow E' \equiv E/(1-i/A)$. This gives

$$f_{Z,\text{surv}}(> E_1) = \frac{1}{\int_{E_1}^{+\infty} q_{Z,\text{inj}}(E) dE} \sum_{i=0}^{A_Z-1} \int_{E_1/(1-i/A)}^{\infty} dE' p_i(A_Z, x, E') q_{Z,\text{inj}}(E') \quad (3.23)$$

Then exchange the order between sum and integral to switch back the sum into the integral, bearing in mind that integrating from $E_1/(1-i/A)$ to ∞ and then summing from $i = 0$ to $i = A_Z - 1$ is the same as firstly summing from $i = 0$ to j and then integrating from E_1 to ∞ .

The fraction of photodisintegrated nuclei with energy more than $2E$ is given by $f_{Z,\text{loss}}(> 2E) = 1 - f_{Z,\text{surv}}(> 2E)$, and the number of secondary protons is easily evaluated using Eq. (3.6).

In Scenario (A), one considers only the fragments with energy in the range $[E_1, E_2]$, which have suffered at most $Z/4$ photodisintegration interactions, so as to study a group of nuclei with similar rigidities. Eq. (3.21) remains valid, if the sum over i runs from $i = 0$ to $i = Z/4$, therefore one finds

$$f_{Z,\text{surv}}(E_1; E_2) = \frac{1}{\int_{E_1}^{E_2} q_{Z,\text{inj}}(E) dE} \left\{ \int_{E_1}^{+\infty} dE q_{Z,\text{inj}}(E) P_{j_1}(A_Z, x, E) - \int_{E_2}^{+\infty} dE q_{Z,\text{inj}}(E) P_{j_2}(A_Z, x, E) \right\}, \quad (3.24)$$

with $j_1 = \min\{Z/4, \text{int}[A(1 - E_1/E)]\}$, $j_2 = \min\{Z/4, \text{int}[A(1 - E_2/E)]\}$. Here as well, one defines $f_{Z,\text{loss}}(> 2E) = 1 - f_{Z,\text{surv}}(> 2E)$, and the number of secondary protons is easily evaluated using Eq. (3.6).

3.2.3 Results

So far, our treatment has remained quite general. Here, we apply it to the specific case of the "Cen A excess" reported by the Pierre Auger collaboration. We thus use $E_1 = 55 \text{ EeV}$, $E_2 = 84 \text{ EeV}$ and assume for simplicity that the source injects a pure oxygen, silicon or iron composition. In Fig. 3.3 we show both the analytical and the numerical results of the ratio of anisotropy significance at low to high energies as a function of the distance to the source that is responsible for the anisotropy. In this figure, we do not assume any proton component in the source composition, so that $N_{p,\text{prop}} \rightarrow 0$, $M_H/M_Z \rightarrow 0$ in Eqs. (3.14) and (3.15). We adopt an exponential cut-off power law spectrum, as generally expected, with a cut-off energy $E_{\text{max}} \propto Z$. The four panels correspond to different injection spectral indices and maximal energies. As can be seen, these results share the following common features.

At small source distances, the anisotropy signal produced by secondary protons is less prominent than the high energy one, because only a few primary nuclei photodisintegrate on this short path length. As more and more secondary protons are produced with increasing source distance, this ratio grows and eventually exceeds unity. In the case $s = 2$, $E_{\text{max}} = (Z/26) \times 10^{21} \text{ eV}$, both the analytical treatment and the numerical treatment result in a maximum source distance of $\sim 15 \text{ Mpc}$, $\sim 60 \text{ Mpc}$ and $\sim 180 \text{ Mpc}$ for oxygen nuclei, silicon nuclei and iron nuclei respectively. Note that for $E_{\text{max}} = (Z/26) \times 10^{21} \text{ eV}$, the source produces protons of energy $\gtrsim 40 \text{ EeV}$: such protons would presumably produce a strong anisotropy, though its magnitude would depend strongly on the distribution and characteristics of intervening magnetic fields. We show therefore the case with a high E_{max} for the sake of generality in order to illustrate the dependence of the results on the maximal energy.

From lighter to heavier nuclei, the constraint on the source distance becomes weaker, since at a given energy lighter nuclei carry a comparatively larger Lorentz factor, and as a consequence, their energy lies further beyond the photodisintegration interaction threshold (see also Fig. 3.2). The small differences of D_{max} for the same species among the four panels can be interpreted as follows: protons at E/Z all come from primary nuclei at $2E$, so a smaller cut-off energy or a steeper

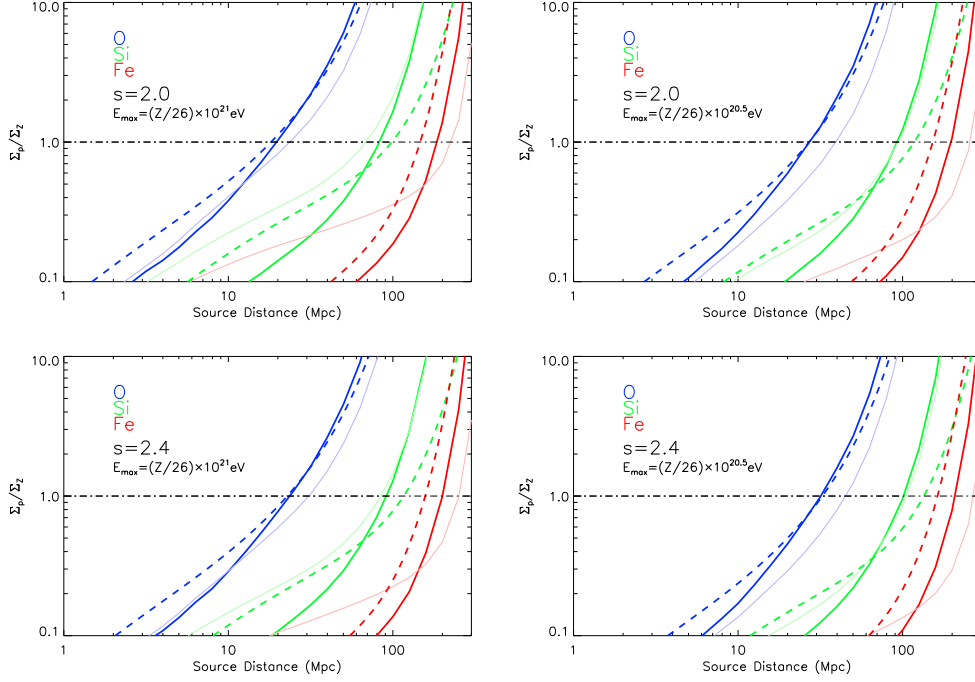


Figure 3.3: Ratio of anisotropy significance at low to high energies as a function of the distance to the sources responsible for the anisotropy. Solid lines represent the numerical results while dashed lines represent the analytical results; thick solid line: scenario (A), in which one sums up over fragments of similar rigidity, in interval $[E_1, E_2]$, with at most $Z/4$ photodisintegration interactions; thin solid lines: scenario (B), in which one sums up over all fragments with rigidities in excess of E_1/Z . The source is assumed to inject pure O, Si or Fe composition as indicated.

power-law slope will decrease the amount of primary nuclei at $2E$, leading to less secondary protons produced at E/Z , so that the values of maximum source distances in these cases are larger.

Another way to plot these results is to consider the minimum metal abundance M_Z/M_H that is required at the source in order to satisfy the bound $\Sigma_p/\Sigma_Z < 1$. The results are shown in Fig. 3.4 as a function of the distance to the source. All four panels indicate that the mass ratio of nuclei to proton $\gtrsim 1 : 1$ is needed. Of course, as the distance increases, so does the minimum M_Z/M_H , in order to compensate for the greater number of secondary protons produced during propagation. The distance where $M_Z/M_H \rightarrow +\infty$ corresponds to D_{max} . Conversely, the asymptote as $D \rightarrow 0$ indicate the minimum M_Z/M_H amount when secondary protons can be safely neglected.

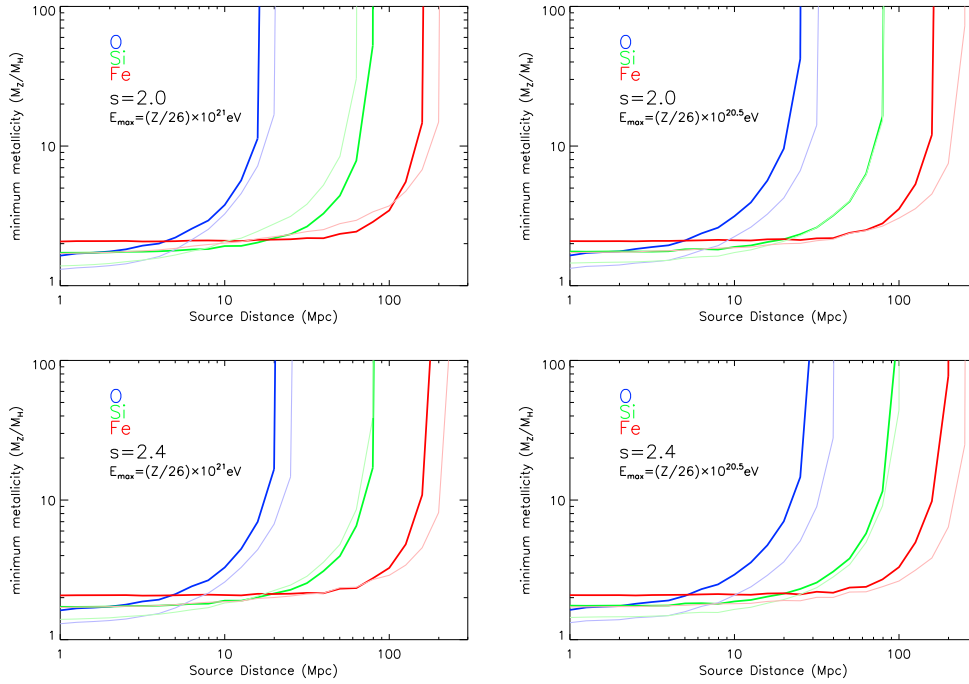


Figure 3.4: The minimum metal mass relative to hydrogen in the source, assuming pure O, Si or Fe compositions are injected. Thick solid lines and thin solid lines respectively represent results in scenario (A) and (B), which are the same as in Fig. 3.3.

3.3 Discussion

The method presented above remains rather general and could be applied to datasets of next generation experiments. Nevertheless, the results obtained in Figs. 3.3 and 3.4 assume tacitly that the heavy chemical composition and the anisotropy signal reported by the PAO are not artifacts. It is fair to say that these two results remain disputed. The significance of the anisotropy, for instance, is not comfortably high, and deserves to be improved with extended datasets. The measurements of the chemical composition by the High Resolution Fly’s Eye Experiment (HiRes) and Telescope Array (TA) differ appreciably from that of the PAO. In particular, their data of $\langle X_{\max} \rangle$ and rms $\sigma_{X_{\max}}$ show a proton dominated spectrum at all energies $> 10^{18}$ eV (Abbasi et al. 2010; Tsunesada 2011). One should not expect to detect anisotropies at low energies if the composition were pure proton, as the low energy protons have a much smaller rigidity than the high energy ones. On the other hand, the analysis of the chemical composition depends on the details of the hadronic interaction model, such as the cross

sections, multiplicities and so on. The fact that these parameters are presently poorly constrained prevents one from drawing firm conclusions. As for the apparent anisotropy, Clay et al. (2010) has shown that there is no significant difference between the energy distribution of the events inside and outside the 25° window of Cen A using a K-S test, implying events around Cen A do not have any special origin; such an analysis cannot provide however a conclusive answer, given the limited event statistics presently available. Additionally, two recent papers suggest that at most 5–6 of events around Cen A can originate from it by backtracing the events' trajectories in the intervening magnetic field (Farrar et al. 2012; Sushchov et al. 2012). We should, however, be cautious with such strong conclusions given that they depend on the magnetic field model adopted, which still carries a large degree of uncertainty.

3.3.1 Source Metallicity

With the above caveats in mind, it is interesting to discuss where the previous results lead us. The constraints derived from Fig. 3.4 are indeed quite strong. For reference, the solar composition (Lodders & Palme 2009) corresponds to $M_{\text{H}}/M_{\text{CNO}} \sim 70$, $M_{\text{H}}/M_{\text{Si}} \sim 900$ and $M_{\text{H}}/M_{\text{Fe}} \sim 550$. Consequently, the minimum metallicities required to match $\Sigma_p/\Sigma_Z < 1$, notwithstanding the secondary protons, are $\sim 120Z_\odot$ for CNO, $\sim 1600Z_\odot$ for Si and $\sim 1100Z_\odot$ for iron like nuclei. The comparison to Z_\odot is less severe for oxygen, but this nucleus is also more fragile and the minimum metallicity diverges rapidly beyond some 20 – 30 Mpc. Conversely, the production of secondary protons is less severe for iron nuclei, but for such nuclei, the minimum requirements on the source metallicity are already quite extraordinary.

The observables $\langle X_{\text{max}} \rangle$ and $\sigma_{X_{\text{max}}}$, as reported by the Pierre Auger Observatory, suggest that the all-sky-averaged composition of arriving UHECRs may be oxygen-like (Hooper & Taylor 2010). If the anisotropy signal observed by the PAO mainly consists of oxygen-like nuclei, our calculations indicate that the source responsible for the anisotropy should lie within 20 – 30 Mpc. There are only a limited number of known powerful radio-galaxies within this distance, such as Cen A, M87. Such radio-galaxies are relatively weak, in terms of jet power and magnetic luminosity, which implies that they cannot accelerate particles beyond $E_{\text{max}} \sim Z \times 10^{18} - 10^{19}$ eV, see the discussion in (Lemoine & Waxman 2009). Even assuming that these sources accelerate oxygen nuclei to the highest energies, the minimum metallicity required by the above arguments lies well above what is

measured in the central parts of such radio-galaxies (Hamann & Ferland 1999). The situation becomes even worse if one considers silicon or heavier nuclei. Consequently, and as already emphasized in Lemoine & Waxman (2009), the current dataset of the Pierre Auger Observatory about the clustering of UHECR events does not support acceleration of UHECRs in these objects.

If future datasets would confirm the existence of anisotropies at high energies, and the absence of anisotropies at low energies, then the present work provides strong constraints on the nature and the source of ultra-high energy cosmic rays: either protons exist at ultra-high energies, and some of them are responsible for the observed anisotropies (in which case no anisotropy is indeed expected at lower energies); or, a close-by source with rather extraordinarily high metallicity produces these anisotropies. The only physically motivated scenario for such a source so far is acceleration at the external shock of a semi-relativistic hyper-novae inside the wind of the progenitor (Wang et al. 2007, Budnik et al. 2008, Liu & Wang 2012a).

3.3.2 Composition Close to the Ankle

Provided the same source population produces both UHECRs with energy $> E_1$ and $> E_1/Z$, the proton fraction at E_1/Z becomes an interesting aspect of the problem. The key point indeed is that if $M_Z \gtrsim M_H$ inside the sources, as suggested by the above discussion, and all sources are alike, then the chemical composition at E_1/Z must contain a significant heavy component¹. More specifically, the fraction of protons at low energies is given by

$$x_p(E_1/Z; E_2/Z) = \frac{\tilde{N}_p(E_1/Z; E_2/Z)}{\tilde{N}_{Z,\text{prop}}(E_1/Z; E_2/Z) + \tilde{N}_p(E_1/Z; E_2/Z)} \quad (3.25)$$

where $\tilde{N}_p = \tilde{N}_{p,\text{prop}} + \tilde{N}_{p,\text{dis}}$ is the total proton number, including the contribution from secondary protons and primary protons, as integrated over all sources, and similarly for $\tilde{N}_{Z,\text{prop}}$. Here we neglect the partially disintegrated fragments. Assuming every source has equal emissivity and the same injection spectrum, we have

$$\tilde{N}_{Z,\text{prop}}(E_1; E_2) \simeq \int_{(1+z)E_1/Z}^{(1+z)E_2/Z} q_{Z,\text{inj}}(E) dE \int_0^{I_{Z,\text{loss}}(E)} n(z) f_{Z,\text{surv}}(E) dD_c(z) \quad (3.26)$$

and

$$\tilde{N}_{p,\text{dis}}(E_1; E_2) \simeq A_Z \int_{2(1+z)E_1}^{2(1+z)E_2} q_{Z,\text{inj}}(E) dE \int_0^{I_{p,\text{loss}}(E/A_Z)} n(z) f_{Z,\text{loss}}(E) dD_c(z). \quad (3.27)$$

¹We thank S. Nagataki for suggesting this to us

Here $n(z)$ is the source density as a function of redshift z and $D_c(z)$ is the comoving distance to the light cone at redshift z ; $l_{Z,\text{loss}}$ and $l_{p,\text{loss}}$ represent the energy loss lengths $|E/(dE/dx)|$ for nuclei and protons respectively. The second equation assumes that photodisintegration takes place on short distance scales compared to $l_{p,\text{loss}}(E/A_Z)$, which is a very good approximation. The energy losses to be considered here includes all processes besides photodisintegration, such as pair production, adiabatic cooling etc. Since the energy loss distance of protons with energy $(1+z)E/Z$ is much larger than the energy loss distance of nuclei at energy $2(1+z)E$, $f_{Z,\text{loss}}[2(1+z)E] \rightarrow 1$ for most sources. On the other hand, $f_{Z,\text{surv.}}[(1+z)E/Z] \approx \exp\{-D_c/l_{Z,\text{loss}}[(1+z)E/Z]\}$ and given that $l_{Z,\text{loss}}[(1+z)E/Z]$ is the upper limit of integration, we have² $e^{-1} \lesssim f_{Z,\text{surv.}} \lesssim 1$. For an estimation here we take $f_{Z,\text{surv.}} = 1$. Then, the above two equations can be written as

$$\tilde{N}_{Z,\text{prop}}(E_1; E_2) \approx k_Z Z^{s-1} \bar{E}^{1-s} \int_0^{l_{Z,\text{loss}}(\bar{E}/Z)} (1+z)^{1-s} n(z) dD_c \quad (3.28)$$

$$\tilde{N}_{p,\text{dis}}(E_1; E_2) \approx k_Z 2^{1-s} \bar{E}^{1-s} A_Z \int_0^{l_{p,\text{loss}}(\bar{E}/Z)} (1+z)^{1-s} n(z) dD_c. \quad (3.29)$$

Since $[E_1, E_2]$ is a narrow energy range, we denote the average energy in this range by \bar{E} . Considering that $n(z)$ usually evolves with redshift z , we make here a further approximation that the term $(1+z)^{1-s}$ cancels the evolution in $n(z)$ to some extent and the integrand is reduced to a constant. Then one can find that

$$x_p(E_1; E_2) \approx \frac{1 + 2^{s-1} M_H/M_Z}{1 + 2^{s-1} M_H/M_Z + A_Z^{s-2} l_{Z,\text{loss}}(\bar{E}/Z)/l_{p,\text{loss}}(\bar{E}_{\text{thr}}/Z)}. \quad (3.30)$$

In the local Universe, for oxygen nuclei, $[E_1/Z, E_2/Z] \sim [7, 10]$ EeV, hence the energy loss in this energy range is comparably caused by photodisintegration on EBL photons and pair production on CMB photons, leading to an energy loss length of $\sim 2 - 3$ Gpc. For silicon and iron nuclei, $[E_1/Z, E_2/Z] \sim [4, 6]$ EeV and $[2, 3]$ EeV respectively, in which energy range the dominant cooling process is adiabatic cooling with an energy loss length ~ 4 Gpc. For protons, however, the dominant energy loss process in the corresponding energy range is caused by pair production on CMB photons with an energy loss length $\sim 1 - 2$ Gpc. Therefore typically, the energy loss length for nuclei is larger than that for protons by a factor of 2-3. If $2^{s-1} M_H/M_Z \lesssim 1$, as suggested by the previous discussion, this implies in turn that the composition in $[E_1/Z, E_2/Z]$ should comprise less than

²If we also consider the slightly disintegrated fragments as surviving primaries, $f_{Z,\text{surv.}}$ will be closer to unity

$\sim 50\%$ protons, in potential conflict with the claims of a light composition close to the ankle of the cosmic ray spectrum.

Looking at this argument the other way round, the data from the Pierre Auger Observatory shows evidence for the UHECR mass composition becoming progressively heavier at energies $\gtrsim 4$ EeV, while below this energy the same data suggests a proton-like composition. Thus, we should expect $M_H/M_Z \gtrsim 1$ if the heavy elements at E_1 are mostly silicon or iron nuclei. In this case, Fig. 3.4 indicates that one should have detected a secondary anisotropy at the ankle. For oxygen, however, E_1/Z already lies in an energy range where the composition apparently departs from proton-like, and the above argument is severely weakened.

3.3.3 Trans-GZK Anisotropies

Another interesting aspect is the possible anisotropy signal that one may expect at higher energies, given the reported anisotropies at > 55 EeV. The detection of such anisotropies provides a strong motivation for next generation experiments such as JEM-EUSO (Casolino et al. 2011), which will provide a substantially larger statistics.

Here we start by assuming that the currently observed anisotropy mainly consists of nuclei with charge number Z and that their source also accelerates heavier nuclei with nuclear charge number Z' . These heavier nuclei will produce a similar anisotropy pattern at higher energies $> Z'E_1/Z$; we define $E'_1 = Z'E_1/Z$ for clarity. The ratio of significance between these two anisotropy signals then reads

$$\frac{\Sigma_{Z'}(> E'_1)}{\Sigma_Z(> E_1)} = \frac{M_{Z'} f_{Z',\text{surv.}}(> E'_1)}{M_Z f_{Z,\text{surv.}}(> E_1)} \left(\frac{Z'}{Z}\right)^{(p_2-3)/2}, \quad (3.31)$$

where $f_{Z,\text{surv.}} \approx \exp(-x/l_{Z,\text{loss}})$. With the approximation $A_Z \simeq 2Z$, the two species of nuclei with the same rigidity share approximately the same Lorentz factor. At the same Lorentz factor, heavier nuclei lose energy faster than lighter nuclei, but the differences between the energy loss lengths of different species such as O, Si, Fe with rigidity E/Z are at most a factor of a few; furthermore, the energy loss lengths are larger than the maximum source distance D_{max} that we have obtained in Section 3. So we expect $0.1 \lesssim f_{Z',\text{surv.}}(> E'_1)/f_{Z,\text{surv.}}(> E_1) \lesssim 1$. Also, $p_2 = 4.3$, hence $(Z'/Z)^{(p_2-3)/2} \gtrsim 1$. Therefore, a stronger anisotropy signal is expected at higher energies if the source is more abundant in nuclei Z' than nuclei Z . In this case, however, some accompanying effects will occur and one should also check

whether these effects already cause violations against current measurements or lead to self-contradiction. We consider here the following three aspects.

- secondary protons produced by nuclei Z' above energy E_1/Z . Since nuclei Z' at E'_1 have the same rigidity as the nuclei Z at E_1 , the secondary protons emitted by nuclei Z' will fall well within the energy range of interest. According to Eq. (3.6), we can write the secondary protons above E_1/Z as $N_{p,\text{dis}}(> E_1/Z) = A_Z f_{Z,\text{loss}}(> 2E_1) N_{Z,\text{inj}}(> 2E_1)$. As such, we obtain the ratio between the number of secondary protons produced by nuclei Z' and Z above E_1/Z

$$\frac{N_{p',\text{dis}}}{N_{p,\text{dis}}} = \frac{M_{Z'} f_{Z',\text{loss}}(> 2E'_1)}{M_Z f_{Z,\text{loss}}(> 2E_1)} \quad (3.32)$$

As was discussed above, the energy loss length of nuclei Z' is a bit larger than that of nuclei Z with the same Lorentz factor, so $f_{Z',\text{loss}}(> 2E'_1) \gtrsim f_{Z,\text{loss}}(> 2E_1)$. If the source is more abundant in nuclei Z' than nuclei Z , i.e, $M_{Z'} > M_Z$, nuclei Z' will actually produce more secondary protons than nuclei Z , above energy E_1/Z . As such, when we calculate the low energy proton anisotropy significance, we should also consider the contribution from nuclei Z' and add a non-trivial term to the numerator of Eq. (3.14). Consequently, the maximum source distance derived previously would be further reduced.

- the chemical composition of UHECRs at energy E'_1 : as the UHECR background decreases rapidly with increasing energy, the composition of cosmic rays emitted by the source can strongly influence the composition measurement at higher energies, provided the source accelerates a larger fraction of nuclei Z' than nuclei Z . Although it is difficult to find a quantitative relation between the composition of the source and that of the all-sky averaged composition, one might naively expect that the all-sky averaged composition above a given energy E (denoted as $\xi_Z(> E)$) to be positively related to $A_Z \frac{N_{Z,\text{prop}}(> E)}{N_{\text{iso}}(> E)}$, and we find

$$\frac{\xi_{Z'}(> E'_1)}{\xi_Z(> E_1)} = \frac{M_{Z'} f_{Z',\text{surv.}}(> E'_1)}{M_Z f_{Z,\text{surv.}}(> E_1)} \left(\frac{Z'}{Z}\right)^{p_2-1} = \left(\frac{Z'}{Z}\right)^{\frac{p_2+1}{2}} \frac{\Sigma_{Z'}}{\Sigma_Z} \quad (3.33)$$

As one can see, since $Z' > Z$, if stronger anisotropy signal is detected at higher energies ($\Sigma_{Z'} > \Sigma_Z$), the UHECRs composition is expected to be heavier.

- the surviving nuclei Z' in the energy range between E_1 and E_2 . Assuming that the source is more abundant in nuclei Z' than nuclei Z , the source

should emit a larger amount of nuclei Z' in the energy range E_1 and E_2 . So after propagation, the number of surviving nuclei in a fixed energy range is $\propto f_{Z,\text{surv.}} \int k_Z E^{-s} dE \propto f_{Z,\text{surv.}} M_Z Z^{s-2}$. With the fact that heavier nuclei lose nucleons slower than lighter nuclei at the same energy (not the same Lorentz factor), we expect the ratio of nuclei Z' and nuclei Z emitted by the source in the energy range to be

$$\frac{N_{Z',\text{prop}}(E_1; E_2)}{N_{Z,\text{prop}}(E_1; E_2)} = \frac{M_{Z'} f_{Z',\text{surv.}}(E_1; E_2)}{M_Z f_{Z,\text{surv.}}(E_1; E_2)} \left(\frac{Z'}{Z}\right)^{s-2} > 1 \quad (3.34)$$

It does not mean however that these Z' nuclei would contribute to the anisotropy pattern seen in the range $[E_1, E_2]$, because they have smaller rigidity than the Z nuclei.

If the source does not accelerate nuclei beyond charge Z , then the anisotropy at higher energies is produced by nuclei of charge Z . To derive the corresponding ratio of significances, make the substitution $M_{Z'}/M_Z \rightarrow 1, Z'/Z \rightarrow E'_1/E_1$ in Eq. (29). Then, with $(p_2 - 3)/2 \simeq 0.65$, one expects the ratio to increase slightly up to the energy at which the distance to the source matches the energy loss distances, then to drop sharply beyond this distance. The detection of such a feature would provide useful constraints on Z and D .

3.4 Conclusion

In this Chapter, we have generalized a test of the chemical composition of UHE-CRs, which proposes to use the anisotropy pattern measured as a function of energy. The basic idea is that if an anisotropy signal is observed at high energies $E \sim 6 \times 10^{19}$ eV, and if we assume that the anisotropy is caused by heavy nuclei of charge Z , then we should expect a strong anisotropy signal at energies E/Z close to the ankle, due to the proton component. In this chapter, we have also considered the production of secondary protons through the photodisintegration interactions of nuclei. Assuming that no anisotropy signal is detected at low energies, we derive an upper bound on the distance to the source.

Our numerical estimates are based on the report of the Pierre Auger Observatory of an excess in the direction to Cen A. At present, the significance of this detection is not well established and one must await future data to confirm or invalidate it. Nevertheless, the method presented here remains general and might well be applied to future more extended datasets. Taking the results of the Pierre

Auger Observatory at face value, we derive a maximal distance to the source of order 20 – 30 Mpc, 80 – 100 Mpc, 180 – 200 Mpc if the nuclei responsible for the anisotropies are oxygen, silicon or iron respectively. The differences between these estimates of the maximal distance depend on the energy loss lengths of these nuclei at GZK energies. Our results are summarized in Fig. 3.4, which shows the minimum mass of metals relatively to hydrogen required in the source, in order to produce a weaker anisotropy at E/Z than at E . At distances exceeding the above estimates, this amount diverges, meaning that even if the source does not accelerate any protons, the amount of secondary protons produced during propagation is sufficient to cause a secondary anisotropy at E/Z larger than that observed at E . At small source distances, where the photodisintegration effect is negligible, one nevertheless finds a minimum mass $M_Z/M_H \gtrsim 1$. When measured relatively to the solar composition, this indicates that the metallicity inside the source should exceed $\sim 120Z_\odot$, $\sim 1600Z_\odot$, or $\sim 1100Z_\odot$ if oxygen, silicon or iron nuclei are responsible for the high energy anisotropy. This result does not depend on the spectral index, or on the details of the injection spectrum, as long as the latter is shaped by rigidity. When combined, these bounds on the distance and metallicity bring in quite stringent constraints on the source of these particles. Additionally, these constraints imply that if the heavy nuclei at GZK energies are silicon or iron, the proton fraction in the all-sky composition at ankle energies should be less than $\sim 50\%$, in potential conflict with measured data.

Particle Acceleration in Relativistic Turbulent Gradual-shear Jets

As is discussed in Chapter. 1, the shear acceleration is more efficient in accelerating higher energy particles, so it may be a promising sources of UHECRs. However, this mechanism is much less studied when compared to shock acceleration or stochastic acceleration. Jets are observed in various astrophysical environments, spanning a wide range from stellar-size scale with ultra-relativistic bulk velocity (such as jets of GRBs) to Mpc scale with weakly-relativistic bulk velocity (such as jets of radio galaxies). When jets interact with their ambient medium, the boundary part could be significantly decelerated while the central part are less affected and maintain relatively high bulk velocities. So a longitudinal shear structure can naturally occur across a jet. Besides, jets may have a rotation velocity component with respect to the propagation axis, arising from the Keplerian motion of the accretion disks where they are launched. In this chapter, we will look into the shear acceleration mechanism in the context of relativistic shearing jets.

4.1 A Brief History of Study on Shear Acceleration

It has been proposed that charged particles can be accelerated in shearing flows since 1980s. Charged particles can be scattered off magnetic field inhomogeneities embedded in shearing flows and covert kinetic energy of the background flows to their non-thermal energies. Thus the shear acceleration is also known as viscous acceleration. In the pioneering work of Berezhko and his collaborators (Berezhko 1981; Berezhko & Krymskii 1981; Berezhko 1982), particle acceleration in a non-relativistic gradual-shear flow of collisionless plasma were considered, and steady-state particle distribution in momentum space was stud-

ied based on non-relativistic Boltzmann equation. Earl et al. (1988) performed an independent study on the same process by expanding Boltzmann equation to the lowest order of the ratio of flow speed to random particle speed and obtaining Parker equation with additional cosmic ray viscosity term and inertial drift term. Jokipii et al. (1989) adopted the same method and extended the study to a non-relativistic flow with a discontinuous or non-gradual shear. Furthermore, they performed an alternative method, the so-called "microscopic analysis", on particle transport in such a flow instead of the traditional method of solving Boltzmann equation (Jokipii & Morfill 1990). They assumed mean free path of particles independent on their energies, and obtained average momentum change and dispersion of particles in one mean free path. Webb (1989) followed the work of Earl et al. (1988) and successfully applied it on a relativistic shearing flow. Ostrowski (1990) studied the spectrum shape of accelerated particles in a relativistic non-gradual shear flow in detail by Monte-Carlo simulation and further proposed (Ostrowski 1998; Ostrowski 2000) a (ultra)relativistic shear flow as a potential source of ultra-high energy cosmic ray protons. Rieger & Duffy (2004) discussed particle acceleration in relativistic jets with three different types of shears: a longitude gradual shear, a longitude non-gradual shear and a transversal gradual shear. Also, they specified shear acceleration timescale in realistic astrophysical jets and indicated conditions of efficient particle acceleration. In the work of Rieger & Duffy (2006), the authors followed the microscopic analysis method used by Jokipii & Morfill (1990) and extend it to a more general case with an energy-dependent particle mean free path in a non-relativistic gradual shear flow.

As shown in previous works, efficiency of shear acceleration is closely related to how strong the velocity shear is, and hence it may be a rather efficient mechanism for particle acceleration in relativistic jets (Ostrowski 1990, Webb 1990, Rieger & Duffy 2004). The main purpose of this chapter is to study in detail the shear acceleration process in relativistic jets, including both a weakly-relativistic gradual shearing jet and an ultra-relativistic gradual shearing jet. To make the underlying physical picture more transparent, we will utilize the microscopic analysis method to derive Fokker-Planck coefficients, based on which we can numerically solve the time-dependent evolution of accelerated particles. Synchrotron emission from accelerated particles and possible application will also be discussed in the work. This chapter is organized as follows. In Section 4.2, we perform a microscopic analysis on the shear acceleration process in a symmetric

cylindrical relativistic jet of gradual shear and discuss the maximum achievable particle energy. In Section 4.3, we study time-dependent spectrum of accelerated particles and their synchrotron emissions in steady state. The effects of escape and the accompanying stochastic acceleration on the spectrum are considered. In Section 4.4, we discuss possible applications of the mechanism on producing high-energy photons and ultra-high energy cosmic rays in astrophysical jets. Finally, we give our conclusion in Section 4.5.

4.2 A Microscopic Analysis

Let's consider jet propagating along the z -axis as shown in Fig. 4.1. To simplify the analysis, we assume that the jet is cylindrical and axial-symmetric, which then can be regarded as a collection of a series of coaxial cylindrical layers of plasma flow with different radius. The velocity shear within the jet only depends on the perpendicular distance to the z -axis. So the bulk velocity of each layer can be denoted by $\beta_j(r)c$, with $r = \sqrt{(x^2 + y^2)}$ and $\beta_j(r)$ being the velocity of the layer at r in units of the light speed c . Now imagine a charged particle (e.g., electron or proton) at (x, y, z) with momentum $p = \gamma\beta mc$ is moving towards a certain direction, where γ and βc are the Lorentz factor and velocity of the particle respectively. Denote the angle between the particle's velocity and the z -axis by θ , the angle between the projection of the particle's velocity on xy -plane and x -axis by ϕ , we can write the velocity components in xyz directions as $\beta_x = \beta \sin\theta \cos\phi$, $\beta_y = \beta \sin\theta \sin\phi$ and $\beta_z = \beta \cos\theta$ respectively. By assuming that the particle propagates straightly within one mean free path or between two scatterings, the particle will move to $(x+\Delta x, y+\Delta y, z+\Delta z)$ during one scattering time $\tau(p) \equiv \Lambda(p)/\beta c$, where $\Lambda(p)$ is the mean free path of the particle with momentum p and

$$\begin{cases} \Delta x = \beta_x c \tau(p) \\ \Delta y = \beta_y c \tau(p) \\ \Delta z = \beta_z c \tau(p). \end{cases} \quad (4.1)$$

Then we can find that the transversal distance that the particle crosses, which determines the relative velocity between the two layers, can be given by

$$\Delta r = \sqrt{(r \cos\alpha + \Delta x)^2 + (r \sin\alpha + \Delta y)^2} - r \quad (4.2)$$

where $\alpha = \tan^{-1}(y/x)$. Substituting Eq.(4.1) into Eq.(4.2) and we get

$$\Delta r = (r^2 + 2\beta c r \tau(p) \cos(\alpha - \phi) + \beta^2 c^2 \sin^2(\theta) \tau(p)^2)^{1/2} - r. \quad (4.3)$$

Denoting the velocity of the layer at radius $r + \Delta r$ by β'_j , the relative velocity and Lorentz factor of the layer at radius $r + \Delta r$ with respect to that of the layer at radius r can be given by $\beta_\Delta = \frac{\beta'_j - \beta_j}{1 - \beta_j \beta'_j}$ and $\Gamma_\Delta = (1 - \beta_\Delta^2)^{-1/2}$, respectively. Once we know the shear profile of the jet and Δr , we can obtain the velocity or Lorentz factor of the particle in the rest frame of the new layer by

$$\gamma' = \Gamma_\Delta \gamma (1 - \beta \beta_\Delta \cos \theta). \quad (4.4)$$

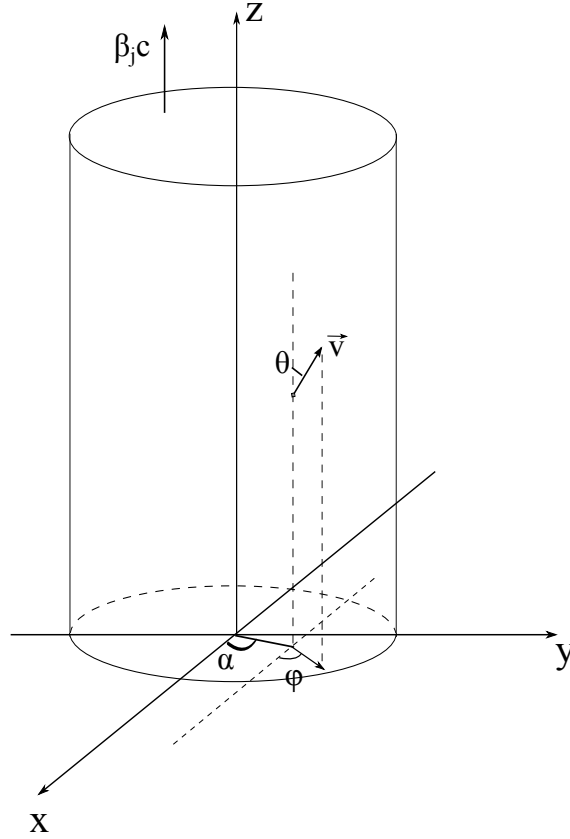


Figure 4.1: A sketch of the geometry. The jet propagates along the z -axis with a velocity profile as a function of distance from the propagation axis. The angle between the z -axis and particle's velocity is θ while the angle between the x -axis and the projection of particle's velocity on the xy -plane is ϕ .

Here, we assume a homogeneous and isotropic distribution of particles in both the real space and the momentum space. Also, the diffusion of particles are assumed to be isotropic. So we can average over ϕ , θ and α to get a mean energy increase in one scattering. From Eq.(4.3) one can find that for any given ϕ we can always redefine $\alpha = \alpha - \phi$ so that as long as we take averages of both α and ϕ from 0 to 2π , the result will not change. Thus we fix $\phi = 0$ hereafter for

simplicity. However, Eq.(4.4) is still not able to be solved analytically. Although we will carry out a numerical calculation later, an analytic expression would be helpful to understand how each parameter effect the acceleration process. So we will try to get some asymptotic solutions for limiting cases in the following.

4.2.1 Non-relativistic Gradual Shear

In this case, the relative velocity between two layers is non-relativistic. This could be a common case for not very energetic particles in weakly-relativistic large-scale jets (e.g., jets of radio galaxies). The mean free path of a charged particle can be given by

$$\Lambda \simeq r_g \frac{B_0^2/8\pi}{kI(k)} \sim \xi^{-1} r_g \left(\frac{r_g}{\lambda_{\max}} \right)^{1-q}, \quad (4.5)$$

where B_0 is the strength of the regular magnetic field in the jet and $I(k, q)$ is the energy density of MHD turbulent waves, which are also regarded as magnetic field inhomogeneities, in per unit wavenumber k . λ_{\max} is the longest wavelength of the turbulent waves. The differential energy spectrum of the turbulence is assumed to be a power law of index $-q$, say, $I(k) \propto k^{-q}$. $\xi \equiv \frac{kI(k)}{(B_0^2/8\pi)}$ is defined as the energy density ratio between turbulent magnetic fields and the regular magnetic field. $r_g = 1.7 \times 10^{16} \text{ cm}(\gamma/10^8)(B_0/10\mu\text{G})^{-1}$ is the Larmor radius of the particle. In the non-relativistic shear case, we can expect $|\Gamma_j^2 \Delta\beta_j| \ll 1$, so

$$\beta_\Delta = \frac{\beta'_j - \beta_j}{1 - \beta'_j \beta_j} = \frac{\Gamma_j^2 \Delta\beta_j}{1 - \Gamma_j^2 \Delta\beta_j \beta_j} \simeq \Gamma_j^2 \Delta\beta_j (1 + \Gamma_j^2 \Delta\beta_j \beta_j) \quad (4.6)$$

and

$$\Gamma_\Delta = \frac{1}{\sqrt{1 - \beta_\Delta^2}} \simeq 1 + \frac{1}{2} \beta_\Delta^2 \quad (4.7)$$

In the above two equations, $\Delta\beta_j \equiv \beta'_j - \beta_j \simeq \frac{\partial\beta_j}{\partial r} \Delta r$. Given $\Delta r \ll r$, Eq.(4.2) can be reduced to $\Delta r = \Delta x \cos\alpha$ in the first order. Thus Eq.(4.4) can be written into

$$\gamma' = \gamma \left(1 + \frac{1}{2} \beta_\Delta^2 - \beta \beta_\Delta \cos\theta \right) \quad (4.8)$$

when keeping the expression to the second order in β_Δ . Substituting Eq. (4.6) and (4.7) into above equations we obtain

$$\gamma' = \gamma \left(1 + \frac{1}{2} A^2 \beta^2 \tau^2 \sin^2 \theta \cos^2 \alpha - A \beta^2 \tau \sin \theta \cos \theta \cos \alpha - A^2 \beta_j \beta^3 \tau \sin^2 \theta \cos \theta \cos^2 \alpha \right) \quad (4.9)$$

where $A \equiv \Gamma_j^2 \left(\frac{\partial \beta_j}{\partial r} \right) c$ only depends on the shear profile of the jet. Fokker-Planck coefficients which describes the average rate of systematic energy change and energy dispersion of a group of particles then can be calculated by

$$\left\langle \frac{\Delta \gamma}{\Delta t} \right\rangle \equiv \frac{2 \langle \gamma' - \gamma \rangle}{\tau} = \int \int \int (\gamma' - \gamma) \sin \theta d\theta d\phi d\alpha / (8\pi^2 \tau) = \frac{1}{3} A^2 \gamma \beta^2 \tau \quad (4.10)$$

and

$$\left\langle \frac{\Delta \gamma^2}{\Delta t} \right\rangle \equiv \frac{2 \langle (\gamma' - \gamma)^2 \rangle}{\tau} = \int \int \int (\gamma' - \gamma)^2 \sin \theta d\theta d\phi d\alpha / (8\pi^2 \tau) = \frac{2}{15} A^2 \gamma^2 \beta^4 \tau \quad (4.11)$$

As $\beta \rightarrow 1$ for relativistic particle, we can expect the shear acceleration timescale

$$t_{\text{acc, shear}} = \frac{\gamma}{\langle \Delta \gamma / \Delta t \rangle} \propto \Gamma_j^{-4} \left(\frac{\partial \beta_j}{\partial r} \right)^{-2} \gamma^{q-2} B^{2-q} \lambda_{\text{max}}^{1-q} \quad (4.12)$$

For high energy particles, $\Delta r \gg r$ could happen so we have $\Delta r \simeq \Delta x$. The dependence on α in the expression of Δr can be dropped. As long as $\Gamma_j^2 \Delta \beta_j \ll 1$ still holds, we will obtain $\langle \Delta \gamma / \Delta t \rangle = \frac{2}{3} A^2 \gamma \beta^2 \tau$, which is two times the obtained result in Eq. (4.10). Here the momentum or energy of the particle is not converted back to the original frame as that in the shock and stochastic acceleration case because, given a continuous change in background flow velocity, a randomly moving particle can hardly travel back to some positions with the background velocity the same with its original position. So what we are concerned with is the momentum of the particle in the frame of the new position, based on which we can calculate energy change of the particle when it gets isotropized at another position.

One may already notice that the factor in the $\langle \Delta \gamma / \Delta t \rangle$ is different from that shown in Chapter 1. This is because here we calculate the energy increase based on Lorentz transformation while in the Chapter 1, the calculation is based on vector operation. To better illustrate, we here re-derive Eq. (1.42) and (1.43) with Lorentz transformation to compare with the derivation in Chapter 1. The denotations are the same with those in Chapter 1.

Let us calculate the momentum of the particle in the rest frame of the new position p' by a Lorentz transformation given momentum is a four-vector, say

$$p'_z = \Gamma(p_z - \beta \gamma m_0 c) = \Gamma p (\cos \theta - \frac{\delta u}{v}) \quad (4.13)$$

$$p'_y = p_y = p \cos \theta \sin \phi \quad (4.14)$$

$$p'_x = p_x = p \cos \theta \cos \phi \quad (4.15)$$

where $\beta = \delta u/c$ is velocity difference between the two layers in unit of light speed c and $\Gamma = 1/\sqrt{1-\beta^2}$.

$$p' = p \left[1 + \frac{\delta u^2}{v^2} - \frac{2\delta u}{v} \cos\theta + \frac{\delta u^2}{c^2} \cos^2\theta \right]^{1/2} \quad (4.16)$$

We can see that, in the above equation, there is one more term of the second order of $\delta u/c$. which will lead to difference in $\langle \frac{\Delta p}{\Delta t} \rangle$ while does not effect $\langle \frac{\Delta p^2}{\Delta t} \rangle$. Expanding the above equation to the second order of $\delta u/v$ and $\delta u/c$, we have

$$p' = p \left(1 + \frac{1}{2} \frac{\delta u^2}{v^2} \sin^2\theta - \frac{\delta u}{v} \cos\theta + \frac{1}{2} \frac{\delta u^2}{c^2} \cos^2\theta \right) \quad (4.17)$$

Substituting the expression of δu into the above equation, we obtain

$$\Delta p = \frac{1}{2} \left(\frac{\partial u}{\partial x} \right)^2 \tau^2 \sin^4\theta \cos^2\phi - \frac{\partial u}{\partial x} \tau \sin\theta \cos\theta \cos\phi + \frac{1}{2} \left(\frac{\partial u}{\partial x} \right)^2 \tau^2 \left(\frac{v}{c} \right)^2 \cos^2\theta \sin^2\theta \cos^2\phi \quad (4.18)$$

Averaging over the solid angle, we have

$$\left\langle \frac{\Delta p}{\Delta t} \right\rangle = \frac{4}{15} \left(\frac{\partial u(x)}{\partial x} \right)^2 p \tau + \frac{1}{15} \left(\frac{\partial u(x)}{\partial x} \right)^2 \left(\frac{v}{c} \right)^2 p \tau \quad (4.19)$$

and

$$\left\langle \frac{\Delta p^2}{\Delta t} \right\rangle = \frac{2}{15} \left[\frac{\partial u(x)}{\partial x} \right]^2 p^2 \tau \quad (4.20)$$

The first term in the right-hand side of Eq. 4.19 is the same as that Eq. (1.51) except that is 2 times larger which is due to definition. The second term comes from the additional second order term of $\delta u/c$. Note that $v/c \rightarrow 1$ if particle is relativistic, and if the flow is also relativistic, $\delta u \rightarrow \Gamma^2 \delta u$. Then we arrive at

$$\left\langle \frac{\Delta p}{\Delta t} \right\rangle = \frac{1}{3} \Gamma^4 \left[\frac{\partial u(x)}{\partial x} \right]^2 p \tau \quad (4.21)$$

which is the same with the Eq. (4.10).

An interesting feature is that, in contrast to the shock acceleration and stochastic acceleration, the shear acceleration timescale in non-relativistic gradual shear case is inversely proportional to the energy of the particle for $q < 2$, i.e., the more energetic the particle is, the more energy it will gain in unit time. This is conducive to the acceleration of high energy particles. To determine the maximum achievable energy under the shear acceleration, some mechanisms that may stop the acceleration such as cooling and escape should be considered. The

synchrotron cooling timescale of charged particles can be given by $t_{\text{syn}} = \frac{9m^3 c^5}{4e^4 \gamma \beta^2 B^2}$.

Let $t_{\text{acc, shear}} = t_{\text{syn}}$, we get

$$\gamma_{\text{max}} = \left[\frac{3}{4} \Gamma_j^4 \left(\frac{\beta_{j,0}}{\Delta L} \right)^2 \xi^{-1} (mc^2)^{5-q} e^{q-6} B^{q-4} \lambda_{\text{max}}^{q-1} \right]^{1/(q-1)} \quad (4.22)$$

The value depends on the parameter q or the shape of the spectrum of turbulence. To find out a detailed value of γ_{max} , we look into three cases, the Bohm limit with $q = 1$, Komogorov turbulence with $q = 5/3$ and so-called hard-sphere approximation with $q = 2$, respectively, and obtain

$$\gamma_{\text{max}} = \begin{cases} \infty, & q = 1, \\ 6.0 \times 10^8 \Gamma_j^6 \beta_{j,0}^3 \left(\frac{\xi}{0.1} \right)^{-3/2} \left(\frac{B}{3\mu\text{G}} \right)^{-7/2} \left(\frac{\lambda_{\text{max}}}{10^{18}\text{cm}} \right) \left(\frac{\Delta L}{10^{20}\text{cm}} \right)^{-3}, & q = 5/3, \\ 8.6 \times 10^8 \Gamma_j^4 \beta_{j,0}^2 \left(\frac{\xi}{0.1} \right)^{-1} \left(\frac{B}{3\mu\text{G}} \right)^{-2} \left(\frac{\lambda_{\text{max}}}{10^{18}\text{cm}} \right) \left(\frac{\Delta L}{10^{20}\text{cm}} \right)^{-2}, & q = 2. \end{cases} \quad (4.23)$$

We should note that in the case of $q = 1$, the dependence of the acceleration timescale on particle's energy is the same with that of synchrotron cooling timescale, so in this case either there is no acceleration at all or the synchrotron cooling can not stop acceleration at any energy. The latter case will occur if

$$A^2 = \Gamma_j^4 \left(\frac{\beta_{j,0}}{\Delta L} \right)^2 c^2 > \frac{3e^5 \xi B^3}{3m^4 c^6} \quad (4.24)$$

On the other hand, particles are randomly scattered by turbulent waves inside the jet. So their propagations can be regarded as diffusion process and they have chances to escape the acceleration region. The diffusion escape time scale can be given by $t_{\text{esc}} = r_j^2 / \kappa \propto \gamma^{q-2}$ where $\kappa = c\Lambda/3$ is the spatial diffusion coefficient. Note that, the energy dependence of t_{esc} on γ is the same with $t_{\text{acc, sh}}$. So diffusive escape may never stop acceleration, or stop acceleration from the beginning. To make sure an efficient acceleration, we require $t_{\text{acc, sh}} < t_{\text{esc}}$ which is equivalent to

$$\Gamma_j^4 \left(\frac{\beta_{j,0}}{\Delta L} \right)^2 r_j^2 > 1 \quad (4.25)$$

For mildly-relativistic and non-relativistic jet, $\Gamma_j^4 \beta_{j,0}^2 < 1$ is generally established, so we require $\Delta L < r_j$. A spine/sheath structure of jet whose inner part keep a relative higher bulk velocity surrounded by a slower shearing boundary layer can satisfy the above requirement.

We need to point out that there exists at least two additional mechanisms, besides the Hillas condition, that can stop acceleration so that the maximum

achievable energy of particles will not be unlimited even if conditions Eq. (4.24) and (4.25) are satisfied. First, as particles become more and more energetic, their mean free paths will eventually become comparable to the size of the acceleration region so their propagation mode will also change gradually from a diffusive way to a rectilinear way. Thus, these high energy particles can escape the region within only a few mean free path. This is similar to the Hillas condition for the maximum energy. The other constraint is from wave-particle interaction. The scattering center is believed to be MHD wave so to scatter off these centers is to interact with the MHD waves. Particles can only interact efficiently with the wave whose wavelength is close to its Larmor radius, so a particle with Larmor radius larger than λ_{\max} will not be scattered efficiently. For electron acceleration, cooling is efficient and hence usually determines the maximum energy. But for proton acceleration, the later two mechanisms may become the most restrictive constraints on the maximum energy.

4.2.2 Relativistic Gradual Shear

If we consider the acceleration in a small-scale ultra-relativistic jet, the velocity shear could be so strong that the relative velocity between the two layers where particles locate before and after one mean free path would become relativistic. This is particularly possible for very energetic particles, which has large mean free paths, at the inner region of a relativistic jet. So the condition $\Gamma_j^2 \Delta\beta_j \ll 1$ may probably not hold anymore in this case and hence Eq. (4.10) and (4.11) fail to depict energy gain process of particles.

Considering a very energetic particle crosses a large distance $r \ll |\Delta r| \simeq \Delta x < r_{\max}$ in one mean free path, it will always move from a small radius layer to a larger radius layer (i.e., $\beta_j > \beta'_j$), so

$$\begin{aligned} \beta_\Delta &= \frac{\Gamma_j^2 \Delta\beta_j}{1 - \Gamma_j^2 \Delta\beta_j \beta_j} \rightarrow -1 \\ \Gamma_\Delta &\simeq 1 / \sqrt{1 - \left(\frac{\Gamma_j^2 \Delta\beta_j}{1 - \Gamma_j^2 \Delta\beta_j \beta_j} \right)^2} \simeq \sqrt{-\frac{\Gamma_j^2 \Delta\beta_j}{2}}. \end{aligned} \quad (4.26)$$

According to Eq. (4.4), we obtain

$$\gamma' = \frac{1}{\sqrt{2}} (-A\tau)^{1/2} \gamma \beta^{1/2} (1 + \beta \cos\theta) (\sin\theta)^{1/2} \quad (4.27)$$

in the case $\Delta\beta_j < 0$. After averaging θ from 0 to π and α from $-\pi/2$ to $\pi/2$, we obtain the average acceleration rate of particles

$$\left\langle \frac{\Delta\gamma}{\Delta t} \right\rangle \simeq 1.24 (-A)^{1/2} \gamma \beta^{1/2} \tau^{-1/2}. \quad (4.28)$$

The acceleration timescale is

$$t_{\text{acc, shear}} = \frac{\gamma}{\langle \Delta\gamma/\Delta t \rangle} \propto \Gamma_j^{-1} \left| \frac{\partial\beta_j}{\partial r} \right|^{-1/2} \gamma^{1-q/2} B^{q/2-1} \lambda_{\text{max}}^{(q-1)/2}. \quad (4.29)$$

Note that it is different from the non-relativistic shear case in which the acceleration timescale increases with the energy of particles for $q < 2$. The maximum energy constrained by synchrotron cooling is found to be

$$\gamma_{\text{max}} = \left[2.8\Gamma_j \left(\frac{\beta_{j,0}}{\Delta L} \right)^{1/2} \xi^{1/2} (mc)^{2+q/2} e^{-3-q/2} B^{-1-q/2} \lambda_{\text{max}}^{(1-q)/2} \right]^{2/(4-q)} \quad (4.30)$$

and

$$\gamma_{\text{max}} = \begin{cases} 1.7 \times 10^8 \left(\frac{\Gamma_j}{10} \right)^{2/3} \left(\frac{\xi}{0.1} \right)^{1/3} \left(\frac{B}{1\text{G}} \right)^{-1} \left(\frac{\Delta L}{10^{12}\text{cm}} \right)^{-2/3}, & q = 1 \\ 2.3 \times 10^8 \left(\frac{\Gamma_j}{10} \right)^{6/7} \left(\frac{\xi}{0.1} \right)^{3/7} \left(\frac{B}{1\text{G}} \right)^{-11/7} \left(\frac{\lambda_{\text{max}}}{10^{11}\text{cm}} \right)^{-2/7} \left(\frac{\Delta L}{10^{12}\text{cm}} \right)^{-3/7}, & q = 5/3 \\ 2.9 \times 10^8 \frac{\Gamma_j}{10} \left(\frac{\xi}{0.1} \right)^{1/2} \left(\frac{B}{1\text{G}} \right)^{-2} \left(\frac{\lambda_{\text{max}}}{10^{11}\text{cm}} \right)^{-1/2} \left(\frac{\Delta L}{10^{12}\text{cm}} \right)^{-1/2}, & q = 2 \end{cases} \quad (4.31)$$

On the other hand, when requiring diffusive escape not to stop acceleration ($t_{\text{esc}} > t_{\text{acc, shear}}$) we have $3.7r_j^2 > \lambda^{3/2}\Delta L^{1/2}$. Given that $\Delta L \leq r_j$, this requirement is reduced to $\lambda \lesssim r_j$, which will be naturally satisfied as long as the Hillas condition and the wave-particle interaction condition are satisfied. More specifically, the former condition requires $r_g < \lambda_{\text{max}}$ which gives $\gamma_{\text{max}} = \Delta L e B / mc = 5.8 \times 10^7 (\lambda_{\text{max}} / 10^{11}\text{cm})(B/1\text{G})$, while the latter one requires $\lambda < \Delta L$, which gives $\gamma_{\text{max}} = 5.8 \times 10^7 (\xi/0.1)(\Delta L/10^{12}\text{cm})(B/1\text{G})$ in $q = 1$ case, and gives, in $q = 5/3$ case, $\gamma_{\text{max}} = 5.8 \times 10^7 (\xi/0.1)^3 (\Delta L/10^{12}\text{cm})^3 (\lambda_{\text{max}}/10^{11}\text{cm})^{-2} (B/1\text{G})$. $\lambda = \Delta L$ can not give constraints on γ_{max} in the case of $q = 2$ because λ is independent on the particle energy.

One thing worth noting is that in an ultra-relativistic shearing jet, particles can hardly reach the maximum energy obtained above. A particle travels among different positions in the jet when it is being accelerated. The acceleration rate is proportional to the bulk Lorentz factor of the background flow. Given a linear shear profile, only the inner most region, which only occupies a small fraction of the total volume of the jet, can have a high bulk Lorentz factor, while Lorentz factors of the flow decrease rapidly to a few in outer part of the jet. So in most part of the jet the shear will become non-relativistic so we need to use Eq. (4.10) instead of Eq. (4.28) to calculate the acceleration rate at large radii, which is much slower. The maximum energy obtained above can only be regarded as an upper limit. Also, as one may already notice that, we do not get the momentum diffusion coefficients in relativistic shear case. That's because in this case the

energy change per scattering is so large that we can not regard the process as a diffusion. We will have some more discussion on this effect in next section.

Fig. 4.2 shows the numerical result of average shear acceleration rate of electrons v.s. their energies or Lorentz factors. The upper panel shows the result of $\langle \Delta\gamma/\Delta t \rangle$ at $r = 10^{16}$ cm in a large scale non-relativistic flow with a jet radius of 10^{20} cm and bulk Lorentz factor of $\Gamma_{j,0} = 1.1$ at the center part of the jet. The velocity of the jet decreases linearly with the distance to propagation axis from $\beta_{j,0} = \sqrt{1 - 1/\Gamma_{j,0}^2}$ at $r = 0$ to $\beta_j = 0$ at $r = r_j$ (i.e., $\Delta r = r_j = 10^{20}$ cm). The average magnetic field is assumed to be $B = 3\mu G$, and $\xi = 0.1$, $q = 1$ and $\Lambda = 10^{18}$ cm is taken for the turbulent magnetic field. We can see that $\langle \Delta\gamma/\Delta t \rangle \propto \gamma^2$ follows Eq. (4.10) at low energies when $\Delta r \ll r$, while follows $2 \times$ Eq. (4.10) at high energies when $\Delta r \gg r$. Transitions happens where $\gamma \sim 2 \times 10^6$, corresponding to $\Delta r \sim \lambda \sim 10^{16}$ cm. The curve of $\langle \Delta\gamma/\Delta t \rangle$ becomes flat at about $\gamma = 2 \times 10^{10}$ above which the mean free path of electrons is larger than the size of the jet. The energy change is due to the transform of particle Lorentz factor from one frame of $\Gamma = \Gamma_j$ to another frame of $\Gamma = 1$, say, $\Delta\gamma/\Delta t = (\Gamma_{j,0} - 1)\gamma/\tau \propto \gamma^0$ in $q = 1$ case. But as we pointed out above, when particles move outside the jet they can probably not return, so particles with energy in such range will not get acceleration. The lower panel of Fig. 4.2 shows $\langle \Delta\gamma/\Delta t \rangle$ v.s. r at $r = 10^8$ cm in a small scale ultra-relativistic flow with a jet radius of 10^{12} cm and central bulk Lorentz factor of $\Gamma_{j,0} = 1000$. We take $B = 1G$, $\xi = 0.1$, $q = 1$, $\Lambda = 10^{11}$ cm and also assume the velocity of the jet decreases linearly to zero from $r = 0$ to $r = r_j$. The numerical solution still follows the analytical solution in non-relativistic shear case (Eq. 4.10) at low energies due to small mean free paths although the velocity of the jet changes drastically. As energies of particles go up, they can cross a larger distance in one mean free path and the velocity shear of the two layers at the beginning and the end of the mean free path becomes relativistic and hence the solution in relativistic shear case works. Again, the mean free path of electrons becomes larger than the jet size above $\gamma \sim 6 \times 10^7$ and we can see the flattening of the curve of $\langle \Delta\gamma/\Delta t \rangle$.

Fig. 4.3 presents how the value of $\langle \Delta\gamma/\Delta t \rangle$ of a electron with $\gamma = 10^6$ changes with their position in the jet. Parameters are the same with those in Fig. 4.2. The profiles of numerical solutions are basically determined by velocity profile of the jet through $A(r)^2$ and $|A(r)|^{1/2}$ in non-relativistic shear case and relativistic shear case respectively. In the upper panel, the numerical solution agrees well with analytical solutions for $\Delta r \gg r$ and $\Delta r \ll r$ at the very central region of the jet and the near the edge of the jet respectively in a weakly-relativistic jet. In the

lower panel, we can see that while the numerical curves follows the analytical solution for relativistic shear case in the inner region, the analytical solution for non-relativistic shear case works for the acceleration in the outer region of the jet. This is because given the velocity profile of $\partial\beta_j/\partial r = \text{const}$, the velocity shear in the outer region of the jet becomes non-relativistic even central part of the jet is ultra-relativistic ($\Gamma_{j,0} \gg 1$). One may notice that there are drops of the acceleration rate around $r \simeq 10^{15.5}\text{cm}$ in the weakly-relativistic jet (upper panel) and around $r = 10^{10}\text{cm}$ in the ultra-relativistic jet (lower panel) respectively. The drops happen when the radii of the positions are comparable to the mean free paths of $\gamma = 10^6$ electron respectively in the two cases, so electrons moving toward certain directions may propagate to a new layer with a similar radius to the original one after one mean free path. Since the shear profile of the jet only depends on r , little change in radius means little shear and hence leads to an inefficient acceleration.

4.3 Accelerated Particle Spectrum

Particle distribution in momentum space $f(p, t)$ and its evolution including diffusive escape is governed by a Fokker-Planck-type equation

$$\frac{\partial f(p, t)}{\partial t} = \frac{1}{2p^2} \frac{\partial^2}{\partial p^2} \left[p^2 \left\langle \frac{\Delta p^2}{\Delta t} \right\rangle f(p, t) \right] - \frac{1}{p^2} \frac{\partial}{\partial p} \left[p^2 \left(\left\langle \frac{\Delta p}{\Delta t} \right\rangle + \langle \dot{p}_c \rangle \right) f(p, t) \right] - \frac{f(p, t)}{t_{\text{esc}}(p)} + q(p, t) \quad (4.32)$$

The first term in the right-hand side calculates the diffusion in momentum space. The second term accounts for the systematic energy change of particles, including particle acceleration and cooling which is denoted by $\langle \dot{p}_c \rangle$. The third term considers the diffusive escape of particles from the accelerated region by assuming all the particles have finite escape possibilities which do not depend on their positions in the acceleration region. $q(p, t)$ is the particle injection term which is usually considered to be a δ -function in energy but continuous in time, i.e., $q = \delta(p - p_0)$ with p_0 the injection momentum, and we will approximate this term as a narrow Gaussian function in our numerical calculation. Given that $p \simeq \gamma mc$ and $n(\gamma, t)d\gamma = 4\pi p^2 f(p, t)dp$ which is the differential particle number density, Lorentz factor (energy) distribution can be obtained as

$$\frac{\partial n(\gamma, t)}{\partial t} = \frac{1}{2} \frac{\partial}{\partial \gamma} \left[\left\langle \frac{\Delta \gamma^2}{\Delta t} \right\rangle \frac{\partial n(\gamma, t)}{\partial \gamma} \right] - \frac{\partial}{\partial \gamma} \left[\left(\left\langle \frac{\Delta \gamma}{\Delta t} \right\rangle - \frac{1}{2} \frac{\partial}{\partial \gamma} \left\langle \frac{\Delta \gamma^2}{\Delta t} \right\rangle + \langle \dot{\gamma}_c \rangle \right) n(\gamma, t) \right] - \frac{n}{t_{\text{esc}}} + Q(\gamma, t) \quad (4.33)$$

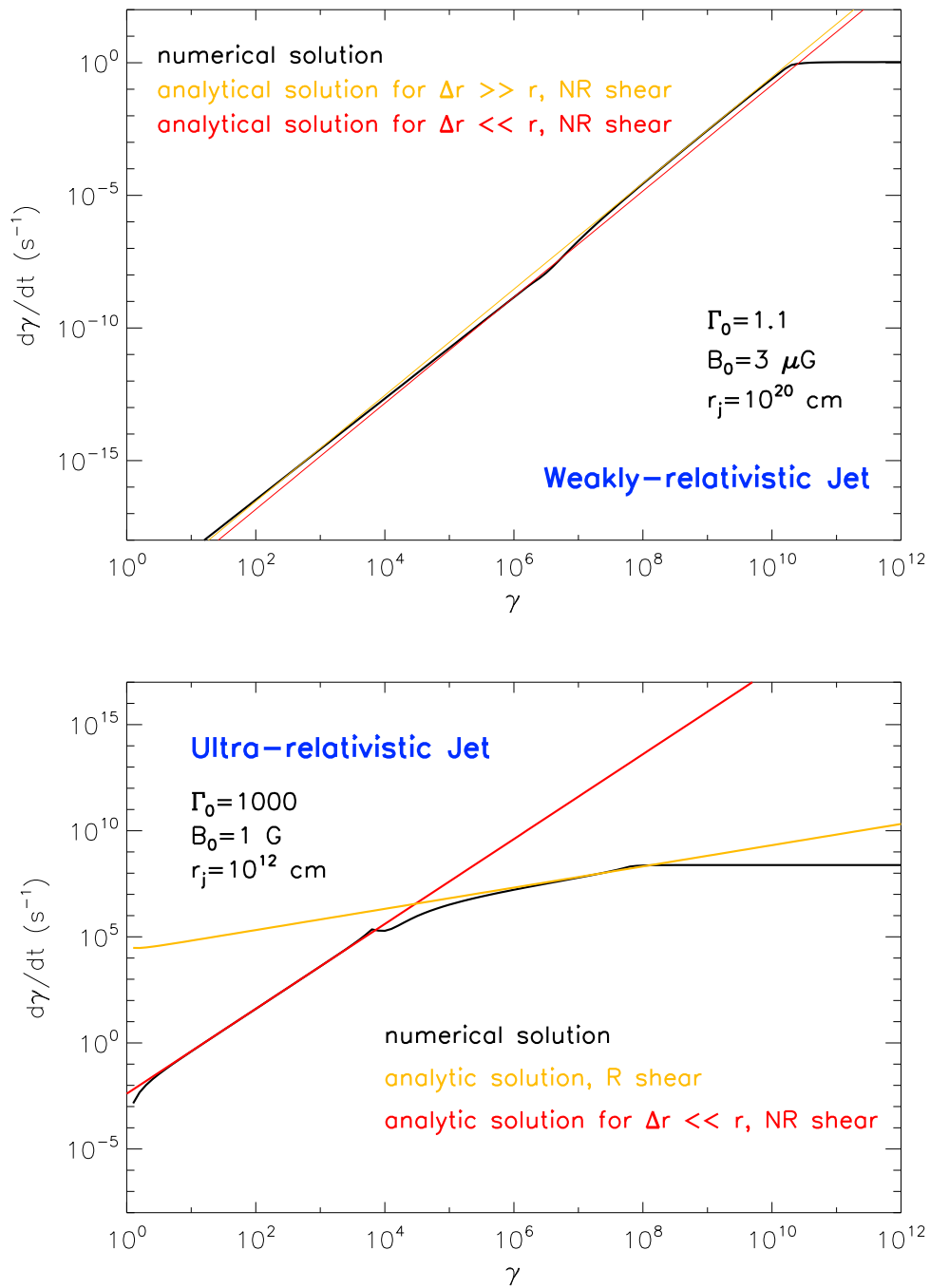


Figure 4.2: Average acceleration rate as a function of particle energy (Lorentz factor). The upper panel is for the case of a mildly-relativistic jet while the lower panel is for the case of an ultra-relativistic jet.

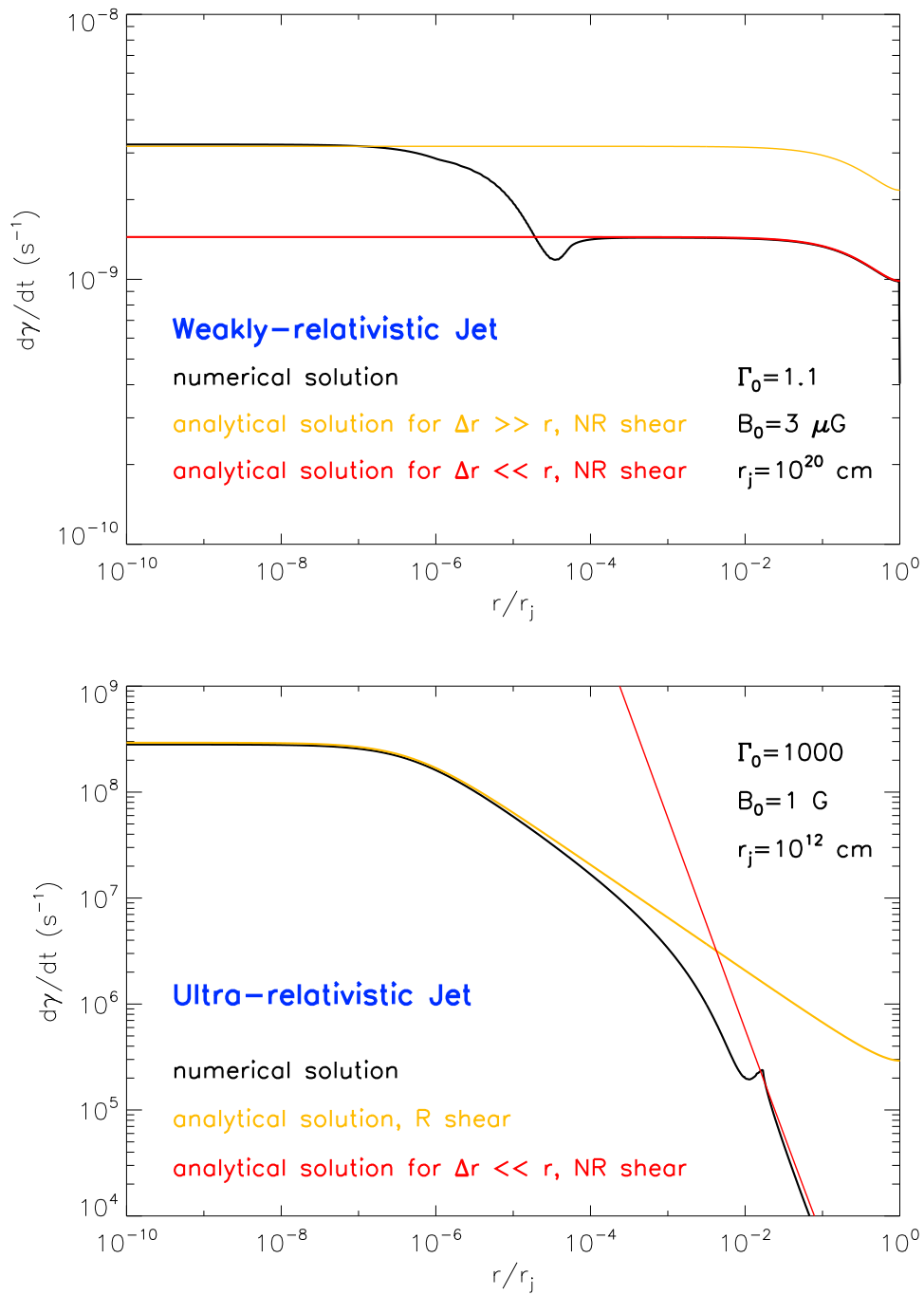


Figure 4.3: Average acceleration rate as a function of radius (vertical distance to the propagation axis). The upper panel is for the case of a mildly-relativistic jet while the lower panel is for the case of an ultra-relativistic jet.

where $Q = \text{Const.} \times \delta(\gamma - \gamma_0)$ with γ_0 the Lorentz factor of injected particles which is taken to be 100 in the calculation. The efficiency of shear acceleration strongly depends on the velocity profile of the jet, so the acceleration rate varies with the jet radius. We here aim to get a space-averaged spectrum of accelerated particles. Given that the particle spatial distribution is homogeneous and isotropic, we can obtain average Fokker-Planck coefficients by

$$\left\langle \frac{\Delta\gamma}{\Delta t} \right\rangle = \frac{\int 2\pi r \langle \frac{\Delta\gamma}{\Delta t} \rangle(r) dr}{\int 2\pi r dr} \quad (4.34)$$

$$\left\langle \frac{\Delta\gamma^2}{\Delta t} \right\rangle = \frac{\int 2\pi r \langle \frac{\Delta\gamma^2}{\Delta t} \rangle(r) dr}{\int 2\pi r dr} \quad (4.35)$$

On the other hand, particles extract kinetic energy of background flow via scattering off magnetic field inhomogeneities, while these scattering centers are essential to the stochastic acceleration. So the shear acceleration should be inevitably accompanied by stochastic acceleration. Thus, in Eq. (4.33), the Fokker-Planck coefficients, $\langle \frac{\Delta\gamma^2}{\Delta t} \rangle$ and $\langle \frac{\Delta\gamma}{\Delta t} \rangle$ should both contain two parts, say, $\langle \frac{\Delta\gamma^2}{\Delta t} \rangle = \langle \frac{\Delta\gamma^2}{\Delta t} \rangle_{\text{st}} + \langle \frac{\Delta\gamma^2}{\Delta t} \rangle_{\text{sh}}$ where $\langle \frac{\Delta\gamma^2}{\Delta t} \rangle_{\text{st}} = \frac{4\xi\Gamma_A^4\beta_A^2\gamma^2c}{3r_g^{2-q}r_{g,\text{max}}^{q-1}}$ is the diffusion coefficient of stochastic acceleration with β_A being the Alfvén speed of the plasma and $\Gamma_A = 1/\sqrt{1-\beta_A^2}$. Similarly, $\langle \frac{\Delta\gamma}{\Delta t} \rangle = \langle \frac{\Delta\gamma}{\Delta t} \rangle_{\text{st}} + \langle \frac{\Delta\gamma}{\Delta t} \rangle_{\text{sh}}$ where $\langle \frac{\Delta\gamma}{\Delta t} \rangle_{\text{st}} = \frac{8\xi\Gamma_A^2\beta_A^2\gamma c}{3r_g^{2-q}r_{g,\text{max}}^{q-1}}$.

4.3.1 In Weakly-relativistic Jets

As obtained in the previous section, the transverse size of the shear region ΔL should be smaller than the radius of the jet r_j to ensure shear acceleration faster than escape in a weakly-relativistic jet. So we assume jet velocity is constant from $r = 0$ to $r = 0.9r_j$ with velocity $\beta_{j,0}$ and decreases linearly from $0.9r_j$ to r_j , which is

$$\beta_j = \begin{cases} \beta_{j,0}, & r < 0.9r_j, \\ \beta_{j,0} - \frac{\beta_{j,0}}{\Delta L}(r - 0.9r_j), & r \geq 0.9r_j. \end{cases} \quad (4.36)$$

After using the velocity profile to get the Fokker-Planck coefficients, we can solve the particle spectrum numerically from Eq. (4.33). But before we show these results, it is useful to derive analytical solutions for steady state with some simplification, because analytical solutions not only give us a direct impression of the spectrum shape, but also can serve as a cross-check of the numerical results.

Intuitively, the spectrum should consist of three parts. At low energy, stochastic acceleration will be faster than shear acceleration and hence dominates the accelerated spectrum; shear acceleration may become more efficient at higher energy while stochastic acceleration becomes less efficient, so the former mechanism will overcome the latter one at a certain energy and shape the spectrum; at the highest energy, cooling effect as well as other mechanisms can stop the acceleration so the spectrum should change again and finally a cut-off should occur in the spectrum. Here we neglect the diffusive escape term. Given $\langle \frac{\Delta\gamma^2}{\Delta t} \rangle_{\text{st}} \propto \gamma^q$ and $\langle \frac{\Delta\gamma}{\Delta t} \rangle_{p,\text{st}} \propto \gamma^{q-1}$, we have $n(\gamma) \propto \gamma^{1-q}$ at low energy. After shear acceleration takes over at $\langle \frac{\Delta\gamma}{\Delta t} \rangle_{p,\text{st}} = \langle \frac{\Delta\gamma}{\Delta t} \rangle_{p,\text{sh}}$, the Fokker-Planck coefficients become $D_{\text{sh}} \propto \gamma^{4-q}$ and $\langle \Delta\gamma/\Delta t \rangle_{p,\text{sh}} \propto \gamma^{3-q}$, leading to $n(\gamma) \propto \gamma^{q-3}$. For electrons, acceleration is usually stopped by synchrotron cooling and this leads to a pile-up bump followed by a cut-off at the highest energy as $n(\gamma) \propto \gamma^{1+q} \exp\left[-\frac{5}{q-1} \left(\frac{\gamma}{\gamma_{\text{max}}}\right)^{q-1}\right]$. For proton acceleration, the cut-off is dependent on particle containment and wave-particle interaction, the shape of the spectrum is closely related to how the propagation mode of particles change from a diffusive way to a rectilinear way, and the behavior of the turbulence spectrum at small wave-numbers. These issues are still not well studied and also beyond the scope of this work. So we just assume an abrupt cut-off above the corresponding energies in Fokker-Planck coefficients when calculating the proton spectrum.

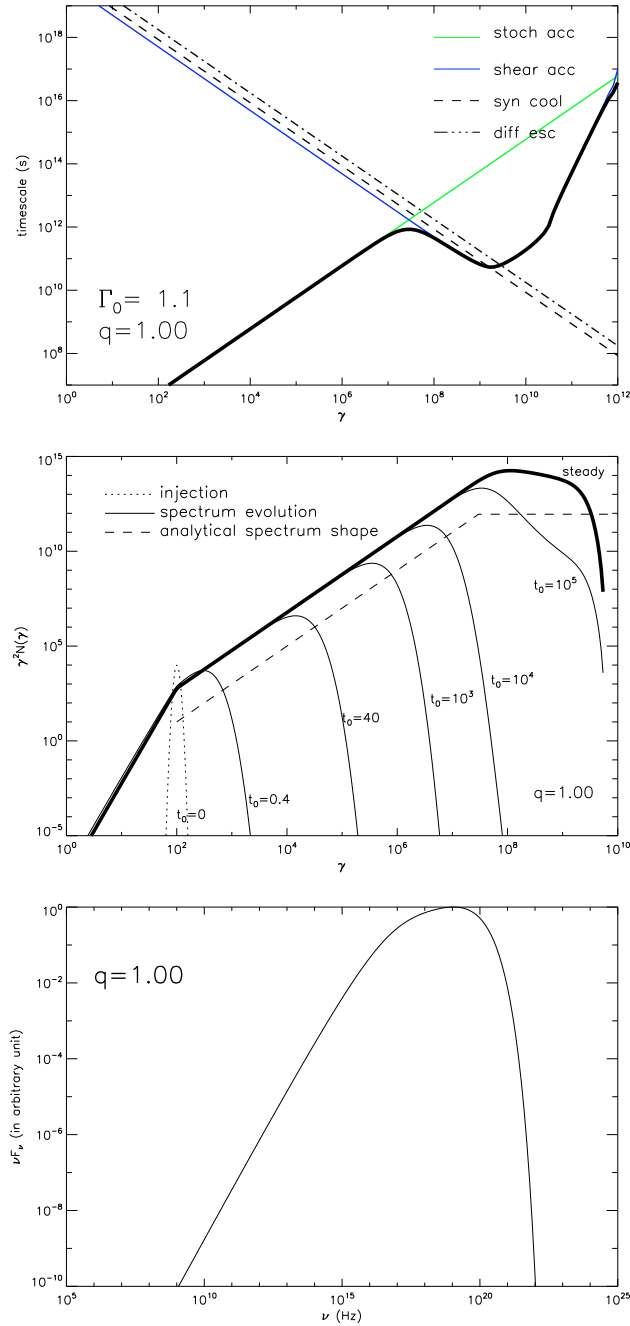


Figure 4.4: $q = 1$ case. **Top panel:** timescales for different processes. The blue and green lines show the average shear acceleration timescale and stochastic timescale. The thick black line is the real acceleration timescale under these two acceleration mechanisms. The dashed line represents synchrotron cooling timescale while the dash-dotted line represents diffusive escape timescale; **Middle panel:** evolution of electron spectrum. Thin black lines are spectrum at certain time after the injection while the thick line shows the spectrum in steady state. The dashed line exhibits the analytical solution for steady state; **Bottom panel:** synchrotron radiation of electrons in steady state. Transverse radius of jet is $r_j = 10^{20}$ cm, while the size of shearing region is $\Delta L = 10^{19}$ cm. The background magnetic field is $B_0 = 3\mu\text{G}$. The energy density ratio between turbulent magnetic field and background magnetic field is $\xi = 0.1$. The number density of protons is 10^{-4}cm^{-3} which leads to an Alfvén speed of $\beta_A \approx 0.007$.

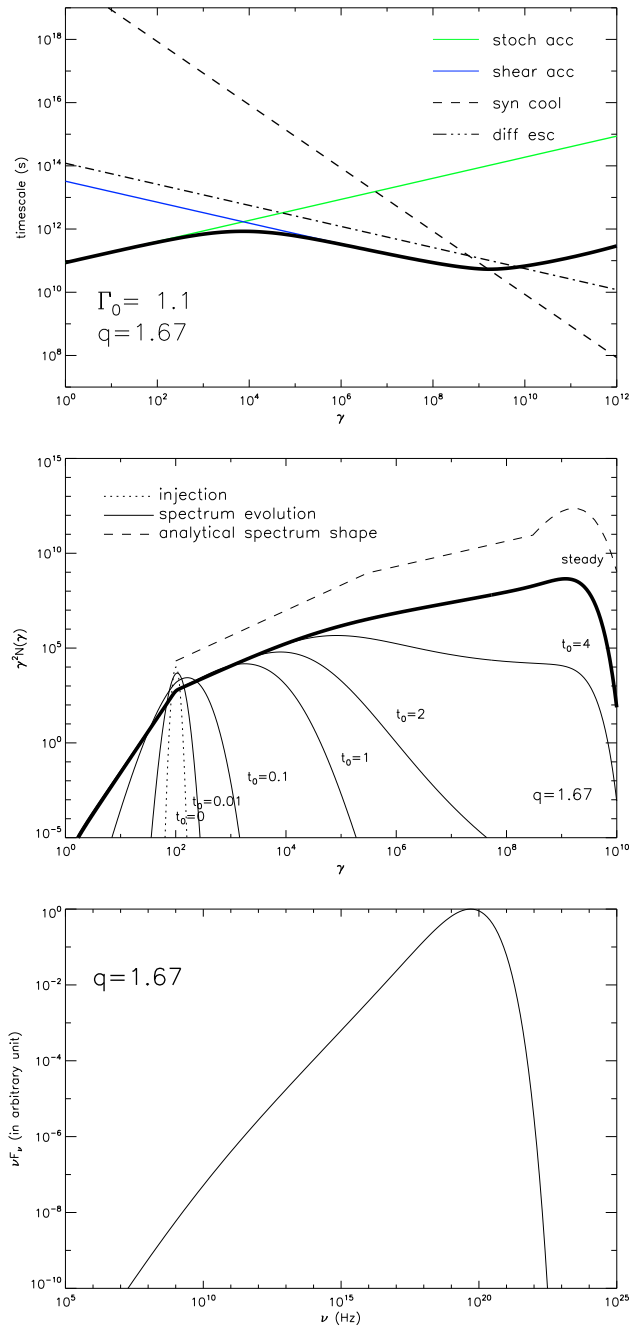


Figure 4.5: The same as Fig. 4.4 but for $q = 5/3$ case.

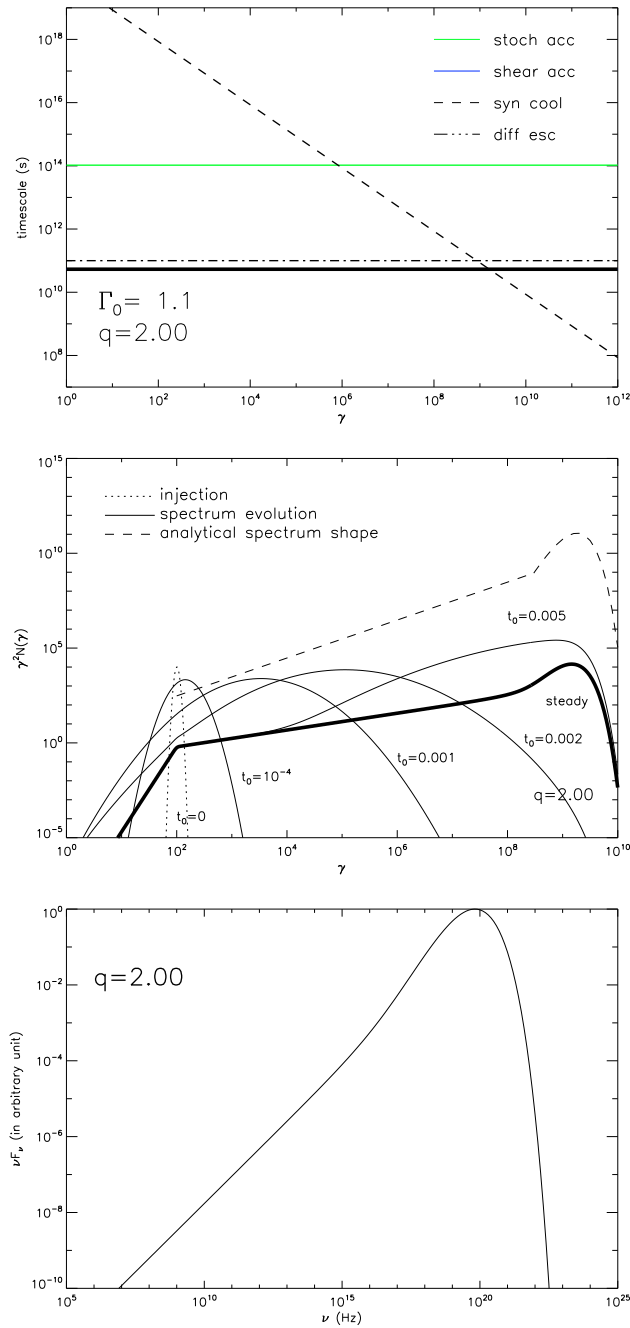


Figure 4.6: The same as Fig. 4.4 but for $q = 2$ case. In this case, the mean scattering time is independent on particle energy.

Figs. 4.4-4.6 show the timescales for different processes (top panels), the spectra of accelerated electrons (middle panels) and their synchrotron emission in the steady state (bottom panels) in the weakly-relativistic jet case for different types of turbulences. As we can see from the top panels, in $q = 1$ and $q = 5/3$

cases, stochastic acceleration plays an important role at low energies while shear acceleration dominates at high energies. The maximum energy achievable in shear acceleration is about 100 times higher than that in stochastic acceleration in the $q = 1$ case and are even higher in $q = 5/3$ and $q = 2$ case. Around $\gamma \sim 10^9$ and higher energy, the mean free path of electrons become comparable or larger than the size of the shear region, $\Delta L = 10^{19}$ cm, so some of the electrons, especially those initially moving against the jet axis, will catastrophically escape the jet. Thus the average acceleration rate is lowered down, and the acceleration timescale increase rapidly beyond $\gamma \sim 10^9$. For $q = 2$ case, as the mean free path is independent on particle energy, even at low energies some electrons can escape very quickly and the presented timescale is a little longer than that calculated by Eq. (4.12).

The middle panels exhibit the time evolution of the accelerated electron spectrum for three cases of turbulence respectively. The thick solid lines present the spectrum at steady state while thin solid lines show the spectrum at different time before reaching the steady state, in unit of t_0 where $t_0 \equiv t/t_{\text{stoch},0}$ with $t_{\text{stoch},0}$ the stochastic acceleration timescale for electrons at injection, i.e. $t_{\text{stoch},0} = p_0^2 / \langle \frac{\Delta\gamma^2}{\Delta t} \rangle_{\text{st}}(\gamma = \gamma_0)$. The dashed lines are the profiles of analytical solutions in steady state without considering escape. We can see that the shape of numerical solutions generally follow that of the analytical one, except 1) the slope of spectrum that dominated by shear acceleration are a bit softer than the analytical one which is due to diffusive escape and 2) the feature of pile-up bump is not pronounced or even vanishes, caused by catastrophic escape. To further illustrate the effect of escape, we present the spectrum evolution of electrons in $q = 5/3$ case in Fig. 4.8, in which all the parameters are the same with that in Fig. 4.5 of $q = 5/3$ case but remove the diffusive escape term n/t_{esc} in Eq. (4.33) and ignore the decrease in Fokker-Planck coefficients resulted from catastrophic escape. As we can see, the slope of spectrum at high energy is well consistent with the analytical one.

Although stochastic acceleration does not influence the high energy spectrum, it plays an important role in the whole acceleration process for $q < 2$ cases. The shear acceleration rate increases with particle energy, which, however, also implies that low energy particles are not easy to get energy via this process. In the case that the injection energy is low, the shear acceleration would become quite inefficient. Fig. 4.7 shows the evolution of electron spectrum with artificially removing the terms related to stochastic acceleration when solving Eq. (4.33),

while all the parameters are kept the same as in the middle panel of Fig. 4.5. We can see the time required to reach the steady state is about one order of magnitude longer. So stochastic acceleration serves as a pre-acceleration when the injection energy of electrons is low, and boosts the whole acceleration process (also see Rieger & Duffy 2006 for a discussion of shock-type acceleration providing energetic seed particles).

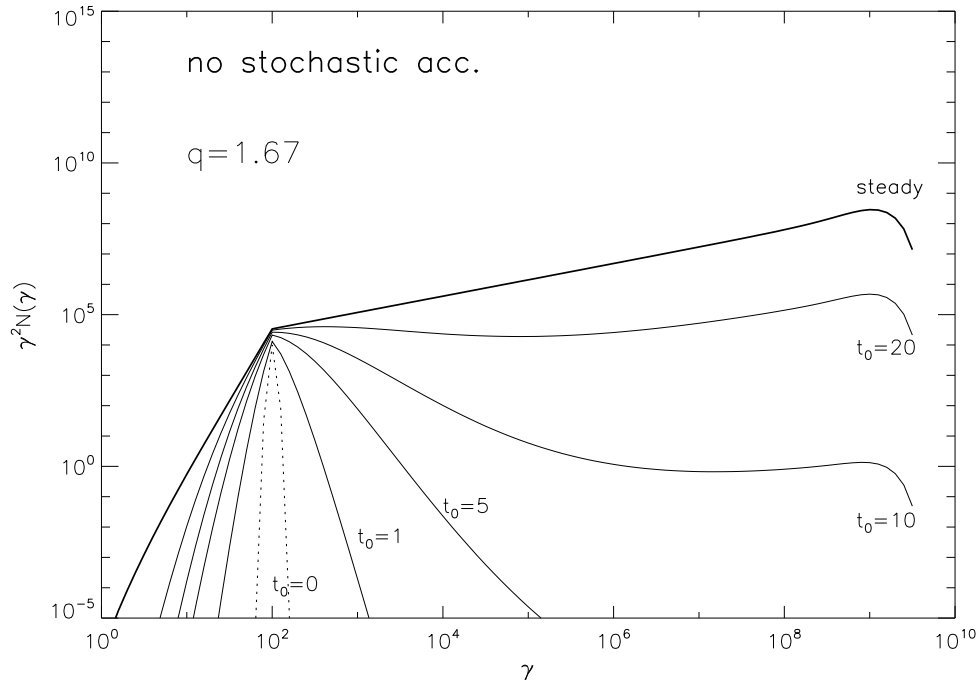


Figure 4.7: Time-dependent evolution of electron spectrum without stochastic acceleration. All parameters are same the as in the Fig. 4.5.

According to the analytical solution of electrons in steady state, we may expect that, except for $q = 1$ and $q = 2$ case, the steady-state synchrotron spectrum generally contains three segments of power-laws and a cutoff. The lowest-energy segment (probably in radio band) should be dominated by electrons subjected to stochastic acceleration with a photon index of $-q/2$. The middle-segment (probably in Optical/UV band) is produced by shear acceleration with a photon index of $-(4-q)/2$. While in the highest-energy segment (probably in X-ray band), a hardening may occur, which is due to the cooling pile up with photon index of $q/2$, coupled with an exponential-like cut-off $\exp\left(-b\nu^{\frac{q-1}{q+1}}\right)$ where b is a constant related to turbulence and cooling parameters. However, due to the effect of the escape process, the actual synchrotron spectrum would be correspondingly

softer and the hardening may not show as well. As is shown in the bottom panels of Fig. 4.4-4.6, the peak of the νf_ν spectrum can be as high as $10^{19} - 10^{20}$ Hz and power indices of different band spectrum can be different. In the lower panel of Fig. 4.8, we can clearly see that the spectrum indices in radio, optical and X-ray bands are different. Note that in order to show the change in spectrum indices clearly, the y-axis is set to be f_ν instead of νf_ν as in the other figures.

Protons can also be accelerated in shearing plasma flows. Since a proton is more massive than an electron, its mean free path and cooling time are longer than those of electrons of the same Lorentz factor. Therefore the most restrictive constraints on maximum particle energy come from longest interacting wavelength and the size of acceleration region. Both these constraints are related to the Larmor radius of the particle, which only depends on particle energy when the value of magnetic field is fixed. So the maximum proton energy should be comparable to that of electrons for the given jet parameters, say, around PeV. Fig. (4.9)-(4.11) show the timescale, time-dependent spectrum and synchrotron emission of protons, the parameters of which are the same with those in Fig. (4.4)-Fig. (4.6). The cut-off in proton spectrum are around $\gamma = 10^6$ or PeV. This leads to a peak around 5 GHz in the synchrotron energy spectrum. Before the cut-off, the proton spectra are also consistent with the analytical solutions.

4.3.2 In Ultra-relativistic Jets

The acceleration process is more complicated in an ultra-relativistic gradual shearing jet. As we pointed out above, with a linear velocity profile, the bulk Lorentz factor of the jet decreases rapidly to a few at the outer part of the jet and hence only the inner most part can have a relativistic shear. This can be also seen from the lower panel of Fig. (4.3). The analytical acceleration rate significantly deviates from the numerical one in relativistic shear case at $r = 10^{-3} r_j$. On the other hand, since the bulk Lorentz factors of different layers can be much different, we can not simply get space-averaged Fokker-Planck coefficients to compute the accelerated spectrum. This is because that different layers are in different inertial frames and their times are not simultaneous¹. A unified time in different layers can be used if we consider the process in the observer's frame. However, the distribution of particles and the interacting MHD waves (or the

¹Strictly speaking, this problem also exists in a weakly-relativistic jet. But the difference of velocity is small among different layers, so it will not make much error when ignoring this effect.

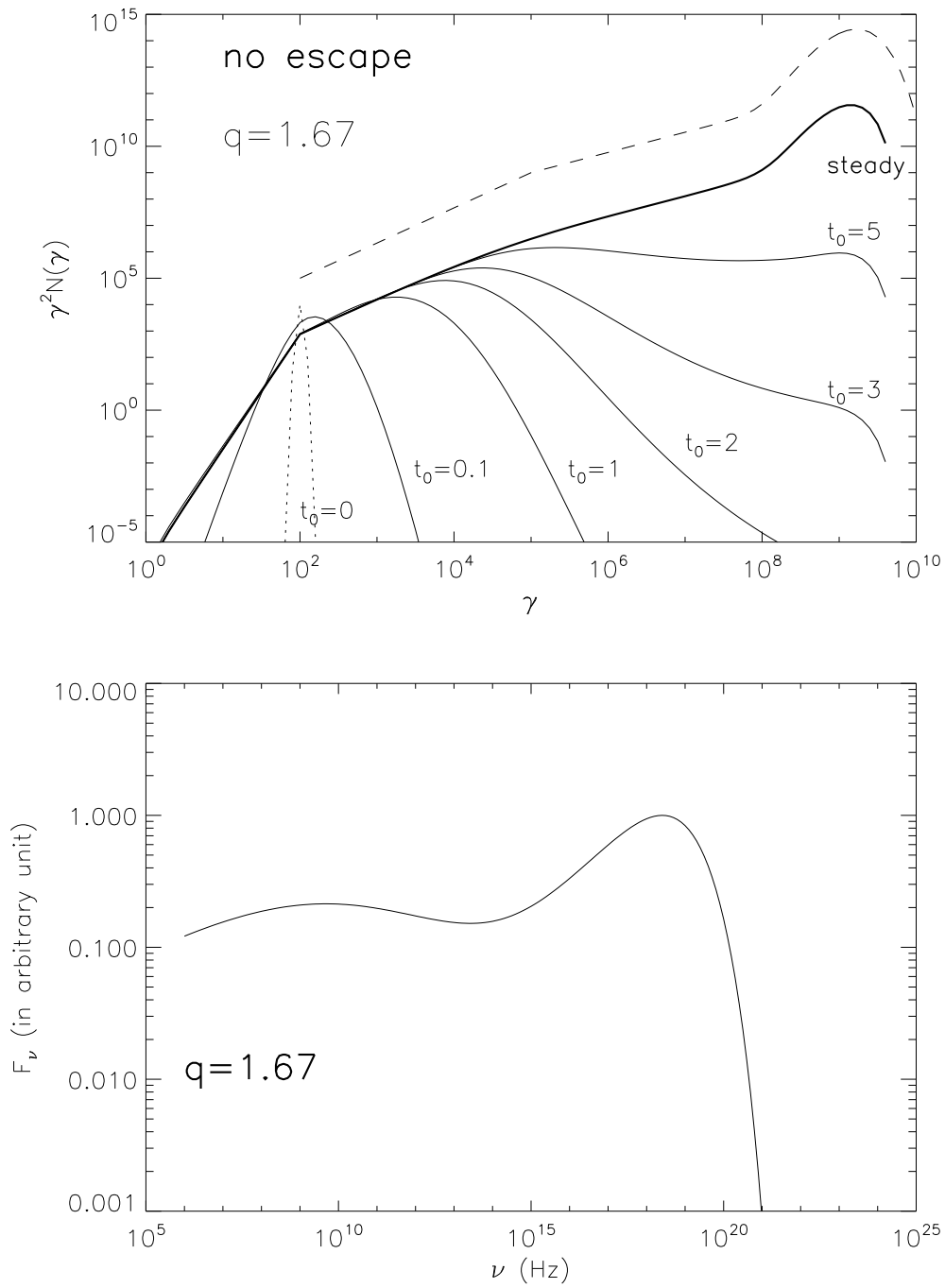


Figure 4.8: The time-dependent evolution of electron spectrum without escape (but with stochastic acceleration). All parameters are same the as in the Fig. 4.5.

scattering centers) will become highly anisotropic and inhomogeneous due to relativistic motion of these layers.

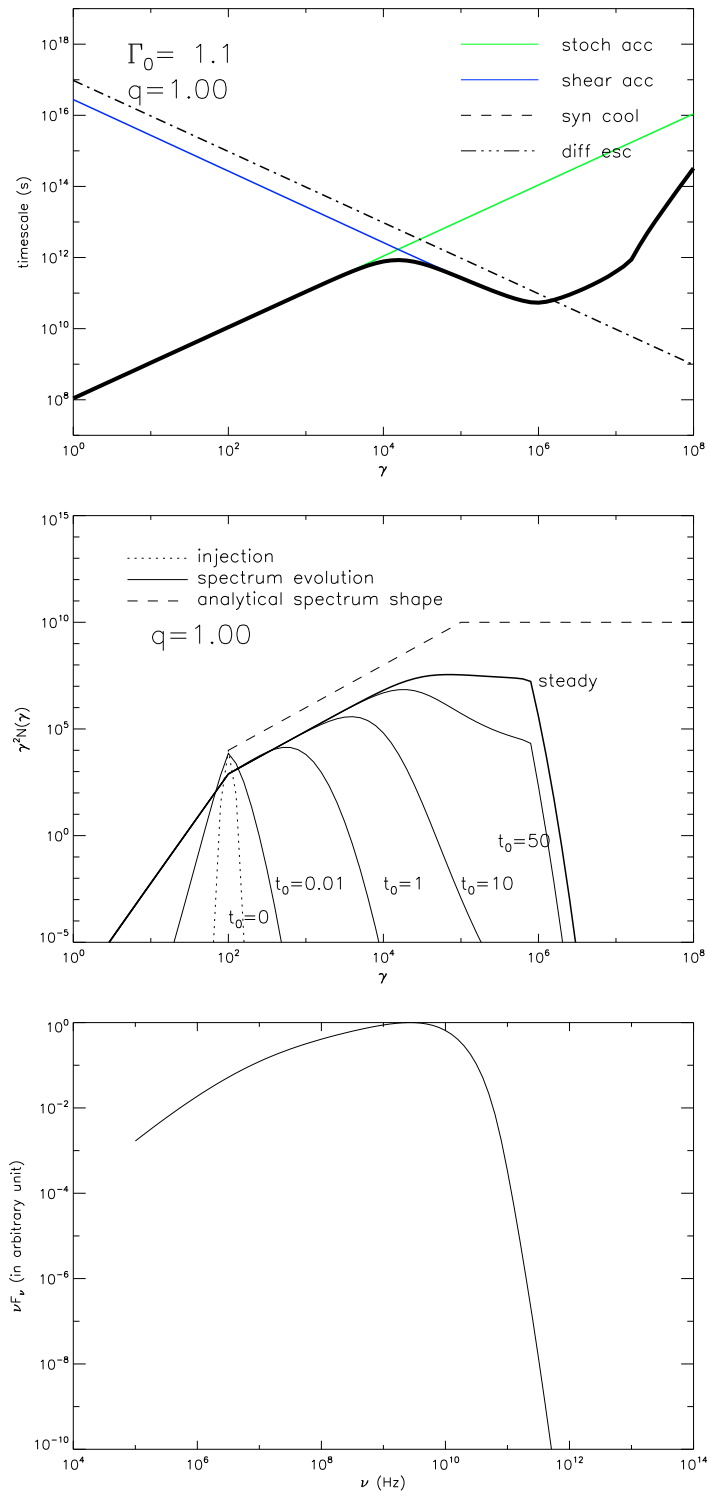


Figure 4.9: the same as Fig. 4.4 but for proton acceleration.

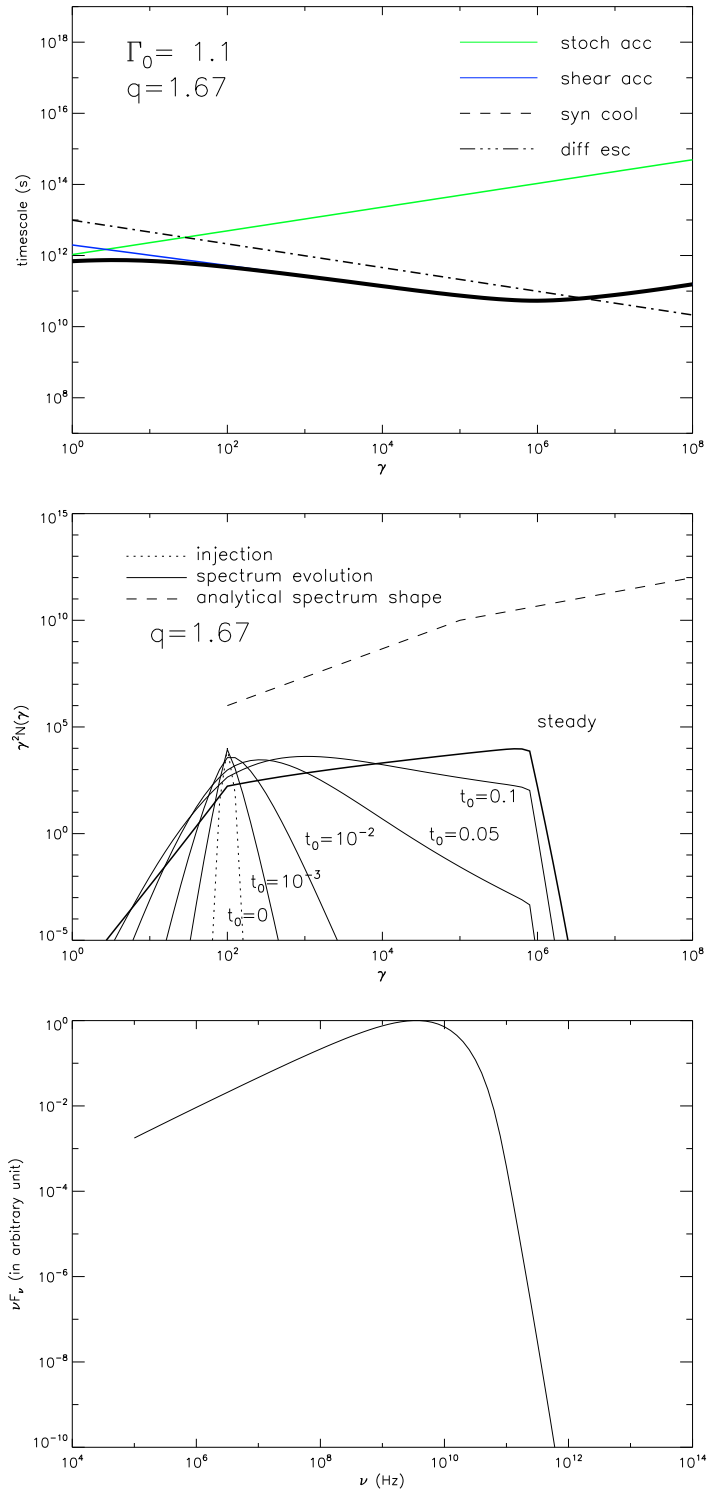


Figure 4.10: the same as Fig. 4.5 but for proton acceleration.

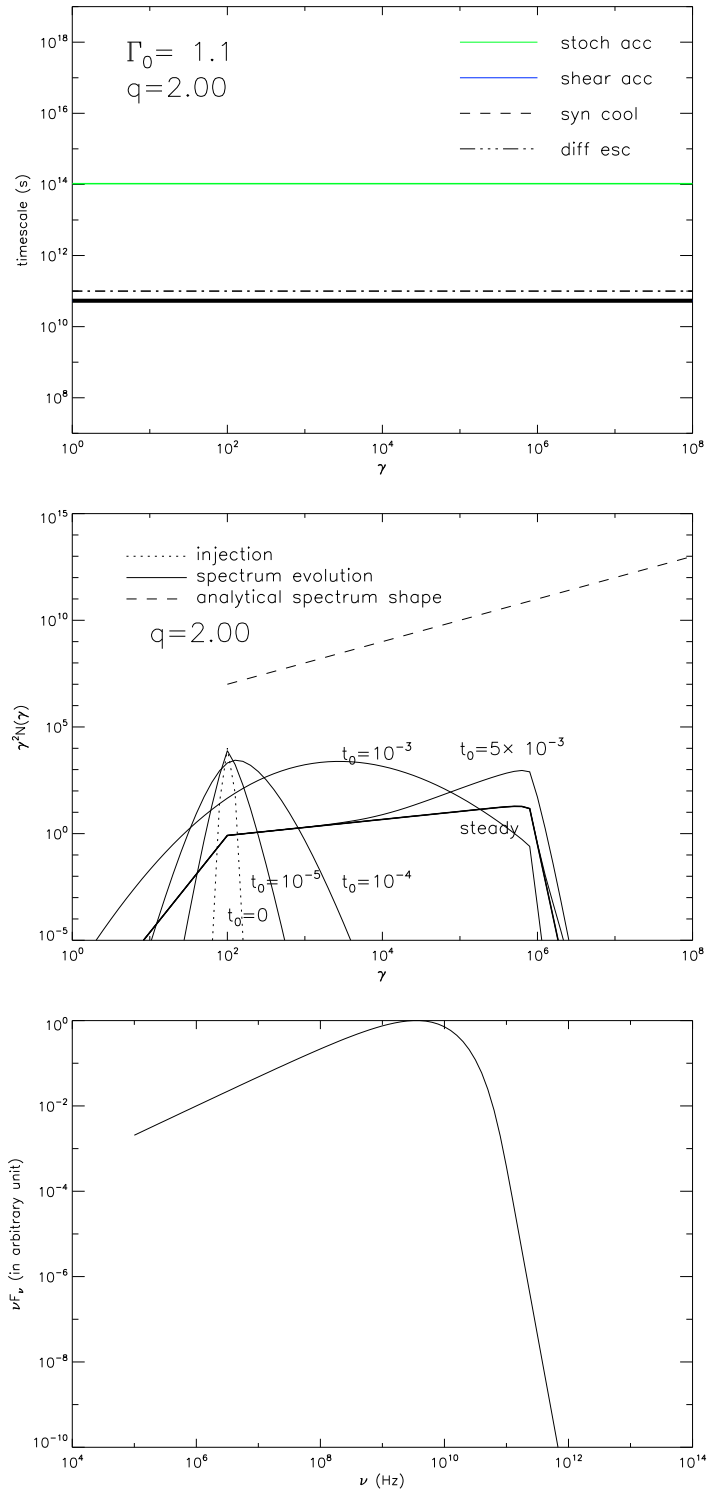


Figure 4.11: the same as Fig. 4.6 but for proton acceleration.

We leave the spatial-averaged or spatial-resolved particle spectrum to future study, and here we just naively focus on the acceleration process at a certain inner layer, as if particles were well confined to the layer. This is to see how the obtained form of the acceleration rate (i.e., Eq. 4.28) shapes the momentum distribution of particles. However, even under such a simplification, the accelerated particle spectrum still can not be obtained by solving Eq. (4.33) because the momentum change of particles in one scattering is too big to simply treat it as a diffusion process. But there should be still some dispersion in the momentum distribution of particles due to that particles moving towards different directions (i.e., different θ) will move to different layers and acquire different Lorentz boosts.

We use the Monte-Carlo method to study the evolution of the spectrum. We inject 10^4 mono-energetic electrons with Lorentz factor of 100 at the layer at $r = 10^{-3}r_j$, and assign a random direction of velocity for each of them. For successive scatterings, we artificially assume the environments are the same with that of the original position. Then we calculate their energies in the rest frame of the arrived new positions for every successive scattering. Results are shown in Fig. (4.12). One thing worth noting in the figures is that the low energy part of numerical spectrum in steady state are basically consistent with the analytical steady-state solutions (dashed lines) with neglecting the diffusion term and escape term in Eq. (4.33), say,

$$n(\gamma) = \left[\left\langle \frac{\Delta\gamma}{\Delta t} \right\rangle + \langle \dot{p}_c \rangle \right]^{-1} \times \text{Const.} \quad (4.37)$$

This implies that the dispersion in momentum space is not efficient if the shear is relativistic. Indeed, given a relativistic shear, a strong Lorentz boost would dominate the energy change. However, when the acceleration rate is close to the cooling rate, the systematic energy change term in Eq. (4.33) becomes very small or even vanishes because the energy gain the cooling terms cancel each other. Then the dispersion term, although we do not know how to depict it analytically, will be important in shaping the spectrum at the cut-off region.

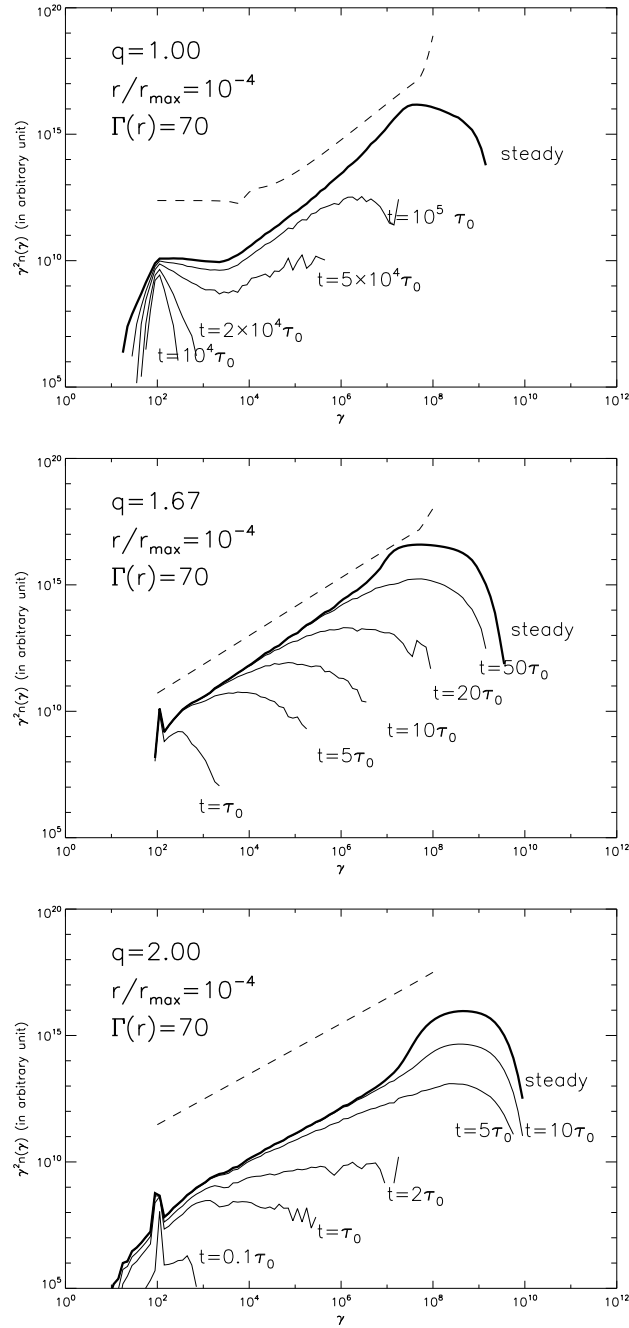


Figure 4.12: Time-depended evolution of electron spectrum, by using Monte-Carlo method, in an ultra-relativistic gradual-shear jet for $q = 1$, $q = 5/3$ and $q = 2$ cases respectively. Solid lines are the spectrum in different time while dash lines show the steady-state analytical solutions with neglecting the diffusion term in the Fokker-Planck equation.

4.4 Discussion

4.4.1 Possible Application on Extended X-ray Emissions from Large-scale AGN Jets

Large-scale (kpc to Mpc) jets are observed in the X-ray bands from various radio galaxies and quasars, such as 3C15 (Kataoka et al. 2003), 3C120 (Harris et al. 2004), 3C279 (Jester et al. 2006), M87 (Wilson & Yang 2002; Marshall et al. 2002), Pictor A (Wilson et al. 2001; Hardcastle et al. 2005), PKS 1127-145 (Siemiginowska et al. 2002), PKS 1136-135 (Sambruna et al. 2006). Besides bright X-ray knots and hotspots, extended X-ray emissions have also been found from many jets. The origin of the X-ray emissions is still under debate. One popular model ascribes X-ray emission to synchrotron radiation from electrons with Lorentz factor of 10^{7-8} . Sometimes an additional component of electrons is required to explain radio and optical emissions since a hardening occurs in X-rays therefore the broadband spectrum can not be fitted by a single component of electrons. In the synchrotron model, the lifetime of the X-ray emitting electrons is a few thousands years in a magnetic field of a few μG , so even if these electrons would travel rectilinearly, their energies will be exhausted before migrating beyond hundreds of parsecs. So the acceleration of these X-ray emitting electrons should be spatially distributed along the whole kpc-Mpc jets where extended emissions are presented, instead of solely related to certain specific regions such as the shock in the jet head. Formally, stochastic acceleration could be responsible for these energetic electrons since the acceleration is also distributed. However, the synchrotron photon energy can only marginally achieve the required value, $E_{\text{ph,max}} \approx 1 \text{ keV} (\beta_A/0.01)^2 (\xi/0.1) \Gamma_j$, even if momentum diffusion of electrons is in Bohm limit ($q = 1$), unless there exists relativistic MHD waves (also see Wang 2002). An alternative model is the IC/CMB model, in which electrons with $\gamma \sim 100$ in the rest frame of a highly relativistic jet with bulk Lorentz factor of $\sim 10 - 20$ are scattered off cosmic microwave background photons and produce X-rays (e.g., Celotti et al. 2001). This model does not call for a distributed acceleration since the lifetime of X-ray emitting electrons are much longer in this case. Neither does it need to invoke another electron component since a hardening in X-ray can be naturally produced when X-ray and low energy emissions stem from inverse Compton and synchrotron radiation respectively. However, the model requires well alignment of jets with the line of sight, leading to a very long physical length of the jets, sometimes even $> \text{Mpc}$. Furthermore, it requires the jets to maintain

highly-relativistic speeds at such a large scale. Besides, the model seems to suffer energetics problems. A comprehensive review of X-ray jets from AGN and the models can be found in Harris & Krawczynski(2006).

Here, we propose synchrotron emissions from electrons accelerated in shearing jets as a possible origin of the extended X-ray emissions from large-scale jets. Shear acceleration is a distributed acceleration. It will work as long as MHD turbulence and shearing flow both occur. As shown in Fig. 4.4-4.6, the shear acceleration is a more efficient acceleration mechanism which can accelerate electrons up to PeV energies in a weakly-relativistic jets with reasonable parameters. Comparing to stochastic acceleration, it enhances the maximum electron energy by about two orders of magnitude. In the synchrotron spectrum of the accelerated electrons, a softening around optical/UV band may occur at the energy corresponding to where shear acceleration overcomes the stochastic acceleration. Whether a hardening in X-ray can be produced depends on the types of turbulence and the escape process which are determined by the jet properties. We notice that a similar idea of X-ray emitting electrons being accelerated at jet boundary was proposed by Stawarz & Ostrowski (2002) and Rieger & Mannheim (2002).

4.4.2 Acceleration of Ultra-high Energy Cosmic Rays

As pointed out in Section 4.3.1, proton acceleration by the shear mechanism is mainly constrained by containment and wave-particle interaction. The maximum proton energy is just around PeV for the given jet parameters. Since protons are less effected by cooling process, a larger magnetic field will be conducive to get higher energy proton energy since it will reduce Larmor radii of protons. Taking $q = 5/3$ case as an example and assuming the longest wavelength of turbulent wave $\lambda_{\max} = 0.1\Delta L$, we find the conditions to produce ultrahigh energy proton ($E > 10^{18}\text{eV}$) in a shear jet to be

1) $\Delta L > \lambda = \xi^{-1} r_g^{2-q} \lambda_{\max}^{q-1}$ for both a weakly-relativistic jet and an ultra-relativistic jet, which gives

$$\Delta L > 3 \times 10^{16} \left(\frac{E}{10^{18}\text{eV}} \right) \left(\frac{B}{1\text{G}} \right)^{-1} \left(\frac{\xi}{0.1} \right) \text{cm} \quad (4.38)$$

2) $\lambda_{\max} > r_g$, which is equivalent to

$$\Delta L > 3 \times 10^{16} \left(\frac{E}{10^{18}\text{eV}} \right) \left(\frac{B}{1\text{G}} \right)^{-1} \text{cm} \quad (4.39)$$

for both a weakly-relativistic jet and an ultra-relativistic jet. Note that this constraint does not depend on the type of turbulence

3) $t_{\text{syn}} > t_{\text{acc}}$, which gives

$$\Delta L < 2.7 \times 10^{18} \left(\frac{E}{10^{18} \text{eV}} \right)^{-1/2} \left(\frac{B}{1 \text{G}} \right)^{-7/4} \left(\frac{\xi}{0.1} \right)^{-3/4} \left(\frac{\Gamma_j}{1.1} \right)^3 \left(\frac{\beta_{j,0}}{0.42} \right)^{3/2} \text{ cm} \quad (4.40)$$

for a weakly-relativistic jet and

$$\Delta L < 5.8 \times 10^{28} \left(\frac{E}{10^{18} \text{eV}} \right)^{-7/5} \left(\frac{B}{1 \text{G}} \right)^{-11/5} \left(\frac{\Gamma_j}{10^3} \right)^{13/5} \left(\frac{\xi}{0.1} \right)^{3/5} \text{ cm} \quad (4.41)$$

for an ultra-relativistic jet. Note that in the comoving frame of ultra-relativistic jet, we only require proton energy to be accelerated to $\sim E/\Gamma_j$.

As we fix the values of λ_{max} , Γ_j , $\beta_{j,0}$ and ξ , we get requirements for combinations of the size of the shearing region ΔL and the average magnetic field strength B in the comoving frame of the jet from the above three conditions. Fig. (4.13) shows the available parameter space for acceleration of 10^{18} eV and 10^{20} eV protons in a weakly-relativistic jet and an ultra-relativistic jet respectively. Let us assume the transverse size of a jet is 1%-10% of its length, and then we find that 10 kpc-100 kpc scale AGN jets with magnetic field $1\mu\text{G}$ - $100\mu\text{G}$, GRB jets in prompt emission phase with jet length 10^{13-16} cm and magnetic field 10^{3-5} G may be potential sources for 10^{18} eV protons (c.f., Rieger & Duffy 2005), while the constraint becomes much more stringent for acceleration of 10^{20} eV protons. Some very energetic GRB jets may marginally meet the requirement. But note that Fig. (4.13) is only valid for a Komogorov-type turbulence (i.e., $q = 5/3$) with a linear longitudinal shear for the jet velocity, and we also fix many other parameters. For $q = 1$, we do not need to consider the constraint from cooling, while for $q = 2$ the constraint of $\Delta L > \lambda$ disappears since the mean free path of particle in that case is irrelevant to particle energy. So we can not completely exclude the possibility of acceleration of 10^{20} eV particle in the shear acceleration mechanism (c.f., Ostrowski 1998).

4.5 Conclusion

In this work, we used a microscopic analysis and showed that particles can be accelerated efficiently in a relativistic turbulent shearing jets. We derived the acceleration rate and momentum diffusion rate analytically, and found that the shear acceleration timescale is inversely proportional to particle energies. More

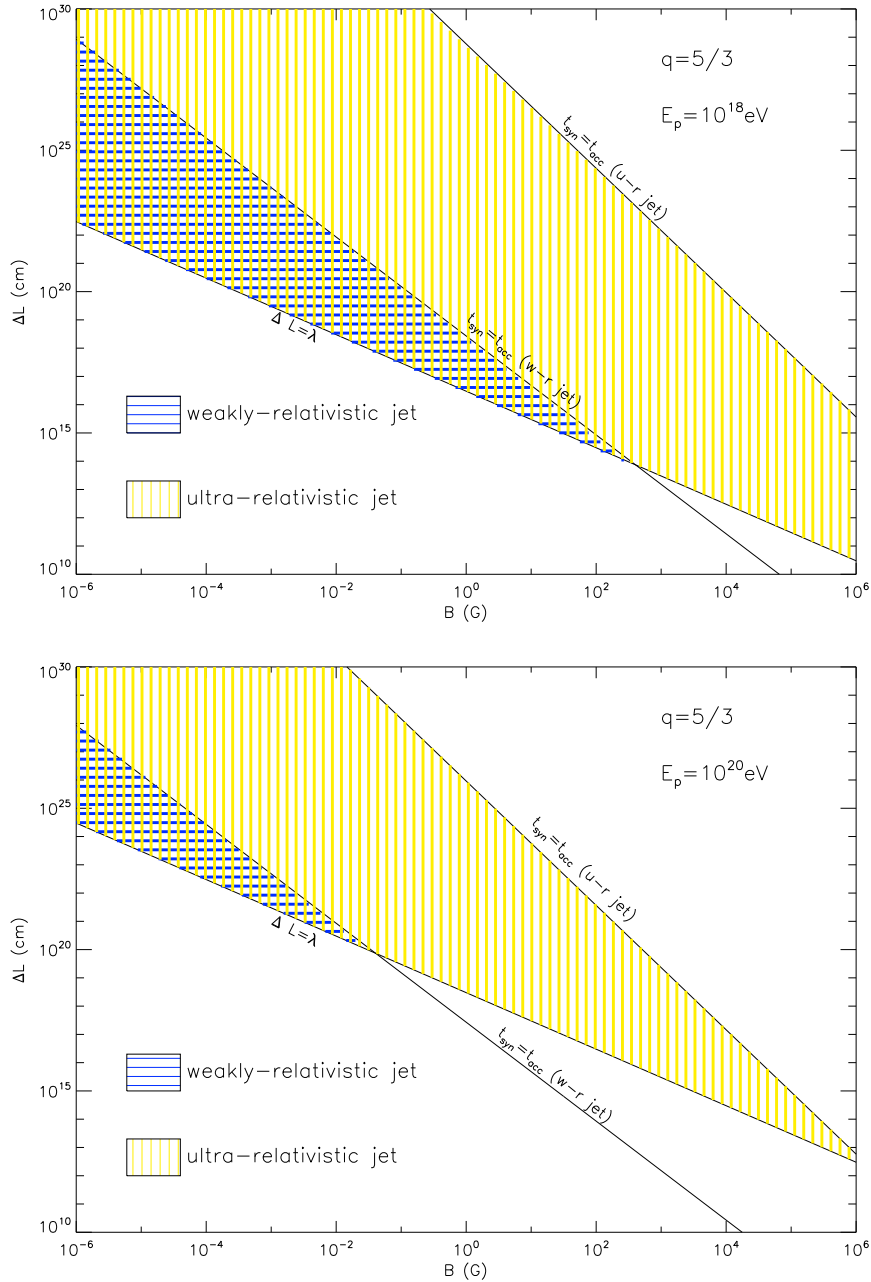


Figure 4.13: Available jet parameter space for acceleration of 10^{18} eV (upper panel) and 10^{20} eV (lower panel) protons for $q = 5/3$ case. The hatched blue regions are for weakly-relativistic jets and the hatched yellow regions are for ultra-relativistic jets. Jet parameters are identical to those used in Section 4.3.1 and Section 4.3.2.

energetic particles will gain energy faster so the mechanism is conducive to the acceleration of high energy particles. We also calculated how the distribu-

tion of particles evolves with time. In a steady state, if neglecting the diffusive escape process, the acceleration in a turbulent field with a power-law energy spectrum gives rise to a power-law differential particle distribution of $n(\gamma) \propto \gamma^{1-q}$ at low energy where stochastic acceleration dominates, and $n(\gamma) \propto \gamma^{q-3}$ beyond the energy that shear acceleration rate exceeds the stochastic acceleration rate. The acceleration process will be eventually stopped by various process such as cooling, direct escape and inefficient wave-particle interaction. In electron acceleration case, the main process to stop the acceleration is synchrotron cooling. A bump in spectrum caused by cooling pile-up will occur and then followed by an exponential-like cut-off in the form of $n(\gamma) \propto \gamma^{1+q} \exp\left[-\frac{5}{q-1} \left(\frac{\gamma}{\gamma_{\max}}\right)^{q-1}\right]$. Considering the diffusive escape will soften the spectrum and the pile-up bump would vanish if some particles at that energy can escape the jet efficiently. We also found that although stochastic acceleration is much less efficient than shear acceleration in acceleration of high-energy particles, it can serve as a pre-acceleration and boosts the whole acceleration process. Synchrotron emissions from the accelerated particles are also calculated. Radio, optical/UV and X-ray bands may have different photon indices according to the jet parameters. Finally, we discussed the possible application of the shear acceleration mechanism to explaining the X-ray emissions of large-scale AGN jets, as well as the possibility of producing ultrahigh energy cosmic rays.

Summary, Discussion and Future Work

To unravel the puzzle of UHECRs, we have to jointly use information from various sources. Direct measurements of the spectrum shape, the chemical composition, and arrival directions of UHECRs are linked to each other. Indirect measurements such as secondary neutrinos and gamma rays may provide extra constraints and implications on their sources. This dissertation aims to take a closer look at the mystery of UHECRs from different perspectives.

In Chapter. 2, we try to find the possible link between the recently discovered sub-PeV/PeV neutrinos and UHECR sources. To contribute the observed UHECRs, the energy budget of sources must be in the range of $10^{44.5} - 10^{45.5} \text{erg/Mpc}^3 \text{yr}$ while the uncertainty mainly arises from the disputed transition from Galactic to extragalactic cosmic rays. So if the detected neutrinos have the same origin as the UHECRs, then based on the neutrino flux, we can obtain some clues on the UHECR sources from the required pion-production efficiency, as the latter quantity is sensitively dependent on the environment of the sources, such as gas density and magnetic field strengths. Our calculation shows that semi-relativistic hypernova remnants in star-forming galaxies could provide a reasonable neutrino flux. There are two caveats though. First, the uncertainty in the energy above which the extragalactic cosmic rays component starts to dominate the Galactic one, i.e. the second-knee transition model and the ankle transition model, will lead to an uncertainty of one order of magnitude in the energy budget of the sources. To distinguish the two models, we need to measure the shape of the spectrum around the second knee accurately. It is often thought that the second-knee is due to the rapid drop of Galactic cosmic ray flux while the extragalactic component takes over. However, as a matter of fact, the second-knee is not robustly established. On the other hand, if a new component takes over we should expect a hardening in the spectrum, not only a softening.

Otherwise, a very coincidental flux ratio between the Galactic cosmic ray and the extragalactic one is required to reproduce this feature. A longer operation time for these experiment is required to achieve better statistics. The second caveat is that the diagnosis on UHECR sources is based on a real link between the neutrinos and UHECRs. The energies of the parent particles of the observed neutrinos—if they are protons—are only required to be $\sim 1 - 100$ PeV, rendering it entirely possible that these neutrinos stem from some 100 PeV-proton accelerators. After all, given harsher requirements for higher energy accelerators, we can expect there should be more 100 PeV-proton accelerators than UHE-proton accelerators in our Universe, and hence the possibility of the observed neutrinos coming from lower-energy accelerators is higher. Only if the neutrino spectrum extends to > 10 PeV without a break can we support this link, but this would require an accumulation of events for many more years since the flux at such high energies is very low.

In Chapter. 3, we utilize the PAO measurements of the chemical composition and arrival directions of UHECRs simultaneously to constrain the nearby UHECR sources. The method is based on a quite robust feature of rigidity-dependent propagation of charged particles in a magnetic field. Particles of the same rigidity (E/Z) will follow the same path if they have the same initial condition, so if the anisotropy above 55 EeV observed by the PAO is true and those highest-energy particles are indeed metal nuclei, the protons with the same rigidity from the same sources would cause an even stronger anisotropy pattern at lower energies, which, however, is not observed. This fact restricts the potential sources to be high-metallicity objects. Moreover, in the case that those > 55 EeV events are nuclei, these particles may be (partially) disintegrated into secondary protons during propagation so that merely these secondary protons would cause a stronger anisotropy signal at lower energies, even if there would be no primary protons from the sources. This provides an upper limit on the distances of the sources of observed UHECRs. In the case of carbon, nitrogen or oxygen nuclei, it requires the sources' distance to be smaller than a few tens of Mpc, even more demanding than constraints imposed solely by the particle attenuation length (e.g., the GZK effect), leaving us a very limited number of candidates. But we need to point out that this constraint is based on the correctness of the PAO's measurements on both the chemical composition and the arrival directions of events. In fact, our derived constraints are so strong that it might challenge the validity of the PAO's results, which may have suffered from some deficiencies

such as insufficient statistics or a lack of knowledge of the hadronic model at such high energies. Unfortunately, the present large uncertainty is not going to be improved in the near future.

In Chapter. 4, we discussed the mechanisms of acceleration of UHECRs. We study the shear acceleration mechanism, which is also a Fermi-type acceleration mechanism but much less explored than the shock acceleration and stochastic acceleration mechanisms. The shear acceleration mechanism will naturally work in the presence of turbulent MHD waves and shearing background flows, which may be common in various astrophysical environments. For instance, when an outflow interacts with its ambient medium, its outer part will be decelerated more than the central part. Jets also have rotation with respect to the propagating axis, which may be associated with the Keplerian rotation of the accretion disk, and cause a transverse shear. For simplicity, we considered a longitudinal shear in a symmetric large scale relativistic jet while the transverse shear may have already been smeared out at kpc-Mpc scales. It should be noted that we assume isotropic diffusion throughout this study. Acceleration rates and diffusion rates are derived, and the time-dependent particle spectrum as well as the synchrotron emission of accelerated particles are presented. A specific feature of shear acceleration is that it tends to accelerate higher energy particles more efficiently. We found that PeV electrons and EeV protons can be obtained under typical jet parameters, while 10^{20} eV protons may also be available, but requires extreme or, probably, unrealistic conditions. The main difficulty in accelerating a 10^{20} eV proton is that a particle of such a high energy has a very large Larmor radius while there may not be turbulent waves with wavelengths long enough to interact with these particles, while the wavelength of an MHD wave is supposed to be smaller than the size of the jet. This constraint is similar to the Hillas condition, but more rigorous. On the other hand, we should note that this wave-particle interaction problem is not unique to shear acceleration. Shock acceleration and stochastic acceleration also suffer from this issue, since both these mechanisms require turbulent waves in the background flow to work. Another interesting feature of the shear acceleration is that the latter is not sufficiently effective for low energy particles. This part of the spectrum is supported by the stochastic acceleration. Stochastic acceleration always exists, given the presence of turbulent waves. Although it is less relevant for the acceleration of high energy particles when compared with the shear acceleration, it serves as a pre-accelerator and boosts the whole acceleration process. The total spectrum

then manifests itself as a three-segment power law with a high-energy cutoff. The first segment is caused by stochastic acceleration. The second one, which is softer, is shaped by the shear acceleration. At the high energy end, synchrotron cooling is non-negligible anymore and creates a pile-up bump, which forms the third segment of the power law, followed by a cutoff. Synchrotron emission from such a distribution of particles will also lead to a three-segment photo spectrum, and may be consistent with the emission from large-scale AGN jets. Another feature of shear acceleration is that it can happen everywhere in a region of shearing outflow. This is not the case of the shock acceleration. As particles only get accelerated at the shock front, one may not expect these radiating particles to be responsible for emissions far away from the shock, since they should have already cooled before undergoing significant migration. So shear acceleration may be a solution to the extended emission throughout almost the entirety of the kpc-Mpc scale AGN jets. Lastly, we should mention the approximations used in this work. First, we assume that both the turbulent waves and the diffusion of particles are isotropic. This may not be true if the regular background magnetic field is much stronger than the turbulent magnetic field, because Alfvén waves can not propagate perpendicular to the background magnetic field (although magnetic sonic wave is still isotropic in the presence of strong regular magnetic field). Also, the perpendicular diffusion of particles would be inhibited by the longitudinal background magnetic field and would decrease the acceleration rate. In an ultra-relativistic shearing jet, the physical picture will be more intricate because time in different positions will not be simultaneous, due to different Lorentz factors. One possible solution is to calculate everything in the lab frame. To do this, we need to account for the anisotropic distribution of particles and MHD waves even if they are isotropic in the comoving frame. This would be a topic for future studies.

BIBLIOGRAPHY

- Abbasi, R. U, et al., Physical Review Letters, 92, 151101 (2004)
- Abbasi, R. U et al., Astrophys. J, 622, 910 (2005)
- Abbasi, R. U., Abu-Zayyad, T., Allen, M., et al. 2008, Physical Review Letters, 100, 101101
- Abbasi, R. U., Abu-Zayyad, T., Al-Seady, M., et al. 2010, Physical Review Letters, 104, 161101
- Aharonian, F. A., Belyanin, A. A., Derishev, E. V., Kocharovsky, V. V., & Kocharovsky, V. V. 2002, Phys. Rev. D, 66, 023005
- Ahlers, M. & Murase, K., arXiv:1309.4077
- Allard, D., Ave, M., Busca, N., et al. 2006, JCAP, 9, 005
- Aloisio, R., Boncioli, D., Grillo, A. F., Petrera, S., Salamida, F. 2012, JCAP, 10, 007
- Aloisio, R., Berezhinsky, V., Grigorieva, S. 2013, Astroparticle Physics, 41, 73
- Aloisio, R., Berezhinsky, V., Grigorieva, S. 2013, Astroparticle Physics, 41, 94
- Alvarez-Muñiz, J., and P. Mészáros, Phys. Rev. D, 70, 123001 (2004)
- Anchordoqui, L.A, Hooper, D., S. Sarkar and A.M. Taylor, Astropart. Phys., 29, 1, 2008
- Anchordoqui, L. A., Goldberg, H., Lynch, M. H., et al. 2014, Physical Review Letters, 89, 083003
- Arons, J. 2003, Astrophys. J, 589, 871
- Bell, A. R. 1978a, MNRAS, 182, 147
- Bell, A. R. 1978b, MNRAS, 182, 443

- Berezhko, E. G. 1981, International Cosmic Ray Conference, 3, 506
- Berezhko, E. G., & Krymskii, G. F. 1981, Soviet Astronomy Letters, 7, 352
- Berezhko, E. G. 1982, Soviet Astronomy Letters, 8, 403
- Berezinsky, V., Gazizov, A., & Grigorieva, S. 2006, Physical Review Letters, 74, 043005
- Berezinsky, V., A. Gazizov, M. Kachelrieß and S. Ostapchenko, Physics Letters B, 695, 13 (2011)
- Bernet, M.L, Miniati, F. and S.J. Lilly, Astrophys. J, 772, L28 (2013)
- Bertone, G., Isola, C., Lemoine, M., Sigl, G. 2002, Physical Review Letters, 66, 103003
- Bhattacharjee, P. 2000, Phys. Rep., 327, 109
- Bieging, J. H. 1990, The Evolution of the Interstellar Medium, 12, 137
- Biermann, P.L. and P. A. Strittmatter, Astrophys. J, 322, 643 (1987)
- Biermann, P. L., & Strittmatter, P. A. 1988, The Impact of VLBI on Astrophysics and Geophysics, 129, 85
- Biermann, P. L, Astron. and Astrophys. 271, 649 (1993);
- Biermann, P. L and J.P. Cassinelli, Astron. and Astrophys. 277, 691 (1993)
- Blasi, P. and E. Amato, JCAP, 1, 11 (2012)
- Breitschwerdt, D., McKenzie, J. F and Voelk, H. J, Astron. and Astrophys., 269, 54 (1993)
- Budnik, R., Katz, B., MacFadyen, A., Waxman E. 2008, Astrophys. J 673, 928
- Casolino, M., Adams, J. H., Bertaina, M. E., et al. 2011, Astrophysics and Space Sciences Transactions, 7, 477

- Celotti, A., Ghisellini, G., & Chiaberge, M. 2001, MNRAS, 321, L1
- Chakraborti, S., Ray, A., Soderberg, A. M., Loeb, A., & Chandra, P. 2011, Nature Communications, 2,
- Chang, X.-C., & Wang, X.-Y. 2014, ApJ, 793, 131
- Chang, X.-C., Liu, R.-Y., & Wang, X.-Y. 2014, arXiv:1412.8361
- Chevalier, R.A and A.W. Clegg, Nature, 317, 44 (1985)
- Cholis, I. and Hooper, D. 2013, JCAP, 6, 30
- Chung, D. J. H., Kolb, E. W., & Riotto, A. 1999, Phys. Rev. D, 60, 063504
- Clay, R. W., Whelan, B. J., & Edwards, P. G. 2010, Pub. Astron. Soc. Aus., 27, 439
- Coppi P.S, and F.A. Aharonian, Astrophys. J, 487, L9 (1997)
- Coroniti, F. V. 1990, Astrophys. J, 349, 538
- Crocker, R.M, Mon. Not. R. Astron. Soc., 423, 3512 (2012)
- Daddi, E, et al., Astrophys. J., 713, 686 (2010)
- de Gouveia dal Pino, E. M., & Lazarian, A. 2000, Revista Mexicana de Astronomia y Astrofisica Conference Series, 9, 97
- de Cea del Pozo, E., Torres D.F. and A.Y. Rodriguez Marrero, Astrophys. J, 698, 1054 (2009)
- Derishev, E. V., Aharonian, F. A., Kocharovskiy, V. V., & Kocharovskiy, V. V. 2003, Phys. Rev. D, 68, 043003
- Dermer, C. D., & Atoyan, A. 2006, New Journal of Physics, 8, 122

- Dermer, C. D., Razzaque, S., Finke, J. D., & Atoyan, A. 2009, *New Journal of Physics*, 11, 065016
- Domingo-Santamaría, E. and Torres, D.F., *Astron. and Astrophys.* 444, 403 (2005)
- Earl, J. A., Jokipii, J. R., & Morfill, G. 1988, *Astrophys. J.*, 331, L91
- Fang, K., Kotera, K., & Olinto, A. V. 2012, *Astrophys. J.*, 750, 118
- Farrar, G. R., & Gruzinov, A. 2009, *Astrophys. J.*, 693, 329
- Farrar, G. R., Jansson, R., Feain, I. J., & Gaensler, B. M. 2012, arXiv:1211.7086
- Fermi-LAT Collaboration, Abdo, A. A, et al. 2010a, *Physical Review Letters*, 104, 101101
- Fermi-LAT Collaboration, Ackermann, M, et al., 2010b, *The Astrophysics Journal*, 717, L71
- Fox, D. B, Kashiyama, K. & Mészáros, P, 2013 *Astrophys. J.*, 774, 74
- Galama, T. J., Vreeswijk, P. M., van Paradijs, J., et al. 1998, *Nature*, 395, 670
- Ghisellini, G., et al., *Mon. Not. R. Astron. Soc.*, 402, 497 (2010)
- Greisen, K., *Physical Review Letters* 16, 748 (1966)
- Guetta, D. and Della Valle, M., *Astrophys. J.*, 657, L73 (2007)
- Hamann, F., & Ferland, G. 1999, *ARA&A*, 37, 487
- Hardcastle, M. J., & Croston, J. H. 2005, *Mon. Not. R. Astron. Soc.*, 363, 649
- Harris, D. E., Mossman, A. E., & Walker, R. C. 2004, *Astrophys. J.*, 615, 161
- Harris, D. E., & Krawczynski, H. 2006, *ARA&A*, 44, 463

- He, H.-N., Wang, T, Fan, Y. Z., Liu, S. M. & Wei, D. M. 2013, *Physical Review D*, 87, 063011
- Hill, C. T., Schramm, D. N., & Walker, T. P. 1987, *Phys. Rev. D*, 36, 1007
- Hillas, A. M., Hollows, J. D., Hunter, H. W., & Marsden, D. J. 1971, *International Cosmic Ray Conference*, 3, 1007
- Hillas, A. M, *ARA&A.*, 22, 425 (1984)
- Hillas, A. M, *J. Phys. G*, 31, R95 (2005)
- Hooper, D., Sarkar, S., & Taylor, A. M. 2007, *Astroparticle Physics*, 27, 199
- Hooper, D., Sarkar, S., & Taylor, A. M. 2008, *Physical Review D*, 77, 103007
- Hooper, D., & Taylor, A. M. 2010, *Astroparticle Physics*, 33, 151
- Hopkins, A. M and J.F. Beacom, *Astrophys. J*, 651, 142 (2006)
- IceCube Collaboration, Abbasi, R. U et al., *Nature*, 484, 351 (2012)
- IceCube Collaboration, Aartsen, M. G et al., *Physical Review Letters*, 2013a, 111, 021103
- IceCube Collaboration, Aartsen, M. G et al., *Science*, 2013b, *Science*, 342
- IceCube Collaboration, Aartsen, M. G et al. 2013c *Physical Review D*, 88, 112008
- IceCube Collaboration, Aartsen, M. G et al. 2014, *Physical Review Letters*, 113, 101101
- Inoue, S, F. A. Aharonian, N. Sugiyama, *Astrophys. J*, 628, L9, 2005
- Inoue, Y., *Astrophys. J*, 728, 11 (2011)
- Iwamoto, K., Mazzali, P. A., Nomoto, K., et al. 1998, *Nature*, 395, 672

- Jester, S., Harris, D. E., Marshall, H. L., & Meisenheimer, K. 2006, *Astrophys. J.*, 648, 900
- Jokipii, J. R., Kota, J., & Morfill, G. 1989, *Astrophys. J.*, 345, L67
- Jokipii, J. R., & Morfill, G. E. 1990, *Astrophys. J.*, 356, 255
- Kalashev, O.E., Kusenko, A. and Essey, W. 2013, *Physical Review Letters*, 111, 041103
- Kampert, K.-H., & for the Pierre Auger Collaboration 2012, arXiv:1207.4823
- Kang, H, D. Ryu, T. W. Jones, 456, 422 (1996)
- Kang, H, J. P. Rachen, P. L. Biermann, 286, 257 (1997)
- Kataoka, J., Leahy, J. P., Edwards, P. G., et al. 2003, *Astronomy & Astrophysics* , 410, 833
- Katz, B. and E. Waxman, 2009 *JCAP*, 1, 18
- Keeney, B. A et al., *Astrophys. J.*, 646, 951 (2006)
- Kelner, S. R., Aharonian, F. A. & Bugayov, V. V. 2006, *Physical Review D*, 74, 034018
- Khan, E., Goriely, S., Allard, D., Parizot, E., Suomijärvi, T., Koning, A., Hilaire, S.,
Duijvestijn, M. C. 2005, *Astropart. Phys.* 23, 191
- Kotera, K., Lemoine, M. 2008, *Physical Review D*. 77, 123003
- Kotera, K., & Olinto, A. V. 2011, *ARA&A*, 49, 119
- Kulkarni, S.R., et al., *Nature*, 395, 663 (1998); A.M. Soderberg et al., *Nature*, 442, 1014
(2006)
- Kulsrud, R. M. 2005, *Plasma physics for astrophysics*, by R.M. Kulsrud Princeton series in
astrophysics. Princeton, NJ: Princeton University Press, 2005,
- Lacki, B. C and Thompson, T. A, *Astrophys. J.*, 762, 29 (2013)

- Lagage, P.O. and C.J. Cesarsky, *Astron. and Astrophys.*, 125, 249 (1983)
- Lamastra, A., Menci, N., Fiore, F. and Santini, P., *Astron. and Astrophys.* 552, A44 (2013)
- Law, D. R. et al., *Astrophys. J.*, 745, 85 (2012)
- Lemoine, M., & Waxman, E. 2009, *JCAP*, 11, 9
- Letessier-Selvon, A., & Stanev, T. 2011, *Reviews of Modern Physics*, 83, 907
- Liu, R.-Y., & Wang, X.-Y. 2012, *Astrophys. J*, 746, 40
- Liu, R.-Y., Wang, X.-Y., Wang, W., & Taylor, A. M. 2012, *Astrophys. J*, 755, 139
- Liu, R.-Y. & Wang, X.-Y. 2013, *Astrophys. J* 766, 73;
- Liu, R.-Y., Taylor, A. M., Lemoine, M., Wang, X.-Y., & Waxman, E. 2013, *ApJ*, 776, 88
- Liu, R.-Y., Wang, X.-Y., Inoue, S., Crocker, R., & Aharonian, F. 2014, *Phys. Rev. D*, 89, 083004
- Lodders, K., & Palme, H. 2009, *Meteoritics and Planetary Science Supplement*, 72, 5154
- Loeb, A. and E. Waxman, *J. Cosmol. Astropart. Phys.*, 5, 3 (2006)
- Lyubarsky, Y., & Kirk, J. G. 2001, *Astrophys. J*, 547, 437
- Lyubarsky, Y. E. 2003, *Mon. Not. R. Astron. Soc.*, 345, 153
- Magnelli, B et al., *Astron. and Astrophys*, 528, A35 (2011)
- Matthews, J., 2005, *Astropart. Phys.* 22, 387.
- Mannheim, K and P. L. Biermann, *Astron. Astrophys.*, 253, L21 (1992)
- Mannheim, K, *Astron. Astrophys.*, 269, 67, 1993

- Mannheim, K, R.J. Protheroe and J.P. Rachen, *Phys. Rev. D.* 63, 023003 (2001)
- Marshall, H. L., Miller, B. P., Davis, D. S., et al. 2002, *Astrophys. J.*, 564, 683
- McKeith, C. D, A. Greve, D. Downes and F. Prada, *Astron. and Astrophys.*, 293, 703 (1995)
- Mészáros, P. 2013, *Astrophys. J.*, 774, 74
- Milgrom, M., & Usov, V. 1995, *ApJ*, 449, L37
- Murase, K., & Nagataki, S. 2006, *Physical Review D*, 73, 063002
- Murase, K, Ioka, K., S. Nagataki and T. Nakamura, *Phys. Rev. D*, 78, 023005 (2008)
- Murase, K, Inoue, S and S. Nagataki, *Astrophys. J.*, 689, L105 (2008)
- Murase, K., J.F. Beacom, J. F and Takami, H. 2012, *J. Cosmol. Astropart. Phys.*, 8, 30
- Murase, K., Ahlers, M., & Lacki, B. C. 2013, *Physical Review D*, 88, 121301
- Murase K. & Ioka, K. 2013, *Phys. Rev. Lett.*, 111, 121102
- Nakamura, T., Mazzali, P. A., Nomoto, K., & Iwamoto, K. 2001, *ApJ*, 550, 991
- Neronov, A., Semikoz, D.V. & Tchernin, C., arXiv:1307.2158
- Norman, C. A, D. B. Melrose, A. Achterberg, 454, 60 (1995);
- Ostrowski, M. 1990, *Astron. and Astrophys.*, 238, 435
- Ostrowski, M. 1998, *Astron. and Astrophys.*, 335, 134
- Ostrowski, M. 2000, *Mon. Not. R. Astron. Soc.*, 312, 579
- Paczyński, B., *Gamma-Ray Bursts*, 4th Hunstville Symposium, 428, 783 (1998)

Piran, T. 2010, arXiv:1005.3311

Prieto, J. L, Stanek, K. Z and Beacom, J .F., *Astrophys. J.*, 673, 999 (2008)

Prokhorov, D. A. and E.M. Churazov, arXiv:1309.0197

Ptuskin, V. S, Voelk, H. J, Zirakashvili, V. N and Breitschwerdt, D, *Astron. and Astrophys.*,
321, 434 (1997)

Ptuskin, V. S, V.N. Zirakashvili and E.S. Seo, *Astrophys. J.*, 718, 31 (2010)

Puget, J. L., Stecker, F. W., & Bredekamp, J. H. 1976, *Astrophys. J*, 205, 638

Rachen, J. P., Biermann, P. L. 1993, *AA*, 272, 161

Rachen, J.P., Protheroe, R.J., & Mannheim, K., arXiv:astro-ph/9908031

Razzaque, S., arXiv:1309.2756

Rees, M. J., & Meszaros, P. 1994, *Astrophys. J*, 430, L93

Rieger, F. M., & Mannheim, K. 2002, *Astronomy & Astrophysics* , 396, 833

Rieger, F. M., & Duffy, P. 2004, *Astrophys. J*, 617, 155

Rieger, F. M., & Duffy, P. 2005, *ApJ*, 632, L21

Rieger, F. M., & Duffy, P. 2006, *Astrophys. J*, 652, 1044

Rodighiero, G., Daddi, E., I. Baronchelli, et al., *Astrophys. J.*, 739, L40 (2011);

Roulet, E., Sigl, G., van Vliet, A., & Mollerach, S., 2013 *JCAP*, 1, 28;

Sambruna, R. M., Gliozzi, M., Donato, D., et al. 2006, *Astrophys. J. J*, 641, 717

Schure, K. M and A.R. Bell, arXiv:1307.6575

Shopbell, P.L. and Bland-Hawthorn, J, *Astrophys. J.*, 493, 129 (1998)

Siemiginowska, A., Bechtold, J., Aldcroft, T. L., et al. 2002, *Astrophys. J. J*, 570, 543

Stawarz, L., & Ostrowski, M. 2002, *Astrophys. J. J*, 578, 763

Stanek, K.Z., et al., *Acta Astron.*, 56, 333 (2006);

Stecker, F. W. 1969, *Physical Review*, 180, 1264

High-energy neutrino emission from AGN core regions close to the black hole has also been discussed, e.g. F.W. Stecker, C. Done, M.H. Salamon and P. Sommers, *Phys. Rev. Lett.*, 66, 2697 (1991), although it is very unclear how protons may be accelerated to the requisite energies in such locations.

Strickland, D.K and T.M. Heckman, *Astrophys. J.*, 697, 2030 (2009)

Strong, A.W, et al., *Astrophys. J.*, 722, L58 (2010)

Sushchov, O., Kobzar, O., Hnatyk, B., & Marchenko, V. 2012, arXiv:1212.1402

Tacconi, L. J et al., *Astrophys. J.*, 640, 228 (2006)

Takahara, F. 1990, *Prog. Theor. Phys.*, 83, 1071

Taylor, A. M., Ahlers, M., & Aharonian, F. A. 2011, *Physical Review D*, 84, 105007

Telescope Array Collaboration, Abu-Zayyad, T., Aida, R., Allen, M., et al. 2013, *Astrophys. J*, 768, L1

Telescope Array Collaboration 2014, arXiv:1410.3151

Telescope Array Collaboration, Abbasi, R. U., Abe, M., Abu-Zayyad, T., et al. 2015, *Astroparticle Physics*, 64, 49

- The Pierre AUGER Collaboration, et al. 2008, *Astroparticle Physics*, 29, 188
- The Pierre AUGER Collaboration, et al. 2010, *Astroparticle Physics*, 34, 314
- Pierre Auger Collaboration, Abraham, J., Abreu, P., Aglietta, M., et al. 2010a, *Physical Review Letters*, 104, 091101
- Pierre Auger Collaboration, Abraham, J., Abreu, P., Aglietta, M., et al. 2010b, *Astroparticle Physics* 34, 314
- Pierre Auger Collaboration, Abraham, J., Abreu, P., Aglietta, M., et al. 2010c, *Physics Letters B*, 685, 239
- The Pierre Auger Collaboration, Abreu, P., Aglietta, M., et al. 2011, *JCAP*, 6, 22
- The Pierre Auger Collaboration, Aab, A., Abreu, P., et al. 2013a, arXiv:1307.5059
- The Pierre Auger Collaboration, Abreu, P., Aglietta, M., et al. 2013b, *Astrophys. J.*, 762, LL13
- Thompson, T. A, E. Quataert, E. Waxman, N. Murray and C.L. Martin, *Astrophys. J.*, 645, 186 (2006)
- Thompson, C. 2006, *Astrophys. J.*, 651, 333
- Trotta, R, et al., *Astrophys. J.*, 729, 106 (2011)
- Tsunesada, Y. for the Telescope Array Collaboration 2011, arXiv:1111.2507
- Ulrich, R. et al., 2009, *New J. Phys.* 11, 065018
- Vannoni, G., Gabici, S., & Aharonian, F. A. 2009, *Astronomy & Astrophysics*, 497, 17
- Vannoni, G, F.A. Aharonian, S. Gabici, S.R. Kelner, and A. Prosekin, A., *Astron. and Astrophys.*, 536, A56 (2011)

- van Weeren, R. J., Röttgering, H. J. A., Brüggén, M., & Hoeft, M. 2010, *Science*, 330, 347
- Vietri, M. 1995, *Astrophys. J.*, 453, 883
- Volk, H. J and P.L. Biermann, *Astrophys. J.* 333, L65 (1988)
- D. Wanderman, D. and Piran, T. 2010, *Mon. Not. R. Astron. Soc.*, 406, 1944
- Wang, X.-Y, Razzaque, S., Mészáros, P. and Dai, Z.-G. 2007, *Phys. Rev. D*, 76, 083009
- Wang, J.-C. 2002, *Chinese Journal of Astronomy & Astrophysics*, 2, 1
- Waxman, E 1995, *Phys. Rev. Lett.*, 75, 386
- Waxman, E., Miralda-Escudé 1996, *J., Ap*, 472, L89
- Waxman, E and J. Bahcall, *Phys. Rev. Lett.*, 78, 2292 (1997)
- Waxman, E and Bahcall, J 1998 *Phys. Rev. D*, 59, 023002
- Waxman, E. 2005, *Physica Scripta Volume T*, 121, 147
- Webb, G. M. 1989, *Astrophys. J.*, 340, 1112
- Webb, M. G. 1990, *International Cosmic Ray Conference*, 4, 126
- Wilson, A. S., Young, A. J., & Shopbell, P. L. 2001, *Astrophys. J.*, 547, 740
- Wilson, A. S., & Yang, Y. 2002, *Astrophys. J.*, 568, 133
- Winter, W. 2013, *Physical Review D*, 88, 083007
- Yüksel, H and M.D. Kistler, *Phys. Rev. D*, 75, 083004 (2007)
- Zandanel, F. and Ando, S., [arXiv:1312.1493](https://arxiv.org/abs/1312.1493);

Zatsepin, G. T., & Kuz'min, V. A. 1966, Soviet Journal of Experimental and Theoretical
Physics Letters, 4, 78